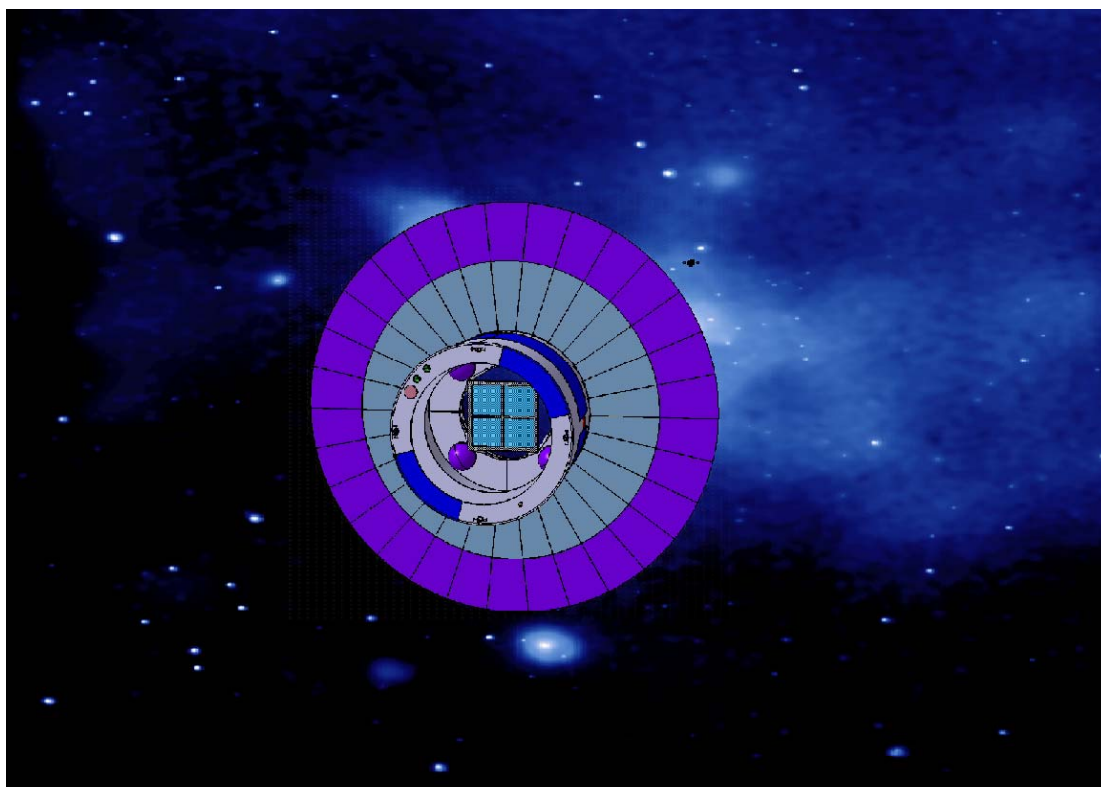




Technology Reference Study
Final Report
GRL
The Gamma Ray Lens



SCI-A/2005.058/GRL/CB
Craig Brown
July 2005

TECHNOLOGY REFERENCE STUDIES

The Science Payload and Advanced Concepts Office (SCI-A) at the European Space Agency (ESA) conducts Technology Reference Studies (TRSs), hypothetical science driven missions that are *not* currently part of the ESA science programme. Most science missions are in many ways very challenging from a technology point of view. It is critical that these technologies are identified as early as possible in order to ensure their development in a timely manner, as well as allowing the feasibility of a mission to be determined. Technology reference studies are used as a means to identify such technology developments.

The Technology Reference Study begins by establishing a series of preliminary scientific requirements. From these requirements, a hypothetical mission is designed that is capable of achieving the scientific goals. Critical issues and mission drivers are identified from the new mission concept and, from these drivers, a series of technology development activities are recommended. One such TRS has been conducted on a Gamma Ray Lens (GRL) mission. The GRL is an ideal candidate for a TRS due to the challenging nature of the technologies involved with focusing gamma rays. Identifying the key areas requiring technology development in this field prepares for any future high-energy astrophysics mission that the science community may propose, as well as establishes common technology development requirements possibly shared by different science missions.

A B S T R A C T

This is the final report for the Gamma Ray Lens (GRL) technology reference study performed by SCI-AM. The Gamma Ray Lens concept arises in response to the desire for high-energy observations of increased sensitivity in the soft gamma-ray regime.

Part one of this report is concerned with the theoretical aspects of the gamma ray lens. In particular, this section establishes a reference science case and science requirements for the GRL, as well as outlines the theory of multilayer mirrors and Laue crystals – the two technologies considered for gamma ray focusing in this report. Focal plane instrumentation is also investigated, with possible GRL detectors introduced and discussed. Finally, a sensitivity analysis model is introduced, used in part two as a tool to investigate potential GRL Laue lens configurations.

Part two contains the detail relating to the GRL mission design. This section outlines two Gamma Ray Lens profiles that were investigated for the TRS; a smaller Soyuz Fregat spacecraft and a larger Ariane 5 scenario. Effective area profiles and sensitivity analyses were conducted for both configurations, technology drivers were derived, and conclusions were made based on the science requirements outlined in part one.

It was found that the smaller Soyuz Fregat configuration, although achieving two orders of magnitude improvement on the sensitivity of SPI-INTEGRAL, was not capable of achieving all of the science requirements set out in part one. The Soyuz configuration failed to observe all energy bands of interest due to the mass constraints of the launcher. The complexity of two separate launches for the GRL optic and detector spacecraft, also make the smaller configuration undesirable.

The Ariane 5 configuration achieved all of the science requirements introduced in part one. A third Extended Ariane 5 lens configuration also demonstrated further potential by greatly increasing the energy band of the instrument. For this reason, the Ariane 5 configuration was chosen as the GRL mission baseline. From the conclusions of the mission design, a series of future actions and potential technology development activities (TDA) were identified.

TABLE OF CONTENTS

1. Introduction	9
------------------------	----------

Part I – Theoretical Aspects of the Gamma Ray Lens Mission

2. A Reference Science Case for the Gamma Ray Lens	11
2.1 Sources of interest in the Soft Gamma Ray regime	11
2.2 Preliminary Science Requirements Applicable to the GRL	16
2.3 The INTEGRAL Mission	18
2.4 References	25
3. High Energy Focusing Technologies	27
3.1 Graded Multilayer Mirrors	27
3.1.1 Hard X-ray and Soft Gamma Ray Astronomy	27
3.1.2 Principles of Multilayer Mirrors	28
3.1.3 Optic Design	32
3.1.4 Conclusions	36
3.1.5 References	37
3.2 Laue Crystals	38
3.2.1 Laue Diffraction	38
3.2.2 Direction of Diffraction	38
3.2.3 Throughput of the Diffracted Ray	39

3.2.4	Mosaicity	40
3.2.5	Temperature Effects	42
3.2.6	Gradient Crystals	43
3.3	The Basic Laue Lens Principle	44
3.3.1	The Focal Spot	45
3.3.2	Effective Area of the Gamma Ray Lens	46
3.3.3	Lens Size and Deployable Optics	48
3.3.4	References	49
4.	Focal Plane Instrumentation and Technologies	50
4.1	Gamma Ray Interaction with Matter	50
4.1.1	Photoelectric Absorption	50
4.1.2	Compton Scattering	51
4.1.3	Pair Production	52
4.2	High Energy Photon Detectors	53
4.2.1	Germanium Detectors	53
4.2.2	Scintillator Detectors	54
4.2.3	Compton Detectors	57
4.2.4	Polarisation Detectors	59
4.3	The Miniature 50-80 K Pulse Tube Cooler	60
4.4	References	61

5.	Sensitivity Analysis	62
5.1	Input to the Model	62
5.2	Model Description	63
5.3	Model Output	65
5.4	Results	66
5.5	References	66

Part II – Gamma Ray Lens Mission Design

6.	Other Missions Useful to the GRL Design	68
6.1	Claire and MAX	68
6.1.1	Claire	68
6.1.2	MAX	72
6.1.3	Conclusions	76
6.1.4	References	77
6.2	XEUS	78
6.2.1	The XEUS Mission	78
6.2.2	Gamma Ray Lens: XEUS Similarities	82
6.2.3	Conclusions	83
6.2.4	References	83

7.	Orbit Selection	84
7.1	Orbit Type and Trade-off	84
7.2	L2 Orbit Type	86
7.2.1	Lissajous Orbits	86
7.2.2	Halo Orbits	87
7.3	Orbit Selection Conclusions	89
7.4	References	90
8.	Mission Profile 1 – Soyuz Fregat	91
8.1	Orbit Insertion	91
8.1.1	Direct Insertion	91
8.1.2	L2 Insertion via Highly Elliptical Transfer Orbit	91
8.1.3	Launch Windows	92
8.1.4	Launch Profile Conclusions	93
8.2	Optics Spacecraft (OSC)	94
8.2.1	Payload	94
8.2.2	Subsystems	94
8.2.3	System Budgets	97
8.3	Detector Spacecraft (DSC)	99
8.3.1	Payload	99
8.3.2	Subsystems	100
8.3.3	System Budgets	101

8.4	Mission Configuration	102
8.4.1	Effective Area	103
8.4.2	Sensitivity Analysis	104
8.5	Soyuz Fregat Mission Profile Conclusions	105
8.6	References	106
9.	Mission Profile 2 – Ariane 5	107
9.1	Single Launch Mission Analysis	107
9.1.1	Direct Launch	107
9.1.2	HEO Launch	107
9.1.3	Launch Profile Conclusions	108
9.2	GRL Optics Spacecraft (OSC)	109
9.2.1	OSC Configuration	109
9.2.2	Payload	112
9.2.3	Subsystems	115
9.2.4	Mass Budget	117
9.2.5	Power Budget	119
9.3	GRL Detector Spacecraft	120
9.3.1	DSC Configuration	120
9.3.2	Payload	123
9.3.3	Subsystems	125
9.3.4	Mass Budget	125
9.3.5	Power budget	126

9.4	GRL Mission Configuration	127
9.4.1	Mission Architecture	127
9.4.2	Link Budget and Ground Segment	131
9.4.3	Laue Lens Effective Area	134
9.4.4	Sensitivity Analysis	135
9.5	Ariane 5 Mission Profile Discussion	136
9.6	Ariane 5 Mission Profile Conclusions	141
9.7	References	141
10.	Future Work and Potential Technology Development Activities	142
10.1	Future Activities	142
10.2	Technology Development Activities	144
10.3	References	146
11.	Appendices	147
11.1	Appendix A - Soyuz Launchers; Current Status and Proposed Upgrades for use to L2	147
11.2	Appendix B - Point Spread Function Size – Derivation	152
11.3	Appendix C - Structural Requirements for the Gamma Ray Lens	155
11.4	Appendix D – XEUS Mission and MSC Design	160
11.5	Appendix E – Ariane 5 GRL Systems Mass Budget	163
11.6	Appendix F - Margin Philosophy for Assessment Studies	166

1. Introduction

The Science Payloads and Advanced Concepts Office has introduced the idea of performing Technology Reference Studies (TRS) in order to recognise and encourage the development of new technology concepts for possible future scientific missions. There are four primary areas of investigation in the TRS programme; Planetary, Solar, Astrophysics and Fundamental physics missions.

As part of the Astrophysics missions theme, it has been decided to include the preliminary study of a gamma ray focuser. This study will aim to establish the advances in instrumentation required to make such a mission viable in the future.

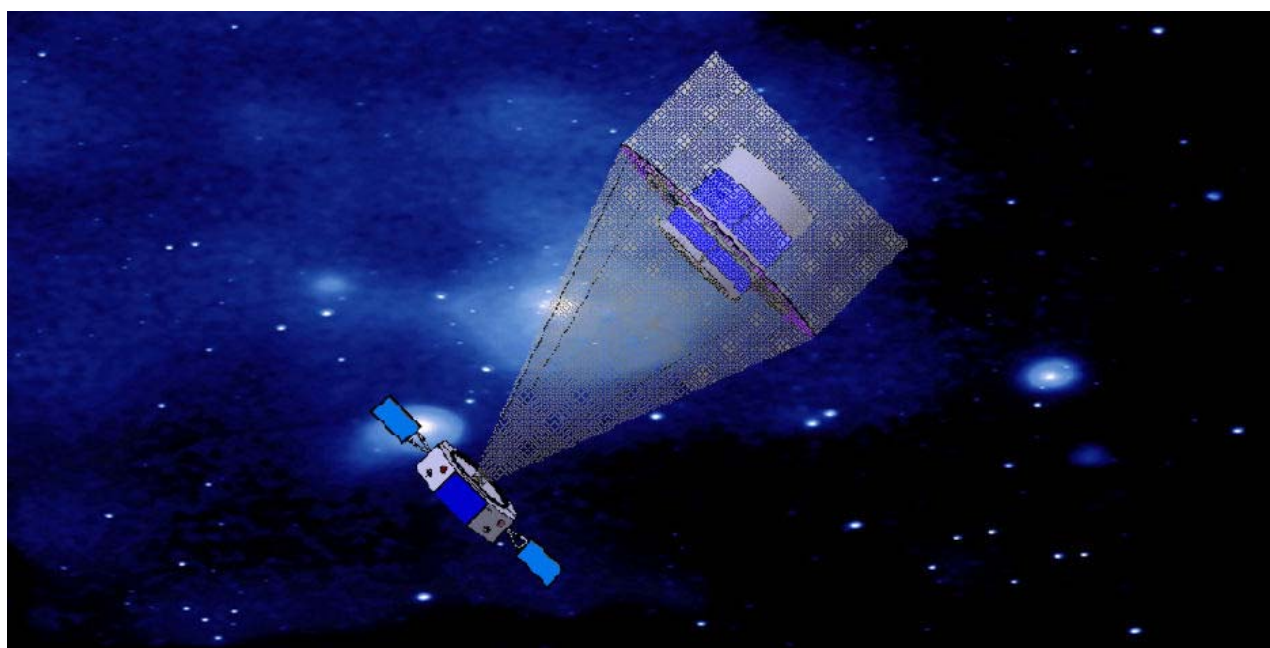
The progression of gamma ray astronomy relies on the development of higher sensitivity instrumentation. Current technologies utilised in the field operate in the background-limited regime and have thus reached a critical point in their development. Any further increase in instrument sensitivity requires an unreasonable increase in spacecraft mass, resulting effectively in unviable space missions. This suggests the need to develop a gamma ray focuser – an optic capable of concentrating gamma rays onto a small detector, thus minimising background and maximising sensitivity.

This report will detail the scientific justification of such a mission, describing the potential return from the use of a ‘Gamma-Ray Lens’. The various principles capable of focusing gamma rays will be introduced and, from the conclusions drawn, a baseline mission will be investigated. The ultimate aim of this report will be to highlight areas for future technology development that are mission enabling for the Gamma Ray Lens, with potential technology transfer to other scientific missions.

PART I

THEORETICAL ASPECTS

OF THE GAMMA RAY LENS MISSION



2. A Reference Science Case for the Gamma Ray Lens

It is important that, in order to establish a baseline for the Gamma Ray Lens (GRL) science mission, the scientific objectives of the mission are firmly understood and, from these objectives, mission drivers can be extracted. It is this set of drivers that will determine the overall configuration and baseline design of the mission. As the primary aim of the GRL is to provide a mission with unprecedented sensitivity in the gamma-ray regime, particular note is made to source fluxes and energies of interest.

Many astrophysical objects have been recognised to be of scientific interest in the gamma-ray regime. Supernovae, compact objects and galactic binary systems, active galactic nuclei, gamma ray bursts and solar flares to name but a few. These target sources allow us to concentrate the gamma ray focuser requirements, using the physical radiative processes of the phenomena to recognise energies and wavelengths of interest to the astronomer.

It has been noted [1][2] that the energy range of 50 keV to 1.2MeV contains many interesting astrophysical features worthy of study and has, to date, been unexplored in detail. Current sensitivity levels have been unacceptable for studying these energies due to the low ($\sim 10^{-7}$ ph.cm⁻².s⁻¹) photon flux. A more sensitive breed of instrument is required to study this band. Such a broad range of energies, however, also suggests the requirement of different types of optic. An instrument designed for hard x-ray/soft gamma ray astronomy, for example, is likely to have a very different design for one aiming to study higher energy gamma rays. It is also important to note that there are two types of gamma ray emission of interest. Line emission and continuum emission.

2.1 Sources of interest in the Soft Gamma Ray regime

2.1.1 Supernovae Type Ia

It is evident that one of the most interesting prospects of gamma ray focusing is the verification of Supernovae Type Ia (SNe Ia) models. Current observations are unable to distinguish between the proposed models and it is suggested that sensitive spectroscopy of the ⁵⁶Ni decay chain via its gamma ray line emission can settle this argument. It is widely believed that this decay chain powers the light curves of supernovae, although successful modelling of such processes are impossible due to the chaotic nature of the supernovae burning fronts [3]. Direct observations of the SNe Ia products are the only way to determine the true nature of this phenomenon.

Given a telescope capable of exploring distances of 50 – 100 Mpc, it is expected that 3-5 SNe Ia can be detected and explored per year of operation. SNe Ia are not only interesting for study in their own right, but also hold prospects for cosmology and in the use as standard candles. They have the potential of being used to measure ‘Dark Energy’ and cosmological constants and, as such, perhaps hold more scientific value than some other astrophysical phenomena that will be discussed.

158 keV (^{56}Ni)
270 keV (^{56}Ni)
847 keV ($^{56}\text{Co} - ^{56}\text{Fe}$)

481 keV, 750 keV, 812 keV (^{56}Ni)
1238 keV ($^{56}\text{Co} - ^{56}\text{Fe}$)

Other supernovae types occur more frequently than SNe Ia but due to the optical thickness of the surrounding ejecta, they are intrinsically faint in the gamma ray regime. This faintness limits the observations to the local group of galaxies that, in turn, limits the likelihood of an event occurring during the mission lifetime.

Light curve models alone cannot uniquely constrain the properties of SNe, as models yielding similar light curves may give rise to different synthetic spectra (e.g., Iwamoto et al. 1998) [4]. High sensitive gamma ray spectroscopy of other SNe types could provide deeper insight into the core collapse physics of stars by directly observing the products of explosive nucleosynthesis. Figure 2.1 clearly shows how determining the luminosity of photons at a given energy could aid in refining supernovae models.

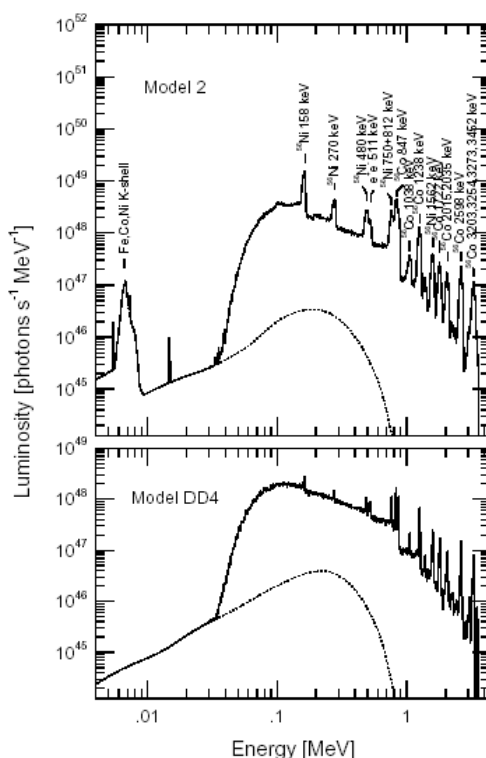


Fig. 2.1 Comparison of expected 20 day spectra from two separate SNe Ia models.

The other types of SNe most likely viewed are SNe Ib and Ic. They lose a large proportion of their opaque envelopes and, in a range of 30 Mpc, are likely to occur one every 2-4 years. Similar lines to those viewed in SNe Ia will be observable. The ^{44}Ti lines of 68 and 78 keV in core collapse remnants, where most heavy elements in the universe are created through the process of nucleosynthesis, would also be of interest to the science community.

2.1.3 Classical Novae

Classical novae emit gamma rays due to the radioactive decay of elements produced in the explosion. Both continuous and line emission will be evident, where the continuous emission is expected to be as a result of the comptonisation of the 511 keV e^+e^- annihilation line [6]. Radioactive elements, which will produce line emission if present in classical novae, are ^{13}N , ^{18}F , ^7Be , ^{22}Na and ^{26}Al . Information about the composition of the white dwarfs involved with classical novae can be obtained through establishing which nuclei are present and in what quantities. The composition of the white dwarf is highly dependent on the yields of radioactive nuclei.

Two very interesting energy lines associated with classical novae are 478 keV and 1275 keV for CO and ONe type novae respectively. The 478 keV line has a rise time of 5 days to 2 weeks and has a photon flux of $1-2 \times 10^{-6} \text{ ph.cm}^{-2}.\text{s}^{-1}$ at 1kpc with an exponential decay over a period of 77 days. The higher energy line at 1275 keV in ONe novae has a greater flux of $2 \times 10^{-5} \text{ ph.cm}^{-2}.\text{s}^{-1}$ at 1kpc with its exponential decay lasting over 3.5 years. The ONe emission would provide a better-sampled spectrum due to this larger flux, although the higher energy poses problems to gamma ray focussing, technologically.

The main attraction of viewing classical novae in the gamma ray regime is the penetrative power of gamma rays. Opaque interstellar dust clouds hamper optical observations. As gamma rays penetrate such clouds, all classical novae within the range of the telescope can be studied and observed.

2.1.4 511 keV e^+e^- Annihilation Line

This gamma ray line is extremely common in many astrophysical phenomena such as gamma ray bursts, compact objects, galactic binaries and supernovae. It is also hypothesised to contribute to the galactic and extragalactic diffuse gamma ray background. Being able to conduct sensitive spectroscopy at this energy will allow a great deal of information about the various sources to be obtained. For this reason, an instrument capable of observing this line would allow a broad science case to be established.

The 511 keV emission from a compact object could give a strong indication as to the nature of that object and, in particular, it's surrounding interstellar media. Current Integral observations of this line show a large concentration of annihilation at the galactic centre, although deep

observations of high galactic latitudes and within the galactic plane are yet to be performed. The measured 511 keV flux from the galactic centre is $\sim 10^{-3} \text{ ph.s}^{-1}.\text{cm}^{-2}$ [20]. There is also evidence to suggest that 511 keV will help the investigation of dark matter in the interstellar medium [21]. Direct observation of the 511 keV annihilation line from a compact object is yet to be observed and would therefore be a primary goal of a gamma-ray focusing mission.

Compton backscattering of the 511 keV line has also been observed (Leventhal & MacCallum 1980; Matteson et al. 1991), and is expected to accompany the 511 keV emission from compact objects. The result of this Compton scattering is a series of line-like features which appear in the continua at ~ 170 keV for single backscattering, ~ 102 keV for double backscattering and ~ 74 keV for triple backscattering. Such features would also provide interesting candidates for a gamma ray observatory and would also provide a fuller picture of the processes associated with positron-electron annihilation.

2.1.5 Gamma-Ray Bursts

With the launch of NASA's Swift observatory, a large amount of interest is being generated in the scientific community concerning Gamma-Ray Bursts. One of Swift's objectives is to detect the presence of gamma ray lines in the light curves obtained from the bursts. Current observations by INTEGRAL have not proven the existence of line features in GRBs although there have been reports of possible line candidates. One of the possible areas of interest for the Gamma Ray Lens would be to investigate the existence and, if present, perform spectroscopy of line features in the GRB light curve. Such investigations would require a very fast response from the spacecraft, as well as an observation programme allowing for opportunistic observations.

2.1.6 Polarimetry

In the investigation of the science of a gamma-ray focussing mission it has become apparent that a great deal of interest is placed on the polarisation of radiation from astronomical sources. Such information can give insight into the structure and geometry of the gamma ray source [8]. Polarisation sensitivity enables us to study particle acceleration mechanisms in supernovae remnants, pulsars and black holes. Synchrotron radiation, inverse Compton scattering and Bremsstrahlung are main photon processes and they each produce distinct photon polarisation features. It would be highly interesting to establish whether a polarimeter could be incorporated into the GRL design.

2.1.7 Conclusions

The hard X-ray and soft gamma ray regime in the 50 keV – 1.2 MeV range is highly unexplored and, from the reported investigation, appears to be of interest to high-energy astronomers. The main question is how important is this science and, of course, this question is highly subjective. As stated in 2.1, the general consensus is that Supernovae type Ia observations using a gamma ray focuser would be greatly beneficial. The verification of SNe Ia models could potentially result in advances in cosmology and the science of ‘Dark Energy’. So, not only is it clear that general observations of astrophysical phenomena are appealing to the astronomer, but there are key observations that could be planned in order to advance scientific theory.

Also, investigation of the positron-electron annihilation line at 511 keV would be highly beneficial. Many astrophysical objects emit radiation of this energy, including SNe Ia. Spectroscopy of this line, coupled with the three inverse Compton scattered annihilation lines, will provide important information about the media surrounding a wide range of interesting sources. A key goal of the Gamma Ray Lens mission will be to verify the emission of 511 keV photons from compact objects, an observation yet to be made with previous missions.

The telescope will require a sensitivity of approximately $10^{-7} - 10^{-8} \text{ cm}^{-2}\text{s}^{-1}$ for 3σ detection in 100 ks for line emission. The exact observation time will depend very much on the science objectives of the mission, and the gamma ray flux from the astrophysical source.

Another important distinction that should be made early in the GRL project should be whether the mission objectives require a gamma ray imager or a gamma ray concentrator. Observations in the gamma ray regime are very often of point sources and therefore do not require the resolution of fine structure in astrophysical phenomena. In such cases, an imager is not required but, in order to decrease the background contribution, a concentrator is favourable.

In conclusion, I believe that there is a significant amount of science to be done with a mission capable of focusing gamma rays. The worth of the mission, however, is highly subjective. Should this mission be a ‘smaller, faster, cheaper’ mission, or does it warrant an investment of ESA Cornerstone class? Investigating the potential scientific achievements for various levels of investment should give a clearer indication of the worth of the Gamma Ray Lens.

2.2 Preliminary Science Requirements Applicable to the GRL

There are two primary science targets for the Gamma Ray Lens.

- 1) Sources associated with the 511 keV positron-electron annihilation line.
- 2) Supernovae type Ia and other regions of explosive nucleosynthesis.

This leads to three separate energy bands of interest.

- 1) 50-200 keV, covering the single, double and triple Compton backscattering of the 511 keV line
- 2) 460-522 keV, covering the 511 keV line as well as the 481 keV ^{56}Ni line from Supernovae Ia.
- 3) 825-910 keV, focusing on the strong 847 keV $^{56}\text{Co} - ^{56}\text{Fe}$ line from Supernovae Ia.

Even though these are the primary lines of interest in the stated energy bands, there are many other lines of interest in these regions that would be of interest to many astronomers. For example, the titanium lines at 68 and 78 keV from core collapse remnants and a line at 478 keV that occurs in galactic novae. The reason behind choosing the 847 keV line from Supernovae Ia as the primary target line is due to the longer (~ 77 day) half life of Co compared to the ~ 7 day half-life of the 158 keV Ni line. The longer decay time allows for a longer observation and, as such, greater sensitivity and a better picture of time evolution of the light curve. Note that the 158 keV line is also observed if the 50-200 keV band is covered.

It should be noted that there are some concerns over the ability of using the 847 keV line as a means of distinguishing one SNe Ia model from another as the various models have only subtle difference between them. However, the results obtained by the GRL spectrometer would provide the first real data with which a SNe Ia model can be constructed and, as such, will prove a very useful tool to members of the community interested in this field of study. Cosmologists and astrophysicists will no longer have to rely on theoretical models alone.

The extremely low photon flux from such sources at gamma-ray energies demand very high sensitivity instrumentation if spectroscopy is to be conducted. The Cosine report [15] for SCI-A recommends that a sensitivity of a few times $10^{-7} \text{ ph.cm}^{-2}\text{s}^{-1}$ is the basic requirement to conduct basic spectroscopy, with a few times $10^{-8} \text{ ph.cm}^{-2}\text{s}^{-1}$ much more desirable.

When defining the effective area requirement, the following is considered. The 847 keV line from type 1 supernovae has a half-life of ~ 77 days. A total observation of a source lasting 80 days, therefore, should be adequate to follow the light curve evolution of the $^{56}\text{N} \rightarrow ^{56}\text{Co}$ decay chain. It is expected that 847 keV flux of $10.4 \times 10^{-5} - 1.2 \times 10^{-5} \text{ photons.cm}^{-2}\text{s}^{-1}$ from Type Ia supernovae at distances of 10-15 Mpc will be observed, according to a series of different models [23]. For the purpose of this argument, an average flux of $1 \times 10^{-6} \text{ photons.cm}^{-2}\text{s}^{-1}$ will be assumed, as Supernovae at greater distances than 15 Mpc, up to 100 Mpc, would also be of interest to the GRL mission.

In order to adequately establish the time evolution of this spectrum, the 80-day observation should be split into a series of time bins or ‘snapshot’ observations. It is assumed that approximately 1000 photons per time bin are required in order to perform modest resolution spectroscopy.

Longer integration times per snapshot will allow Laue lenses with smaller effective areas to be used. Longer time integrations also increase the sensitivity of the instrument. However, longer observation times introduce more systematic detector errors, as well as lessen the number of snapshots taken of the Supernovae over the course of the 80-day observation. For example, an integration time of 1×10^6 seconds allows ~ 7 observations over 80 days with an effective area of just 1000 cm^2 required for modest spectroscopy.

A shorter time integration is more desirable per snapshot in order to effectively determine the time evolution of the ^{56}Ni light curve in type 1 supernovae. The greater the number of snapshot frames over the course of the observation, the better understanding of the light curve evolution can be obtained. Based on the above assumptions, a time bin of 2×10^5 seconds is therefore recommended for the GRL mission requirements, leading to a minimum effective area requirement of 5000 cm^2 at 847 keV.

The flux of 511 keV e^+e^- annihilation radiation varies depending on the gamma-ray origins. The majority of observed sources have had a flux in the order of $\sim 10^{-4} - 10^{-3} \text{ photons.cm}^{-2}\text{s}^{-1}$ [24]. To date, there have been no confirmable observations of 511 keV emission from point sources, however, so one of the main GRL objectives would be to verify this. Observation times in the order of 1×10^6 seconds are expected for most 511 keV sources. An effective area of $\sim 1 \text{ m}^2$ at 511 keV, observing a flux of $1 \times 10^{-6} \text{ photons.cm}^{-2}\text{s}^{-1}$ over an integration time of 1×10^6 seconds, will result in $\sim 10,000$ photons being detected.

The majority of sources of interest are point sources. As such, focusing, and not imaging is the requirement for the mission. A high ($30''$) angular resolution is necessary. The spacecraft must be able to observe any point in the sky within a 12-month period and any point in the sky at any time except for a cone with a 30-degree half angle around the sun (figure 2.2)

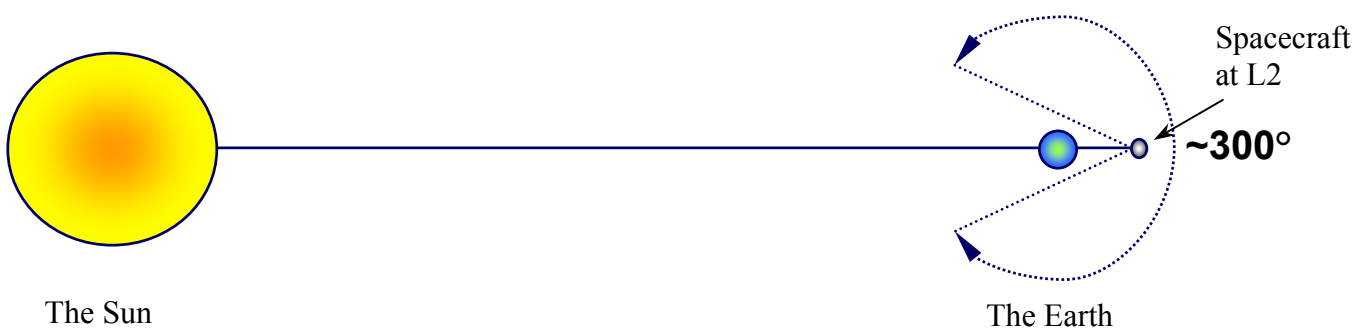


Fig. 2.2 GRL sun acceptance angle

2.3 The INTEGRAL Mission

2.3.1 Mission Summary

The ESA scientific mission INTEGRAL [22] (The International Gamma-Ray Astrophysics Laboratory) is dedicated to fine spectroscopy ($E/\Delta E = 500$) and fine imaging (angular resolution = 12 arcmin FWHM) of celestial gamma-ray sources in the energy range 15 keV to 10 MeV with concurrent source monitoring in the X-ray (3 - 35 keV) and optical (500 - 850 nm) energy bands. The range of astronomical objects and phenomena addressed through INTEGRAL science includes:

- Compact Objects
- Extragalactic Astronomy
- Stellar Nucleosynthesis
- Galactic Structure
- The Galactic Centre
- Particle Processes and Acceleration
- Identification of High Energy Sources
- Serendipitous Discoveries

INTEGRAL was selected by the ESA Science Programme Committee on 3 June 1993 as a medium size scientific mission (M2) of the Horizon 2000 programme to be launched in 2002. The mission was conceived as an observatory led by ESA with contributions from Russia (PROTON launcher) and NASA (Deep Space Network ground station). The nominal lifetime of the observatory was 2 years, extendible to 5 years. Most of the observing time is made available to the worldwide scientific community. Table 1 presents a summary of key mission parameters.

Objectives	Gamma-ray astronomy 15 keV – 10 MeV with high-resolution spectroscopy and fine imaging. Concurrent monitoring in X-ray (3-35 keV and optical (500-600nm) bands
Payload	Main Instruments: Germanium Spectrometer (SPI) Cadmium Telluride/Caesium Iodide imager (IBIS) Monitors: X-ray Monitor (JEM-X) Optical Monitoring Camera (OMC)
Field of View (fully coded)	9°x9° (IBIS), 16° (SPI) 4.8° (JEM-X), 5°x5° (OMC)
Angular Resolution (FWHM)	12' (IBIS), 2.5° (SPI) 3' JEM-X, 25'' (OMC)
Spectral Resolution ($\Delta E/E$)	0.18% @ 1.3 MeV (SPI) 9% @ 100 keV (IBIS) 1.2% @ 10 keV (JEM-X)
Source location radius (10σ)	<1.3° (SPI), <60'' (IBIS), <30'' (JEM-X), 6'' (OMC)
Continuum Sensitivity (3σ in 10⁶ s)	5×10^{-7} ph.s⁻¹.cm⁻².keV⁻¹ @ 100 keV (IBIS) 1.5×10^{-7} ph.s⁻¹.cm⁻².keV⁻¹ @ 1 MeV (SPI) 1.3×10^{-5} ph.s⁻¹.cm⁻².keV⁻¹ @ 6 keV (JEM-X)
Line Sensitivity (3σ in 10⁶ s)	2×10^{-5} ph.s⁻¹.cm⁻² @ 100 keV (IBIS) 5.1×10^{-6} ph.s⁻¹.cm⁻² @ 1 MeV (SPI) 1.7×10^{-5} ph.s⁻¹.cm⁻² @ 6 keV (JEM-X)
Orbit and Launcher	Highly eccentric orbit (HEO) Launcher: PROTON Launch date: 17 October 2002 Period: 72h Inclination: 51.6° Perigee: 9000 km Apogee: 155 000
Ground Stations Time above 40 000 km	Redu (B) and Goldstone (USA) ~90%
Spacecraft Absolute Pointing Error Launch dry mass Science Instrument Mass Science Instrument Power Telemetry Dimensions (satellite)	Three-axis stabilized bus common with XMM ≤5' (Y,Z axes), ≤15' (X axis (roll)) 3600 kg 2087 kg 721 W 85.8 kbits/s science data (incl housekeeping) LxWxH: 4x4x6 m (Solar arrays undeployed)
Operational Mode Nominal Mission Lifetime Design Lifetime	Observatory 2 Years 5 Years

Table 2.1 INTEGRAL mission parameters at launch

2.3.2 Scientific Objectives

Gamma-ray astronomy embraces a number of gamma-ray continuum and gamma-ray line processes: nuclear excitation, radioactivity, positron annihilation and Compton scattering; and an even greater diversity of astrophysical objects and phenomena: nucleosynthesis, nova and supernova explosions, the interstellar medium, cosmic-ray interactions and sources, neutron stars, black holes, gamma-ray bursts, active galactic nuclei and the cosmic gamma-ray background. In order to study all of these objects, INTEGRAL combines fine spectroscopy and imaging of gamma-ray emissions in the energy range 15 keV to 10 MeV with concurrent monitoring in X-rays (4-35 keV) using JEM-X, and optical (500-600 nm) using OMC. Fine spectroscopy over the entire energy range permits spectral features to be uniquely identified and line profiles to be determined for physical studies of the source region. The last high-resolution space instrument, that on HEAO-3 in 1979-80, was 100 times less sensitive than INTEGRAL.

2.3.3 Scientific Payload

The four instruments comprising INTEGRAL's scientific payload weigh 2087 kg, making this the heaviest payload launched by ESA. This is largely due to the need to shield the detectors from background radiation in order to retain their sensitivity. The instruments are housed in a science-payload module that was integrated and tested as an independent unit before being incorporated into the spacecraft. The interface with the satellite bus was designed to be as simple as possible in order to reduce integration time and cost. In addition to the four telescopes, a particle radiation monitor measures charged particles fluxes in the spacecraft orbital environment. The particle data are used in assessing the background and hence the sensitivity and performance of the instruments.

2.3.3.1 SPI (SPectrometer on INTEGRAL)

The spectrometer SPI performs spectral analysis of gamma-ray point sources and extended regions in the 20 keV to 8 MeV energy range with an energy resolution of 2.2 keV (FWHM) at 1.33 MeV. This is accomplished using an array of 19 hexagonal high purity Germanium detectors cooled by a Stirling cooler system to an operating temperature of 85 K. A hexagonal coded aperture mask is located 1.7 m above the detection plane in order to image large regions of the sky (fully coded field of view = 16°) with an angular resolution of 2° . In order to reduce background radiation, the detector assembly is shielded by a veto (anticoincidence) system that extends around the bottom and sides of the detector and almost up to the coded mask. The aperture (and hence the contribution from cosmic diffuse radiation) is limited to $\sim 30^\circ$. A plastic veto is provided below the mask to further reduce the 511 keV background.

Scientific topics to be addressed by the Spectrometer are:

- Nucleosynthesis Processes and Supernova Dynamics
- Interstellar Processes
- Compact Objects
- Active Galactic Nuclei
- Cosmic Diffuse Background Radiation and Diffuse Continuum Emission
- Cosmic Gamma-Ray Bursts

Energy Range	20 keV to 8 MeV
Detector Area	500 cm²
Spectral Resolution	~450 (i.e. 2.33 keV FWHM @ 1.33 MeV)
Field of View (corner to corner)	16° fully coded
Angular Resolution (point sources)	2.5° FWHM
Continuum Sensitivity (3σ in 10⁶ s @ 1MeV)	1.5x10⁻⁷ ph.s⁻¹cm⁻²keV⁻¹
Line Sensitivity (3σ in 10⁶ s)	1.5x10⁻⁵ ph.s⁻¹cm⁻²keV⁻¹ @ 1 MeV 2.8x10⁻⁵ ph.s⁻¹cm⁻²keV⁻¹ @ 511 keV
Timing Accuracy (3σ)	0.123 ms
Mass	1309 kg
Power (sun/eclipse)	385/110 W
Data rate (solar maximum)	15.8 kbps
Data rate (solar minimum)	20.2 kbps

Table 2.2 SPI Instrument parameters at launch

2.3.3.2 IBIS

The Imager IBIS (Imager on Board the INTEGRAL Satellite) provides the diagnostic capabilities of fine imaging (12 arcmin FWHM), source identification and spectral sensitivity to both continuum and broad lines over an energy range from 15 keV to 10 MeV. The instrument uses a tungsten coded aperture mask located 3.2 m above the detection plane. Since diffraction is negligible at gamma-ray wavelengths, the angular resolution obtainable with a coded mask telescope is limited by the spatial resolution of the detector array. The Imager design takes advantage of this by utilizing a large number of spatially resolved pixels, implemented as physically distinct elements. There are two focal planes: a 2600 cm² front layer of CdTe pixels, each 4×4×2 mm (width×depth×height); and a 3100 cm² layer of CsI pixels, each 9×9×30 mm. The CdTe array (ISGRI) and the CsI array (PICsIT) are separated by 90 mm. These detectors provide the wide energy range and high sensitivity continuum spectroscopy required for

INTEGRAL. The division into two layers allows the paths of the photons to be tracked in 3D as they scatter and interact with more than one pixel. Events can be categorized and the signal to noise ratio improved by rejecting those which are unlikely to correspond to real (celestial) photons (e.g. towards the high end of the energy range). The aperture is restricted by a lead shielding tube and shielded in all other directions by an active BGO scintillator veto system. Scientific topics to be addressed by the Imager:

- Galactic Astrophysics
- Explosive and Hydrostatic Nucleosynthesis
- High Energy Transients and Gamma-Ray Bursts
- Extragalactic Astrophysics

Energy Range	15 keV to 10 MeV
Detector Area	2600 cm² (CdTe), 3100 cm² (CsI)
Spectral Resolution	~9% @ 100 keV
Field of View	9°x 9° fully coded
Angular Resolution	12 arcmin FWHM
Continuum Sensitivity (3 σ in 10 ⁶ s @ 100 keV, $\Delta E=E/2$)	5x10⁻⁷ ph.s⁻¹cm⁻²keV⁻¹
Line Sensitivity (3 σ in 10 ⁶ s @ 100 keV)	2x10⁻⁵ ph.s⁻¹cm⁻²
Timing Accuracy (3σ)	0.92 ms
Typical Source Location (10σ source)	< 1 arcmin
Mass	677 kg (+96kg for tube inside PLM)
Power (sun/eclipse)	240/0 W
Data rate (solar maximum)	59.8 kbps
Data rate (solar minimum)	56.8 kbps

Table 2.3 IBIS Instrument parameters at launch

2.3.3.3 JEM-X

The Joint European X-Ray Monitor JEM-X supplements the main INTEGRAL instruments (Spectrometer and Imager) and plays a crucial role in the detection and identification of the gamma-ray sources and in the analysis and scientific interpretation of INTEGRAL gamma-ray data. JEM-X makes observations simultaneously with the main gamma-ray instruments and provides images with arcminute angular resolution in the 3 to 35 keV prime energy band. The baseline photon detection system consists of two identical high-pressure imaging microstrip gas chambers (1.5 bar, 90% Xenon + 10% Methane), at nominal gas gain of 1500. Each detector unit views the sky through its coded aperture mask located at a distance of ~3.2 m above the detection plane. Scientific topics to be addressed by JEM-X are concerned with the study of

sources, which draw upon strengths of JEM-X such as its broad spectral coverage and its ability to detect and resolve cyclotron lines. These include:

- Active Galactic Nuclei
- Accreting X-Ray Pulsars
- X-Ray Transients
- Black Hole Candidates

Energy Range	3 keV to 35 keV
Detector Area (2 units)	500 cm² each
Energy Resolution	1.2 keV @ 100\ keV
Field of View	4.8° (dia) fully coded
Angular Resolution	3 arcmin
Continuum Sensitivity (3σ in 10⁶ s @ 6keV)	1.3x10⁻⁵ ph.s⁻¹cm⁻²keV⁻¹
Line Sensitivity (3σ in 10⁶ s @ 6 keV)	1.7x10⁻⁵ ph.s⁻¹cm⁻²
Timing Accuracy (3σ)	122μs
Typical Source Location (10σ source)	< 30''
Mass	65 kg
Power (sun/eclipse)	50/0 W
Data rate (solar maximum)	7.9 kbps
Data rate (solar minimum)	7.0 kbps

Table 2.4 JEM-X Instrument parameters at launch

2.3.3.4 OMC

The Optical Monitoring Camera OMC uses a passively cooled CCD operated in frame transfer mode. The CCD has 2055 × 1056 pixels (1024 × 1024 in the image section). The CCD is located in the focal plane of a 50 mm diameter telescope that includes a Johnson V-filter and covers the wavelength range 500 to 850 nm. The instrument is mounted close to the top of the payload module structure. The OMC observes the optical emission from the prime targets of the INTEGRAL gamma-ray instruments. It offers the first opportunity to make long observations in the optical band simultaneously with those at X-ray and gamma ray energies. This capability provides invaluable diagnostic information on the nature and the physics of the sources over a broad wavelength range. Multi-wavelength observations are particularly important in high-energy astrophysics where variability is typically rapid. The wide band observing opportunity offered by INTEGRAL is of unique importance in providing for the first time simultaneous observations over seven orders of magnitude in photon energy for some of the most energetic objects including AGN, supernovae, active binary systems, black hole candidates, high energy transients, serendipitous sources and gamma-ray bursts.

2.3.4 Sensitivity

The sensitivity values quoted in tables 2.1, 2.2, 2.3 and 2.4 were the predicted values prior to launch. Since launch and in-orbit calibration, the sensitivity has been refined. Figure 2.3 gives the current 3σ sensitivity in 10^5 seconds.

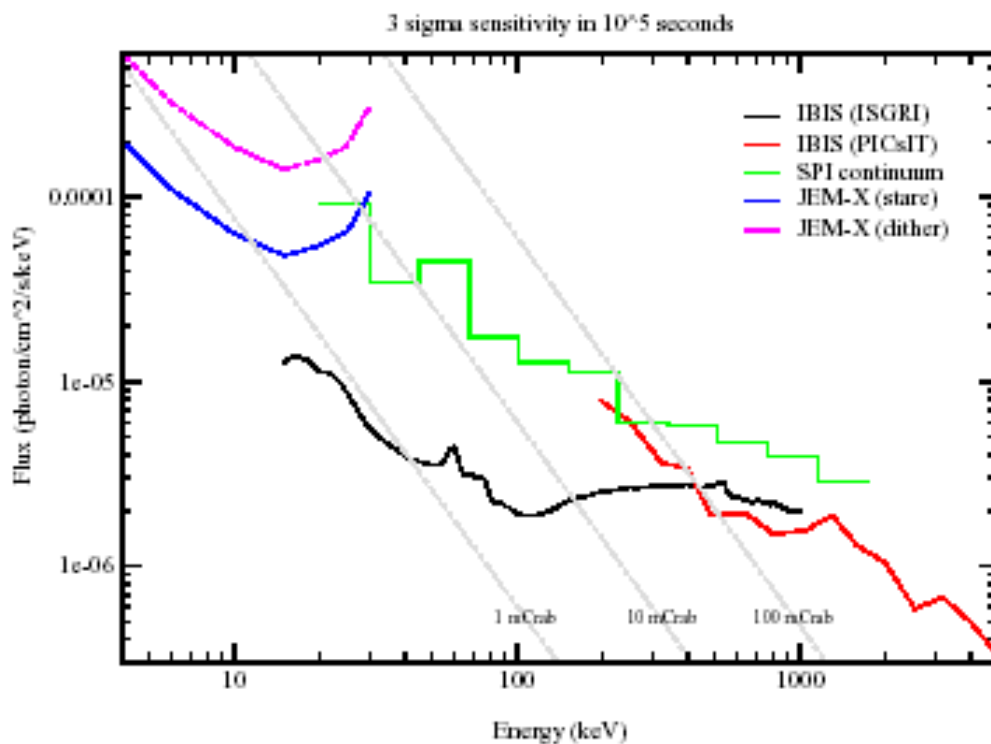


Fig. 2.3 Sensitivity of the INTEGRAL prime instruments

2.3.5 Spacecraft

The spacecraft consists of a service module (bus) containing all spacecraft subsystems and a payload module containing the scientific instruments. The simplicity of the interface between service and payload module was a major design driver. The electrical interface is reduced to a power and data handling bus. The modular approach was conceived to allow for parallel development, assembly, integration and test of the two modules. The service module is a rebuild of the unit developed for XMM-Newton, ESA's X-ray Multi-Mirror satellite. It is a closed structure made of composite material (a combination of aluminium and carbon fibre). It houses the satellite systems, including: solar power generation; power conditioning and control; data handling; telecommunications; thermal, attitude and orbit control. The spacecraft was built under ESA contract by a large industrial consortium, led by Alenia Spazio (I) as prime contractor.

2.3.6 Launcher and Orbit

INTEGRAL was launched by a Russian PROTON launcher from Baikonur/Kazakhstan. The total launch mass was ~4000 kg. It was placed into a highly eccentric geosynchronous orbit with a high perigee in order to provide long periods of uninterrupted observation and nearly constant background outside the radiation belts.

The orbital parameters are:

- **Period:** 72 hours
- **Inclination:** 51.6.
- **Perigee:** 9000 km
- **Apogee:** 153 000 km

Scientific observations are conducted whilst the satellite is above an altitude of 40 000 km. This represents ~90 % of the total orbital period.

2.4 References

- [1] Gamma Ray Spectroscopic Imager for Nuclear Astrophysics, R. Griffiths presentation at ESTEC, 2003
- [2] MAX, a gamma-ray lens for nuclear astrophysics, Peter Von Ballmoos et al. Annex 1: The Science of MAX
- [3] A test for the nature of the type Ia Supernova explosion mechanism, Philip A. Pinto et al, The Astrophysical Journal, 551:231-243, 2001
- [4] The type 1C Hypernova SN 2003dh/GRB 0 0329, P.A Mazzali et al, The Astrophysical Journal, 599:L95-L98, 2003
- [5] Gamma Ray emission from type Ia supernovae, J. Isern et al, New Astronomy Reviews 48, 31 –33, 2004
- [6] Gamma Rays from classical novae: expectations from present and future missions, M. Hemanaz, J. Jose, New Astronomy Reviews 48, 35-39, 2004
- [7] Imaging principles and techniques in space-borne gamma ray astronomy, V. Sconfelder, Nuclear Instruments and Methods in Physics Research, 2003
- [8] PoGO: The Polarised Gamma-Ray Observer, S. Larsson, M. Pierce, Nuclear Instruments and Methods in Physics Research, 2003
- [9] Supernova Polarimetry with the VLT: lessons from asymmetry, L. Wang et al, The Messenger (ISSN 0722-66 91), No. 109, p47-51, 2002
- [10] Evolution of the polarisation of the optical afterglow of the gamma ray burst GRB030329, Nature, Volume 426, Issue 6963, pp 157-159, 2003

- [11] Gamma ray lines from cosmic radioactivity, M.D. Leising, Nuclear Physics A621, 1997, 71c-78c
- [12] Spectral distinction between black holes and neutron stars: The contribution of the SIGMA telescope, P. Laurent, M. Denis, Adv. Space Res. Vol 19, No 1, pp. 45-54, 1997
- [13] Gamma Ray Imaging, M. Beijersbergen, Cosine Report, CSC-ODS-TN1, 2004
- [14] Towards the first light for a gamma ray lens, P. Laporte et al, France
- [15] A comparative study of possible future nuclear astrophysics missions, M. Beijersbergen, Cosine Report, CSC-ODS-TN5, 2004
- [16] Status and prospect for polarimetry in high energy astrophysics, M.L. McConnell, J.M. Ryan, New Astronomy Reviews 48, 215-219, 2004
- [17] A CdTe position sensitive spectrometer for hard X- and soft Gamma-ray polarimetry, E. Caroli et al, Nuclear Instruments and Methods in Physics Research A 477 567-573, 2003
- [18] Gamma-Ray TRM Crystal Focussing Requirements, D Lumb, SCI-A/2004.073/Tn/DL, 2004
- [19] CACT μ S: A small CdTe array for a prototype balloon experiment, E. Caroli et al. Nuclear Instruments and Methods in Physics Research A 513 357 – 361, 2003
- [20] INTEGRAL/SPI Observations of Electron-Positron Annihilation Radiation from our Galaxy, B.J. Teegarden et al., American Astronomical Society Meeting 205, #84.07 , 2004
- [21] 511 keV Line Measurements with SPI: INTEGRAL workshop presentation, E. Churazov, ESTEC, January 2005
- [22] INTEGRAL Special Edition, Astronomy and Astrophysics Vol 411, No. 1, November 2003 pp. L1-L460
- [23] Ruiz-Lapuente, P., et al.,1993, ApJ, 417, 547
- [24] Knödlseeder, J. et al., 2005, The all-sky distribution of 511 keV electron-positron annihilation emission. Accepted for publication in Astronomy and Astrophysics.

3. High Energy Focusing Technologies

The aim of section 3 is to summarise two technologies able to focus gamma rays: Firstly, multilayer mirrors, and secondly crystal diffraction. This section will also outline how crystal diffraction can be used to construct an optic capable of focusing high-energy electromagnetic radiation. It has widely been accepted that focussing hard x-rays and γ -rays is highly impractical. High-energy waves interact with matter primarily by incoherent process, resulting in a loss of information about the incident radiation. As a result of this, instrumentation designed for γ -ray astronomy has utilised inelastic interaction processes with coded aperture masks or Compton scattering telescopes. These result in very high background fluxes, as the collecting areas are at least as large as the area of the detectors. As increasing the sensitivity of the instrument requires a larger collecting area, it quickly becomes impractical to make a more sensitive instrument; the size and, consequently, mass of the instrument increase in such a way that the gain in sensitivity is not worth the mass cost.

It is possible, however, to make use of the phase information of the incident photons. γ -Rays incident on high-Z crystalline materials can undergo Bragg and Laue diffraction, introducing the possibility of focusing these rays. A large photon collecting area with a small detection area will result, significantly decreasing background noise. Such a configuration could optimistically lead to sensitivities of $\sim 10^{-7}$ - 10^{-8} ph.cm⁻²s⁻¹keV⁻¹.

There are two main types of crystal diffraction process; Bragg diffraction and Laue Diffraction. In Bragg diffraction, the reflected ray leaves the crystal through the same surface it entered, similar to a reflection, whereas in Laue diffraction the reflected ray is transmitted through the crystal and leaves a different crystal surface to the one it entered.

3.1 Graded Multilayer Mirrors

Multilayer mirror technology is an extension of classical high-energy optics, utilizing the principle of reflection at grazing incidences. Coatings have been used on Wolter I nested shells in order to increase the effective area and reflectivity of these X-ray mirrors, e.g. the gold coating used on XMM-Newton. Typical mirror coatings are effective only up to ~ 10 keV and, depending on the composition of the coating, will change the effective area profile of the optic.

The principle of multilayer coatings arises when trying to further increase the reflectivity of a high-energy optic. Multilayer mirrors are, in fact, the enabling technology of many next-generation high-energy astrophysics missions such as Constellation X and XEUS. Hundreds of layers of material are used in making a multilayer, usually consisting of two materials sandwiched alternately, one after another. The thickness and number of these ‘bi-layers’ significantly affect the response of the coating. This section aims to introduce the concepts behind multilayer mirror coatings and its potential application to a soft gamma ray mission such as the Gamma Ray Lens.

3.1.1 Hard X-ray and Soft Gamma-Ray Astronomy

The reflectivity of single layer optic coatings becomes limited at energies of ≥ 10 keV. The aim of a multilayer coating is to increase this response as far as possible in order to observe higher energies. It is necessary, therefore, to understand the science objectives of such an optic in order to justify the technology development required. Multilayer Mirrors are expected to be able to significantly increase the reflectivity and effective area of high-energy optics to an energy of ~ 200 keV [1].

There are many spectral lines of interest in the hard X-ray, soft gamma-ray regimes. Most notably is the presence of the ^{56}Ni emission at 158 keV in Supernovae Ia. Spectroscopy of the time evolution of this line will prove significant when investigating the mechanisms of SNe Ia, which can be used as standard cosmological candles. ^{44}Ti lines at 68 and 78 keV in core collapse remnants are also of interest.

Another significant set of line-like features in this energy band are the single, double and triple Compton backscatter radiation of the 511 keV line. These features appear at 170, 102 and 74 keV respectively. Investigation of these lines will compliment any observations made of the 511 keV line and will provide valuable information about the media surrounding compact objects.

The nuclear continuum in this energy range is reasonably featureless, although this is yet to be observed with a high spectral resolution by a focusing optic. Observation of the continuum will aid in establishing the background emission at these energies.

3.1.2 Principles of Multilayer Mirrors

3.1.2.1 Bragg Diffraction

High-energy radiation reflects from crystal planes by Bragg diffraction. Fig. 3.1 shows the scattering of a high-energy ray from successive lattice planes at the surface of a crystal.

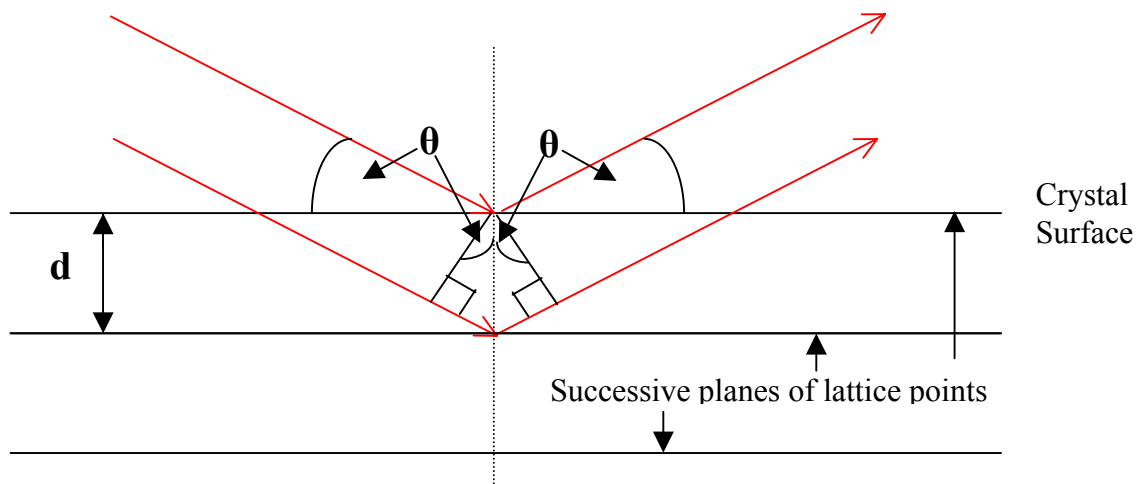


Fig. 3.1 Scattering of high-energy rays from two successive lattice planes at the surface of a crystal.

The rays will be in phase only if the path difference of the rays is an integer number of wavelengths. From the figure, it can be seen, therefore, that:

$$2d \sin \theta = n\lambda \quad [3.1]$$

Where d = distance between successive lattice planes, θ = the angle of reflection (also known as the Bragg angle), n = an integer and λ = the wavelength of the incident radiation. This is known as Bragg's Law. It can be seen from Bragg's Law that θ is governed by the wavelength and hence the energy of the incident photons, as well as the plane spacing and, hence, crystal type.

Bragg's law is used in determining the range of multilayer bi-layer thicknesses.

3.1.2.2 Bi-Layer Interfaces

The perfection of layer interfaces is extremely important in order to maximise the reflectivity and hence effective area of the optic. The effective reflection coefficient at each interface is determined by the optical constants of the material and the perfection of the interface width; a value that characterizes the perfection between layers. The loss of reflectance due to interface imperfections can be extremely large above 100 keV, even at grazing incidence. Material selection is therefore driven by the ability to form stable layers having maximally smooth and sharp interfaces [2], whether by fabrication and deposition of layers, or through material properties. Many layer pairs are under investigation; for example W/Si, Mo/Si, Ni/Ti, Co/Ti, Ni/B₄C, W/B₄C and Ni/C.

3.1.2.3 Bi-layer Thickness and Optimisation

There are many models and investigations into the materials and different combinations of bi-layers. Different combinations of thicknesses result in very different effective area profiles. Figure 3.2 shows a modelled example of the effective area response of two different sets of layers, both using the same material but utilising different bi-layer thicknesses to optimise for different energies [1].

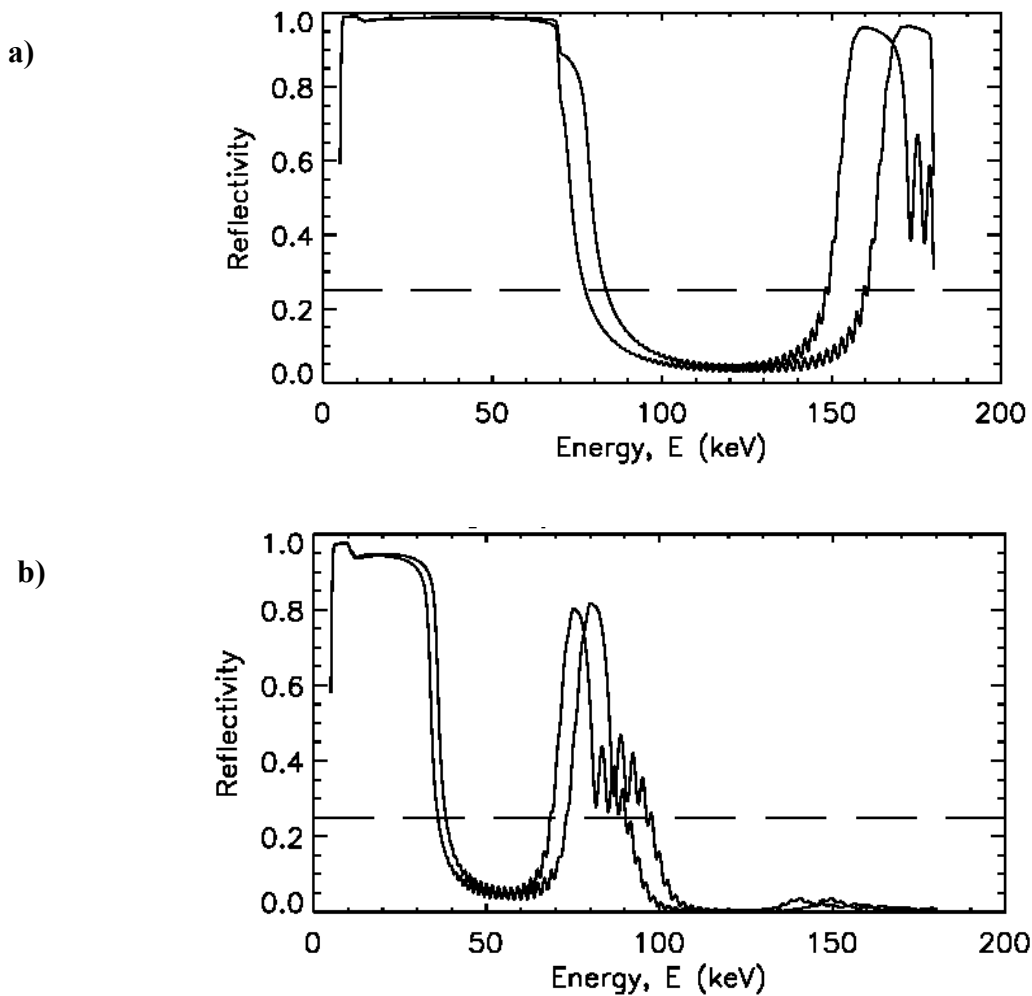


Fig. 3.2 Figures showing two different multilayer designs optimized for different energy bands [1]. a) W/Si multilayer for 155-170 keV b) W/Si multilayer for 70-85 keV. The two curves on each figure show reflectivities at the min. and max. on axis grazing angles.

A method used to increase reflectivity over a large energy band is known as depth grading (fig. 3.3). This is the process of varying the thickness of bi-layers to change the reflectivity profile of the coating. Essentially, each bi-layer is tuned into a different x-ray wavelength, in order to achieve broadband reflectance, in accordance with Bragg's law (equation 3.1). However, Designing a series of layers that increases the reflectivity of a broad energy band results in a lower peak reflectivity. Therefore, it is necessary to decide whether a large continuous coverage is desired from, for example, 50 – 200 keV, or if an optimisation for a number of energy bands is more desirable.

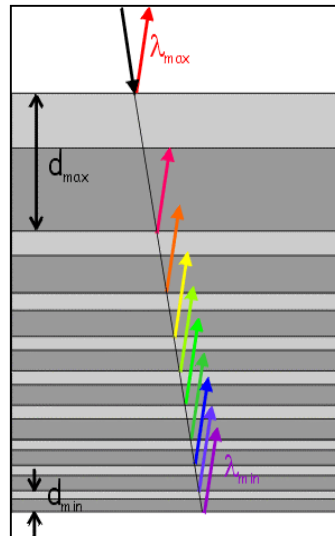


Fig. 3.3 Diagram showing a depth graded multilayer coating and the reflection of different energies from different bi-layer interfaces.

Further investigation is required to establish the materials most suitable for the multilayer coating, the thickness of the layers and the depth-grading profile, in order to optimise the optics for the desired energy bands.

One technique used in the fabrication of multilayers is a deposition process known as DC Magnetron Sputtering [6]. A full description of this method of fabrication is available in the mentioned reference. This process allows one layer of material to be deposited at a time, with the thickness of the layers controlled very precisely. The method is analogous to spray-painting using a can, where the thickness of paint deposited on a surface depends on the speed at which the can is passed over the surface. As mentioned previously, the interface between layers is all-important. Imperfections can result from a variety of material and/or growth dependant mechanisms, for example, the formation of mixed-composition amorphous interlayers by diffusion or by energetic bombardment during growth [7]. The fabrication of multilayers is certainly an area requiring further development.

3.1.3 Optic Design

Current grazing incidence optics methods, such as the Wolter I nested shells as used on XMM-Newton, can be coated with a set of multilayers in order to extend the energy range of the instrument. However, in order to achieve the effective area required to meet the scientific objectives such an optic would be prohibitively massive and, therefore, expensive. The

development of lightweight optics with high angular resolution is necessary for the next generation of high-energy astrophysics missions. Coupling newly developed, lightweight optics with multilayers will allow larger effective areas at higher energies.

3.1.3.1 Silicon Pore Optics

The XEUS mission currently baselines a new, novel type of optic known as Silicon Pore Optics [3]. This type of optic allows for extreme mass and volume reduction, without losing effective area and or resolution. Fig. 3.4a shows the trend of optics technology for resolution versus area density and 3.4b shows the reduction in mass per unit effective area of Silicon Pore Optics. The Silicon Pore Optics used on XEUS show a clear advantage over the other optic technologies with regard to area density and effective area.

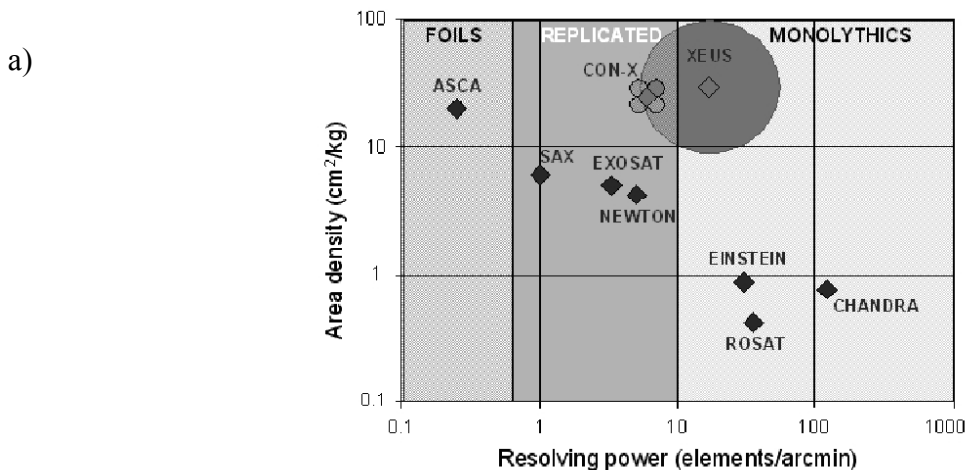


Fig 3.4a The trend of optics technologies for resolution versus area density. Con-X and XEUS break the existing trend in optic technology from previous missions. The areas of circles represent the effective area of the various proposed missions. Effective areas of $< 0.1 \text{ m}^2$ are smaller than the displayed diamonds in this representation.

b)

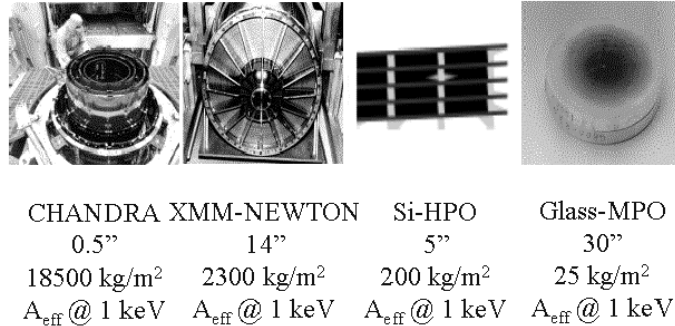


Fig 3.4b Photographs of hardware developed for X-ray missions, together with a summary figure of merit for angular resolution achievable and mass required per unit of effective area. Chandra utilised a glass based mirror and XMM-Newton a series of nested nickel shells. The Si-HPO optics are the Silicon Pore Optics described in this section.

Silicon wafers are used in the construction of the XEUS optics, as silicon is nearly 4x less dense than the nickel used in normal Wolter optics. XEUS, being concerned primarily with energies ≤ 60 keV, will have a multilayer coating optimised for this energy range applied to the silicon wafers before the optic is constructed. The fabrication process is described here.

Fig. 3.5a shows the first step in optic module construction. Ribbed silicon plates, coated with the multilayer and with extremely high surface quality on both sides, are the building blocks of the optic module.

a)

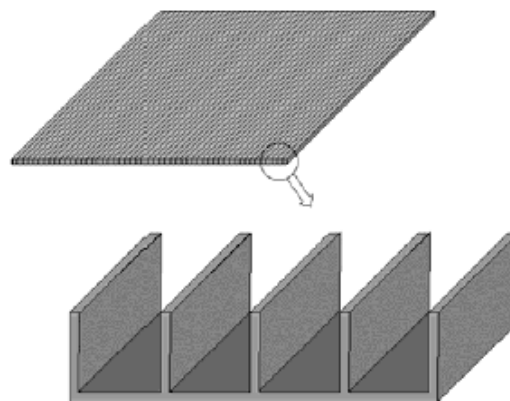


Fig. 3.5a Silicon ribbed plates where the ribs and reflecting plate are only $\sim 200\mu\text{m}$ thick.

A ribbed plate is then stacked onto a precision mandrel with a slumped surface, equivalent to the required radius of curvature for the optic configuration. Several plates are subsequently stacked on top of the curved wafer in the azimuthal direction, to form a single monolithic unit. (Fig 3.5b)

The optics module can then be sealed with another mandrel or detached from the original mandrel. Detachment is preferable due to a mass reduction. This is then known as a ‘sub-petal unit’ (Fig 3.5c).

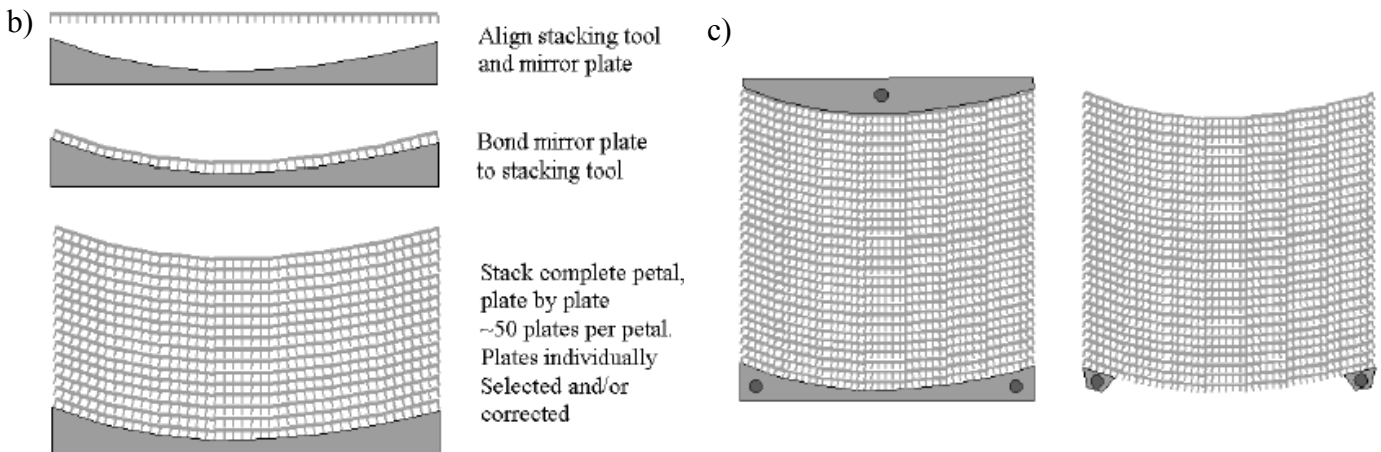


Fig 3.5b Stacking of many silicon plates onto a mandrel. **Fig 3.5c** Options for leaving or removing the forming mandrel.

A number of these ‘sub petal units’ are then integrated, aligned and fixed to create a mirror module. The XEUS mission stacks two such modules in series to form a Wolter I conical approximation in order to conduct true imaging, thus forming a Mirror Petal. XEUS would make use of ~48 mirror Petals to achieve its goal of an effective area of ~10 m². Figure 3.5d shows the hierarchy of fabrication for the complete mirror assembly for XEUS. Note the centre 4 x 4 petals in the optical bench are left empty.

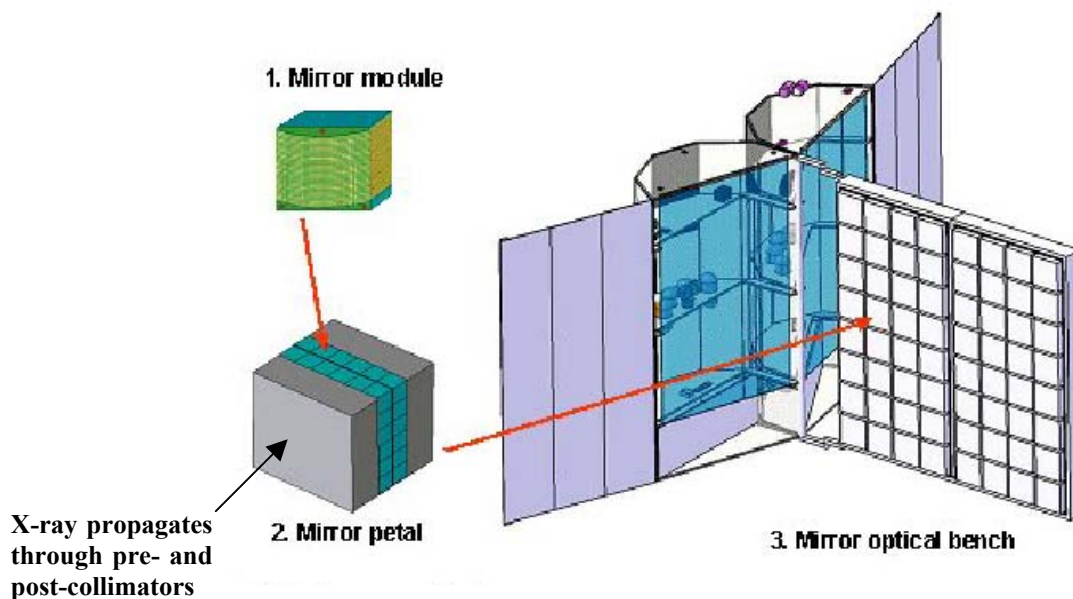


Fig. 3.5d The hierarchy for fabrication of the complete mirror assembly, starting from a module of mirror plates built into a petal containing many modules of mirror plates, built in to a petal containing many modules of mirror pairs. Finally, several petals are combined into the optics of desired area.

The Silicon pore optics described here could have potential application for higher energies than those observed with XEUS through the optimization of the multilayer coating. Optimising the coating for the 50 – 200 keV energy band requires investigation. Focal length also needs to be taken into consideration.

3.1.3.2 Focal Length Considerations

Figure 3.6a shows a model of a multilayer coated optic at varying focal lengths. Even though the model only shows a maximum focal length of 30m, it is evident that a larger focal length is beneficial. Perhaps the most important increase in effective area occurs at regions of very low reflectivity. Figure 3.6a shows clearly that the region between 80 and 125 keV has a significant increase in effective area at a focal length of 30 m. Reflectivity of high energy photons from a surface increases with smaller grazing angles. As the focal length is increased, the grazing

angles become smaller, thus increasing the number of photons reflected from the multilayer and increasing the effective area of the optic at these energies.

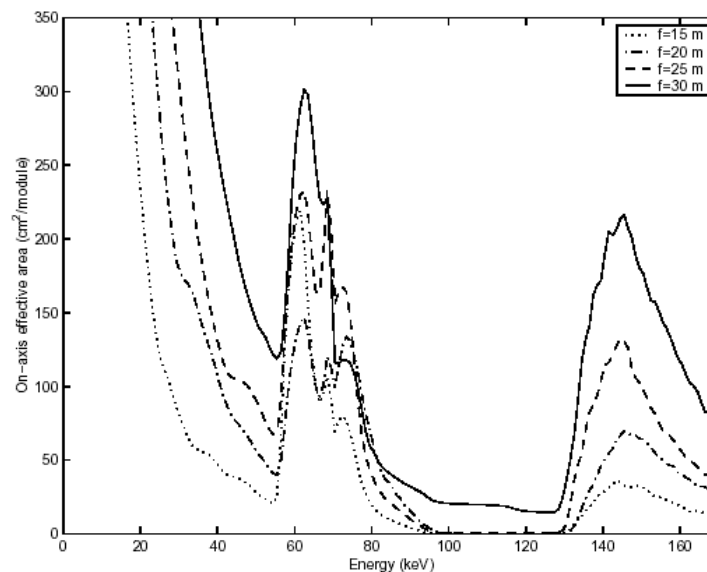


Fig 3.6a *Dependence of the on-axis effective area on focal length. All four designs consider W/Si multilayer coatings. The collecting efficiency of a 5mm CdZnTe detector was assumed for this model. [1]*

The XEUS mission also underwent a similar trade-off study, showing a significant increase in effective area for a larger focal length (Fig 3.6b). A larger focal length in turn, however, requires a greater separation between formation flying spacecraft. A larger distance between craft results in a more difficult metrology and attitude control system that, for extreme distances, could be prohibitive.

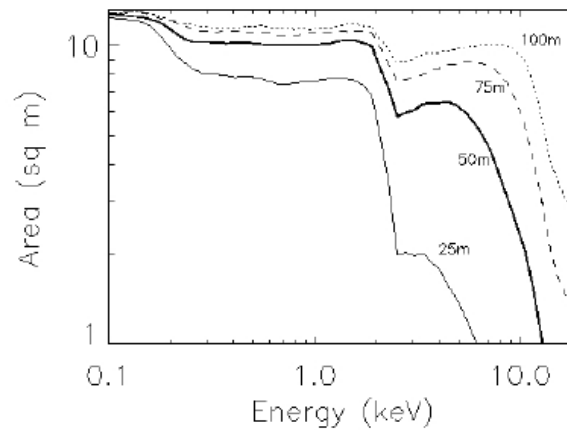


Fig 3.6b The change in effective area resulting from different focal length choices for the XEUS mission.

3.1.4 Conclusions

The use of multilayers as a coating on a Silicon Pore Optic will be demonstrated on the XEUS X-ray observatory mission, extending the energy observed to ~60 keV. This technology is expected to be extendible at least to 200 keV, with reports of perhaps extending this to even higher energies [5]. It has been established that there is a scientific case for exploring the soft gamma ray regime, albeit a limited one. Silicon Pore Optics are a promising technology development that allows a break from the current trend of high-energy optics and, as such, will provide a large effective area and high angular resolution at a reduced mass. A large focal length is also shown to be advantageous, allowing a significant increase in effective area, particularly at energies of very low reflection on a multilayer coating.

3.1.5 References

- [1] Design of a soft-gamma-ray focusing telescope for the study of nuclear lines, C. M. Hubert Chen et al., SPIE Vol. 4851, 2003
- [2] W/SiC x-ray multilayers for use above 100 keV, David L. Windt et al., Applied Optics Vol. 42, no. 13, 1 May 2003
- [3] Status of X-ray Optics Development for the XEUS Mission, Marcos Bavdaz et al., 2004/SCI-A/010.
- [4] Silicon Pore Optics: Novel Lightweight High-resolution X-ray Optics Developed for XEUS, Marco Beijersbergen et al., 2004/SCI-A/011
- [5] Cosine Presentation, ESTEC 2004
- [6] Multilayer facilities required for extreme-ultraviolet lithography, D. L. Windt and W.K. Waskiewicz, j. Vac. Sci. Technol. B, 12, 3826-3832, 1994
- [7] Growth, structure and performance of depth-graded W/Si multilayers for hard X-ray optics, D. L. Windt et al., Journal of Applied Physics, 2000.

3.2 Laue Crystals

3.2.1 Laue Diffraction

Fig. 3.7 shows the path travelled by a high-energy ray traversing a crystal as it is reflected off one of the lattice planes inside a crystal, as occurs in Bragg diffraction in section 3.1.2.1. Bragg's law, equation [3.1], also governs this process.

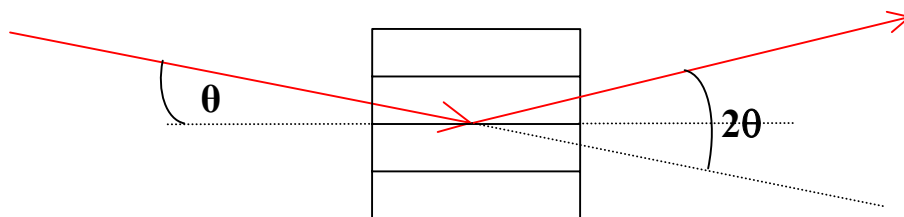


Fig. 3.7 Scattering of high-energy rays off a lattice plane inside a crystal

The ray, however, emerges from the crystal from a different face to that which it entered, and therefore shows Laue diffraction.

3.2.2 Direction of Diffraction

The two important bits of knowledge required about the Laue diffraction process are the direction and throughput of the diffracted ray (section 3.2.3). Also, a very important parameter in Laue Diffraction is crystal mosaicity (section 3.2.4).

A ray of a given energy will be reflected from the crystal planes as in Bragg diffraction, following Bragg's Law (equation 3.1). This information provides the direction of the diffracted beam. In terms of miller indices, Bragg's law becomes;

$$2 \left[\frac{a}{(h^2 + k^2 + l^2)^{1/2}} \right] \sin \theta = n\lambda \quad [3.2]$$

where h , k and l are the miller indices, defining the orientation of the crystal plane of reflection (Fig 3.8). a is the crystal lattice constant. From this, the direction (θ) can be determined for an incident ray of known energy reflecting from a known crystal plane.

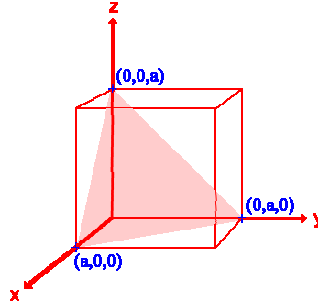


Fig3.8 Diagram showing the orientation of the (111) hkl plane within a crystal unit cell

3.2.3 Throughput of the Diffracted Ray

The throughput of the diffracted ray is very important as it allows us to calculate a value for the crystal peak efficiency through the incident-to-resultant intensity ratio. It can be shown that [1] the ratio of incident power $\{P_0(0)\}$ to diffracted power $\{P(T_0)\}$ is given by;

$$\frac{P(T_0)}{P_0(0)} = \sinh(\sigma T_0) e^{-\left(\frac{\mu}{\cos \theta_B} + \sigma\right) T_0}$$

$$\Rightarrow \frac{1}{2} (1 - e^{-2\sigma T_0}) e^{-\mu \frac{T_0}{\cos \theta_B}}$$

Typical Bragg angles are very shallow, so

$$\text{for } \theta \rightarrow 0, \cos \theta \rightarrow 1$$

$$\frac{P(T_0)}{P_0(0)} = \varepsilon = \frac{1}{2} (1 - e^{-2\sigma T_0}) e^{-\mu T_0}$$

Where;

$$\varepsilon = \text{Crystal Efficiency}$$

$$\sigma = \text{Diffraction Coefficient}$$

$$T_0 = \text{Crystal Thickness}$$

$$\mu = \text{Attenuation Coefficient for thickness } T_0$$

Using this equation, the thickness of Laue crystals can be optimised for maximum efficiency. Figure 3.9 shows a series of theoretical optimisation curves for the Ge (440) crystal plane. This plane is ~30% efficient for the positron-electron annihilation line at 511 keV.

Note that when using crystal efficiency, it is necessary to distinguish between the peak efficiency, usually expressed as a percentage, and the integrated reflectivity expressed in photons/second. Integrated reflectivity is the total diffracted flux. This value gives the number of photons reflected by the whole crystal in a given time interval. Current measurements of germanium crystals show efficiencies of ~30 % and copper ~20% for energies of 300 – 900 keV.

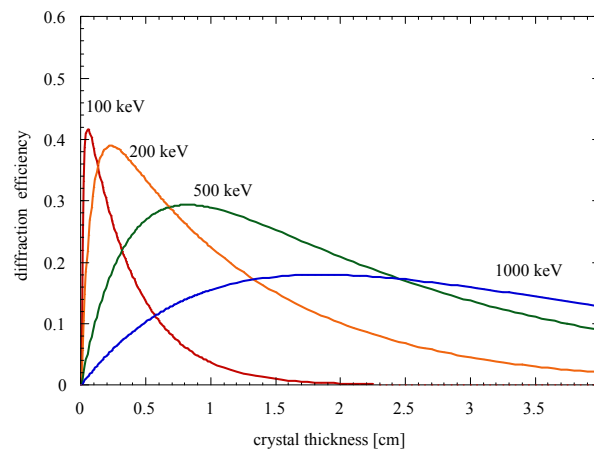


Fig. 3.9 Crystal thickness optimisation curves [4] for the (440) crystal plane of Germanium.

3.2.4 Mosaicity

A perfect crystal is one in which all of the atom basis' are placed accurately at the points of an undistorted space lattice. An x-ray beam would diffract as in figure 3.10. Up to a certain angle θ' , a few arcseconds from the Bragg angle (θ), the resultant intensity is zero. Between θ' and θ , the intensity rises sharply to total reflection, remains so over a small angular range, $\Delta\theta_0$, and then drops sharply once again to zero reflection.

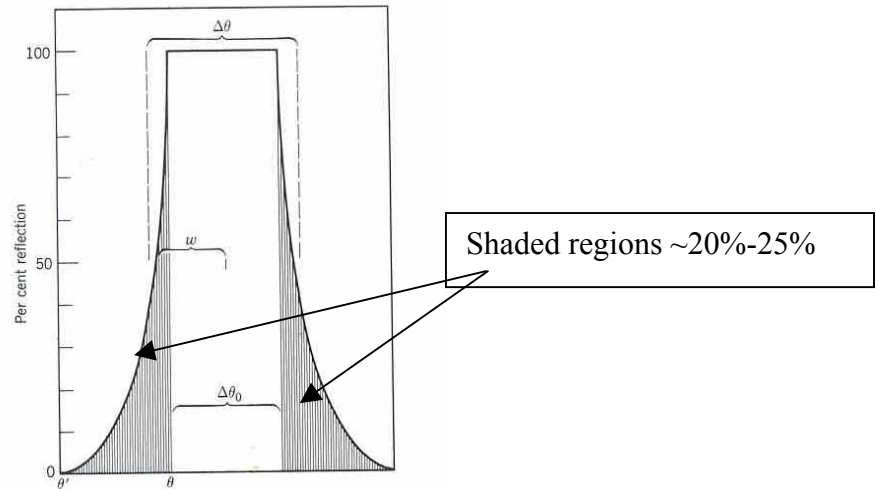


Fig 3.10 Reflection from a perfect crystal

Very few crystals, however display perfect behaviour. The measured values of $\Delta\theta$ are much larger than would be expected from perfect crystals. This led to the development of a model known as the Ideally Imperfect Crystal by Darwin. Such a crystal is constructed from many tiny crystal fragments arranged in a nearly but not quite parallel configuration. This is known as a mosaic crystal. The statistical distribution of the angles is considered to be Gaussian, where the mosaicity ($\Delta\theta_B$) is defined as the FWHM of the distribution (Fig 3.11). The result of such an arrangement is a broadening of $\Delta\theta$. Mosaicity is, in essence, a measure of imperfection in a crystal.

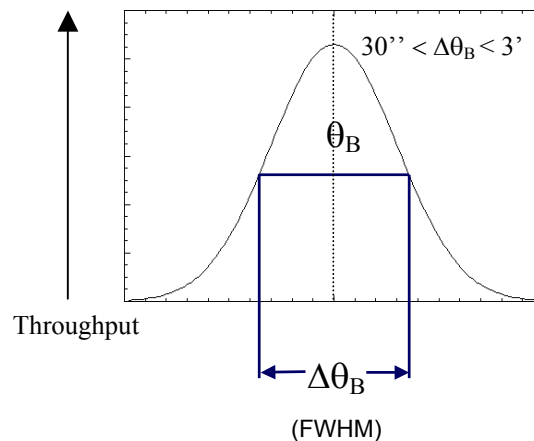


Fig 3.11 The definition of mosaicity, $\Delta\theta_B$

One important effect of increasing mosaicity is the reduction of peak efficiency. The integrated efficiency remains roughly constant. Other parameters affected by mosaicity are the field of view (FOV), energy bandwidth and angular resolution. One useful approximation is that the

mosaicity is approximately 1.5 times the field of view, and gives an indication of the extremely narrow field of view to be expected.

The energy bandwidth, corresponding to a given mosaicity, $\Delta\theta_B$, can be determined from Bragg's law (equation 3.1) as follows;

$$2d\theta_B = \frac{hc}{E} \quad \text{Bragg's law for } n = 1 \text{ and small } \theta \quad [3.3]$$

$$\frac{\Delta\theta_B}{\theta_B} = \frac{\Delta E}{E}$$

$$\therefore \Delta E = \frac{2dE^2\Delta\theta_B}{hc} \quad [3.4]$$

In this way the mosaicity of the crystal can be related to the energy bandpass.

3.2.5 Temperature Effects

The basic temperature effect on a crystal is expansion. An increase in temperature results in an increase in the lattice spacing of the crystal. The Bragg angle, as a result, is changed. Larger temperatures lead to smaller Bragg angles. These effects could become important when considering a lens made from Bragg crystals and will require further research.

The relationship between temperature and mosaicity is also yet to be determined. Extreme temperature effects, such as cryo-cooling of crystals, have been shown to increase mosaicity by increasing misalignments of mosaic domains and by further varying the unit-cell dimensions within each domain (fig. 3.10). This effect could potentially be used in the Bragg crystal manufacture where many hundreds of crystals of a certain known mosaicity are required. Again, further research into this area is required.

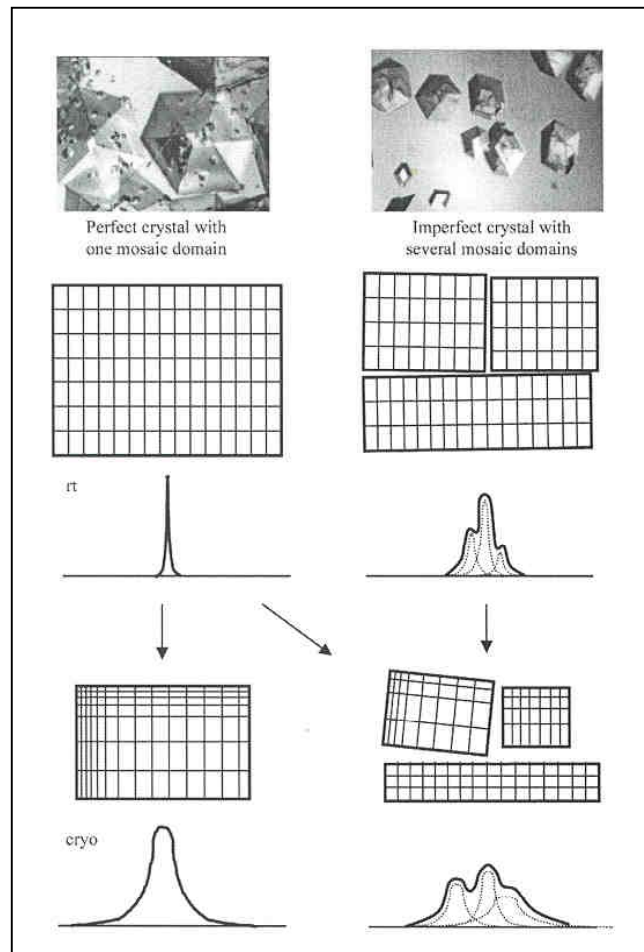


Fig 3.12 Theoretical effects of cryo-cooling on crystal mosaicity of hypothetically perfect and imperfect crystals and the application of the mosaic domain model to reflection profiles. rt = room temperature, cryo = cryo-cooled

3.2.6 Gradient Crystals

Gradient crystals have a variable plane spacing, d . Two main methods for creating a plane variation are inducing a temperature gradient across the crystal and doping a crystal with a second material with a gradient density. The application of gradient crystals to a gamma ray lens needs to be investigated further. Different potential lens configurations have been suggested using gradient crystals [6][9], including configurations capable of true imaging. One of the most useful applications of the gradient crystal is to increase the number of photons per unit bandwidth in a diffracted beam, without losing any of the overall intensity. Large magnifications and de-magnifications can be achieved by bending the gradient crystals, much in

the same way as an optical lens affects visible light. This technology has been demonstrated, though requires a great deal more investigation.

3.3 The Basic Laue Lens Principle

The Laue diffraction lens concept arises from the potential of using more than one crystal to focus high-energy rays. Fig. 3.13 shows the basic principle of this.

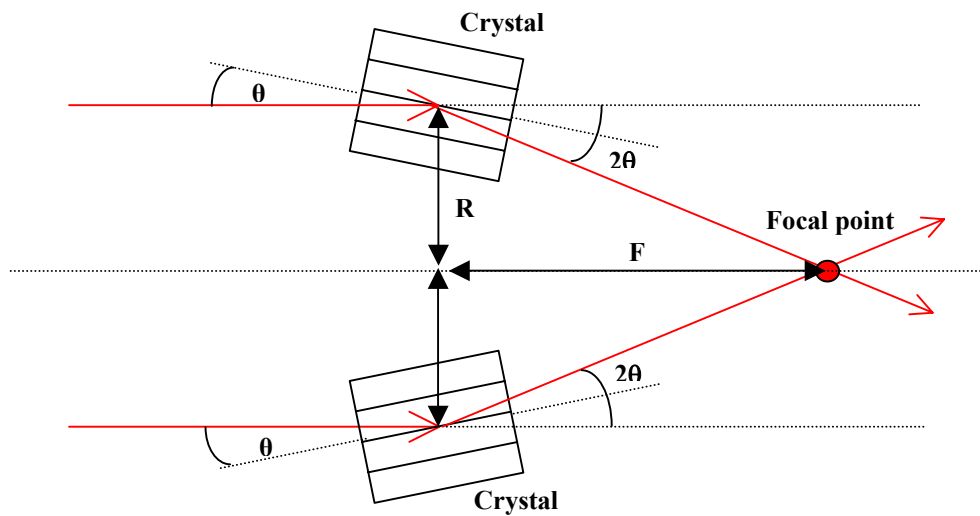


Fig. 3.13 A diagram showing a cross section of a Laue crystal optic, the ray path and focal point

A configuration of crystals in a ring with radius R , where all crystals are orientated in the same direction, θ , would focus rays of a given energy at a focal distance, F , given by;

$$F = \frac{R}{\tan(2\theta)} \quad [3.5]$$

By using the value of θ as calculated in equation (3.1), the focal length of a Laue telescope can be calculated. Combining the small angle approximation of equation 3.5 and the small angle approximation of Bragg's Law (3.3) an equation relating the lens radius and diffracted energy is obtained.

$$E = \frac{Fhc}{Rd} \quad [3.6]$$

Equation 3.6 shows that different radii of crystal rings reflecting from the same crystal plane, for example the (111) plane of Ge, will result in the diffraction of different photon energies. This allows the energy bandpass of the crystal ring to be increased through the nesting of crystal

rings. Fig 3.14 shows how nesting crystal rings results in the diffraction of photons of differing energies. Each crystal is oriented such that the incoming photons diffract from the (111) plane and, in order to meet the Bragg equation, photons of different energies are focused to the focal point depending on the radius of the crystal ring.

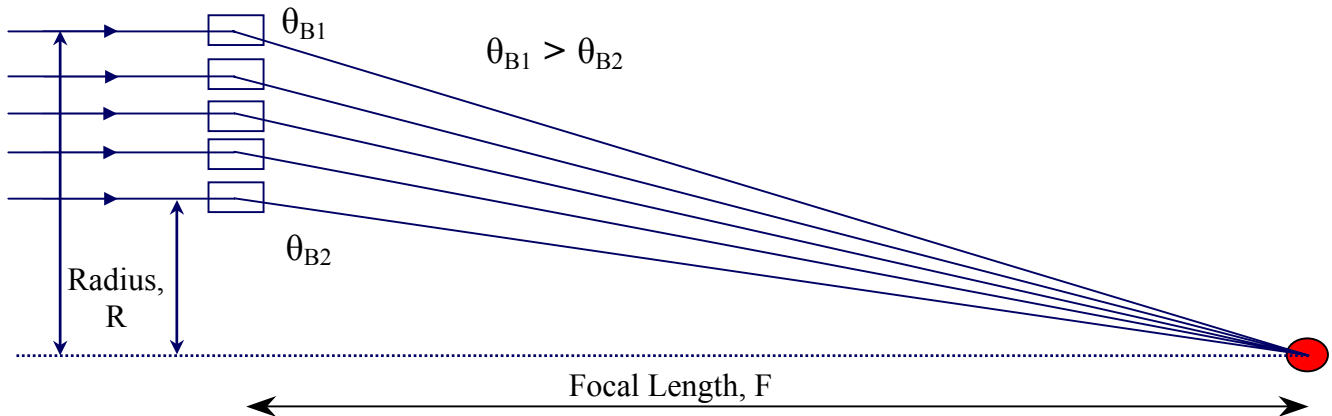


Fig. 3.14 Increasing the lens bandpass by nesting concentric crystal rings

From equation 3.2, it can be seen that changing the lattice constant, a , resulting in a different plane spacing, d , will also have an effect on the Bragg angle. Therefore, changing the type of crystal will also alter the focal length of the lens. For example, for a given energy, copper reflects with a larger Bragg angle than Germanium, thus shortening the wavelength.

The MAX mission (6.1.2), proposed by the CESR team (Toulouse, France), makes use of this effect for a portion of the optic ring structure. The 14 outer rings are Germanium, whereas the ten inner rings are of copper. Copper is a ‘better’ diffracter than Germanium due to its lattice spacing, meaning that it can be used to diffract higher energies to a shorter focal length. This allows the MAX mission to have two ‘windows’ of energy, 460 keV to 522 keV and 825 keV to 910 keV, which can be used to study lines in different regions of the energy spectrum. The choice of band gap and energy depends on the science drivers of the mission and sources of interest.

3.3.1 The Focal Spot

The point spread function (PSF) at the focal plane is due to two separate functions – the intrinsic spread due to crystal mosaicity and the misalignment error between the macroscopic crystals on the lens rings. If a physical constraint is to be placed on the alignment of crystals, it is necessary to consider how the alignment of crystals affects the point spread function size. From a geometric argument, it is shown (see Appendix 2) that;

$$r = 2F\Delta\theta \quad [3.7]$$

where r is the radius of the point spread function, F is the focal length of the lens and $\Delta\theta$ is the crystal misalignment. In order to include the mosaicity in the PSF determination, the spread of the PSF due to mosaicity can be included in the value of $\Delta\theta$ simply by taking the RMS of the two values. E.g., for a mosaicity of $30''$ and a misalignment of $15''$, $\Delta\theta = (30''^2 + 15''^2)^{1/2} = 33.5''$. Clearly, in order to reduce the PSF it is necessary to minimise the focal length, F , or reduce either crystal mosaicity and/or misalignment. As the bandwidth relies on mosaicity, however, reducing this value too far is undesirable.

3.3.2 Effective Area of the Gamma Ray Lens

In order to model the integrated effective area of the basic gamma ray lens it is necessary to sum the contribution to effective area of each crystal ring. The energy bandpass (ΔE) of each crystal ring is known from the crystal mosaicity [3.4] and the peak energy is known from the centre radius of the crystal ring [3.6]. The peak effective area can be estimated using a curve similar to fig.3.9, based on the crystal plane of interest. From the figure, the peak efficiency can be determined for a crystal ring at a given energy. As the effective area curve is assumed Gaussian, the curve can be plotted from using equation [3.8].

$$A_{\text{eff}} = \exp \left(\frac{-(E_{\text{peak}} - E_x)^2}{2 \left(\frac{\Delta E}{2.355} \right)^2} \right) \quad [3.8]$$

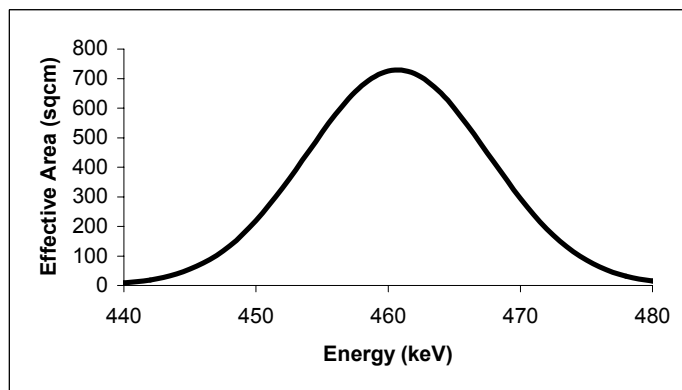


Fig 3. 15 Effective area curve of a Ge ring consisting of 2259 1cm^3 crystals and $30''$ mosaicity

Plotting a similar curve to fig.3.15 for each crystal ring in the lens, and then summing the contributions of each ring results in a total effective area curve of the lens (fig. 3.16).

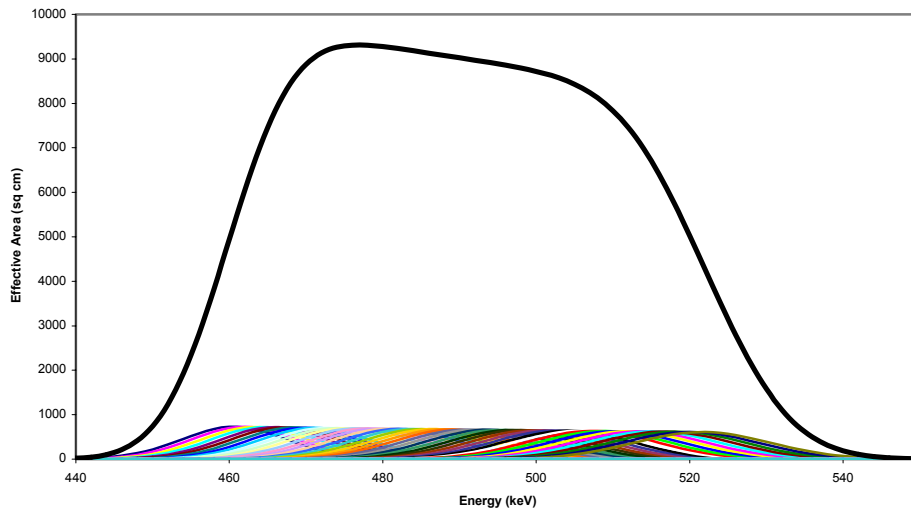


Fig 3.16 Total integrated effective area of an example 3.6m radius gamma ray lens. Focal length = 436m

Fig 3.16 shows the effective area of a lens consisting of 43 close-packed rings of Ge. Larger effective areas are achievable by increasing the radius of the lens, while keeping the energy range constant. A larger geometric area and, hence, a greater effective area results. The energy range can also be extended further by increasing the number of crystal rings. A spreadsheet model has been constructed that allows various lens configurations to be investigated.

An important consideration when designing a crystal lens is the mass of the optic. Crystalline germanium and copper are dense materials meaning a lens such as that graphed in 3.16 would have a mass of ~1000 kg. It is possible to reduce the mass of the ring at the cost of crystal efficiency, by making the crystals thinner, or at the cost of reducing effective area by varying the nesting frequency of the rings (fig 3.17). Increasing the spacing between crystal rings, for example, would allow you to design the effective area profile to suit the science observation requirements (fig 3.18)

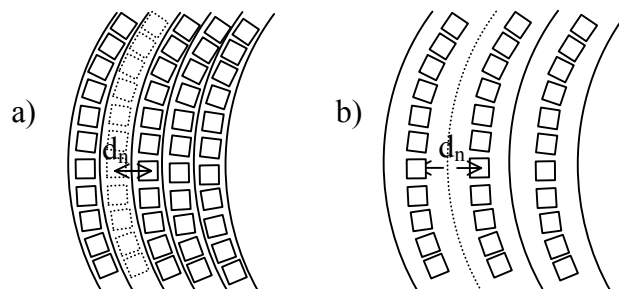


Fig. 3.17 a) A high nesting frequency lens has a large number of rings per radius length, whereas b) a low nesting frequency lens has a lesser number of rings. Low frequency results in a less dense lens and, hence, has a lower mass at the cost of effective area of the lens.

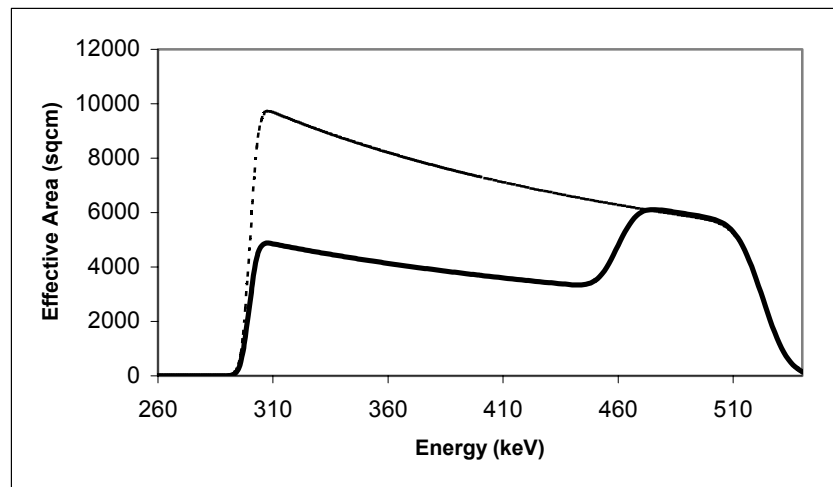


Fig 3.18 A large lens configuration, 4.5m maximum radius. The dashed line shows a fully nested lens whereas the solid line shows a lens optimised for the 460-520 keV region with an extended band for lower energies, taking potential redshifted sources into account

Using the equations in section 3.2, spreadsheet models have been constructed that allow various potential lens configurations to be explored. The parameters that can be changed and investigated in the models are

- Lens Radius
- Crystal Type (Cubic structures only)
- Focal Length
- (hkl) numbers and crystal planes
- Mosaicity
- Focal spot size
- Crystal Efficiency

From these parameters, effective area curves can be obtained. In order to verify the models, the effective area curves of MAX, as reported in the MAX literature, were reproduced (6.1.2).

3.3.3 Lens Size and Deployable Optics

Compare the fairing diameter of standard launchers to the diameter of the lenses mentioned in this section and you will notice that the lens is too large to fit. For example, Europe's largest launcher, the Ariane 5, has a maximum internal fairing diameter of ~4.5m compared to the large lens from fig 3.18 with a diameter of 9m. This suggests that a deployable mechanism is required.

A possible mechanism is shown in fig. 3.19. The lens will be split into segments and stacked in a ‘concertina’ configuration. This will allow the lens to be packed into the volume of the launcher fairing. Once in orbit, the lens will deploy and lock in the large diameter ring required.

Other mechanisms are also possible and a tradeoff study is required. It is important that the alignment between crystals is maintained, meaning the error that can be tolerated in deployment is likely to be extremely small ($< 30''$) – see appendix C. The reliability of such a mechanism is crucial.

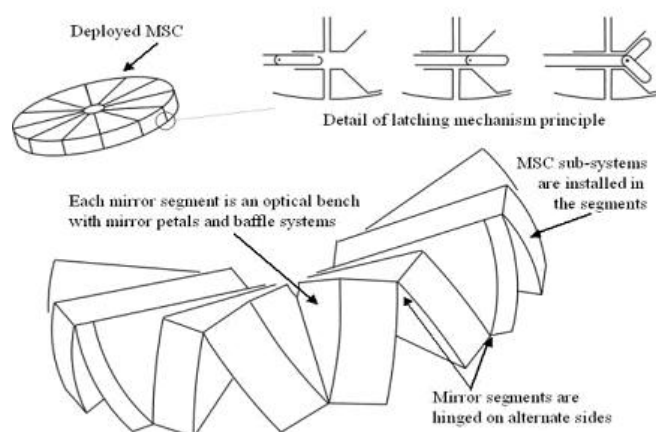


Fig. 3.19 Possible deployable optic configuration for a gamma-ray lens

3.3.4 References

- [1] Hubert Halloin, Claire: Premières Lumières d’une Lentille Gamma. PhD Thesis, University Paul Sabatier, Toulouse, 2003
- [2] Charles Kittel, Introduction to Solid State Physics, John Wiley & Sons, 6th Edition, 1986
- [3] Eduard Preuss et al., Laue Atlas, Halsted Press, John Wiley & Sons, 1974
- [4] Peter von Ballmoos, MAX Presentation, ESTEC, January 2004
- [5] Craig Brown, Gamma Ray Lens presentation, ESTEC, September 2004
- [6] Robert K. Smither, Crystal Diffraction Lenses for Imaging Gamma-Ray Telescope, World Scientific, 1986
- [7] Peter von Ballmoos, MAX – A Gamma-ray Lens for Nuclear Astrophysics, 2003
- [8] H. Klug, X-Ray Diffraction Procedures, John Wiley & Sons, 1954
- [9] G.K Skinner and P. B Fernandez, Variable-Metric diffraction crystals for X-Ray Optics, Rev. Sci. Instrum. 63 (2), February 1992

4. Focal Plane Instrumentation and Technologies

The Gamma Ray Lens mission requires a detector capable of working with photons of energies of 300 to 900 keV. This section considers the possible detectors capable of meeting the scientific requirements in this energy regime. A polarimetry instrument is also considered, as well as the potential of using an advanced Compton telescope at the focal plane.

4.1 Gamma-Ray Interaction with Matter

There are three methods by which X-rays and Gamma rays interact with matter [1]; photoelectric absorption, Compton scattering and pair production. This section looks at each of these mechanisms.

4.1.1 Photoelectric Absorption

The process of photoelectric absorption is where an incident photon is completely absorbed by an atom in an absorbing material. As a result of this absorption, an electron is ejected from the atom's nucleus, as shown in figure 4.1. This photoelectron, in order to conserve energy and momentum, must have been bound to the atom, i.e. an inner electron of the atom.

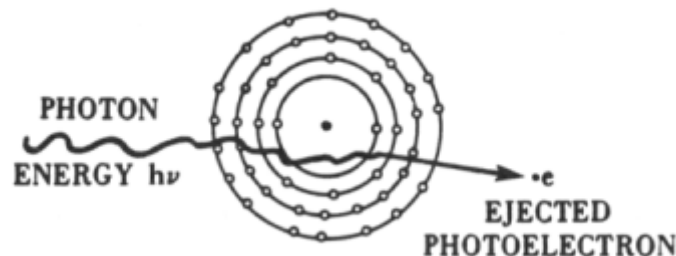


Figure 4.1 The photoelectric absorption process

The kinetic energy, T_e of the photoelectron is given by

$$T_e = E_\gamma - B_e \quad [4.1]$$

where B_e is the binding energy of the electron and E_γ is the energy of the incident gamma ray. The vacancy left by the ejected electron is subsequently filled by a higher-shell electron, the transition resulting in an X-ray being emitted.

This process is the most favoured type of interaction for gamma ray spectroscopy, since all of the gamma ray energy is deposited into the detector. It is, however, only dominant at very soft gamma ray energies, <200 keV. The interaction is also reliant upon Z (atomic number), where the absorption probability, τ , is given by

$$\tau \propto \frac{Z^n}{E_\gamma^{3.5}} \quad [4.2]$$

In [4.2] n is usually between 4 and 5 depending on the absorber. This dependence on Z has large implications in the choice of absorber material for both detectors and shielding purposes.

4.1.2 Compton Scattering

Compton scattering is the process where a gamma ray incident on an absorbing material is scattered by an outer electron of an atom, where some of the gamma ray energy is imparted to the electron. Note that not all of the photon energy can be passed on to the electron as momentum and energy are to be conserved. Fig 4.2 shows a schematic of Compton scattering from an outer shell electron.

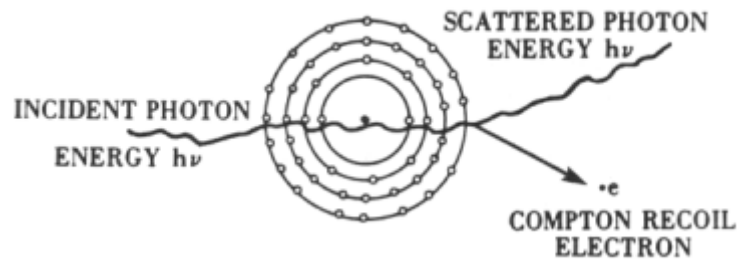


Fig. 4.2 The Compton scattering process

Conservation of energy and momentum lead to this expression for the energy of scattered photon:

$$E'_\gamma = \frac{E_\gamma}{1 + (E_\gamma/m_0c^2)(1 - \cos \theta)} \quad [4.3]$$

where θ is the scattering angle, m_0c^2 is the electron rest mass energy and E_γ and E'_γ are the incident and scattered gamma ray energies respectively. Equation [4.4] gives the kinetic energy of the scattered electron after the collision has occurred.

$$T_e = E_\gamma - E'_\gamma = \frac{E_\gamma^2(1 - \cos \theta)}{m_0c^2 + E_\gamma(1 - \cos \theta)} \quad [4.4]$$

From [4.4] it is evident that a range of kinetic energies are possible, from zero at $\theta = 0^\circ$ to $2E_\gamma^2/(m_0c^2 + 2E_\gamma)$ for $\theta = 180^\circ$. The scattered photon continues through the absorber, interacting further or escaping the absorber material completely. A photon escaping is an important event in gamma ray spectroscopy as not all of the gamma ray energy is deposited within the detector. This results in a continuous background in the energy spectrum known as the Compton continuum, which extends up to an energy corresponding to the maximum energy transfer. At this energy, a sharp cut off is evident in the energy spectrum, known as the Compton edge.

Compton Scattering is the most likely form of interaction in the intermediate gamma ray energy range, between 200 keV and 5 MeV. As the probability of Compton scattering is related to the number of electrons available to cause a scatter, the probability of this mechanism also increases with larger Z .

4.1.3 Pair Production

For gamma rays with energy greater than or equal to 1.022 MeV, twice the rest mass of an electron, in the presence of an atomic nucleus, the possibility of pair production is introduced. This mechanism results in an electron-positron pair being created from the high-energy gamma ray, with the excess energy being evenly divided between the resultant electron and positron as kinetic energy. Figure 4.3 shows a schematic of the pair production process.

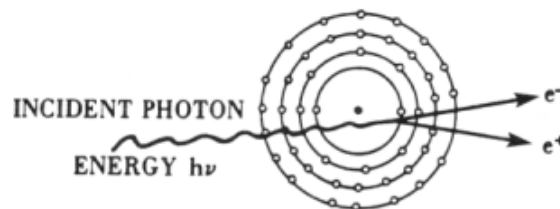


Fig 4.3 The pair production process

As the surrounding medium slows the resultant positron to thermal energies, the positron can annihilate with one of the atomic electrons resulting in two 511 keV gamma rays being emitted. Either these are then absorbed in the medium through one of the aforementioned mechanisms, or one or both photons escape the detector.

Photons that escape the detector result in 'escape peaks' in the gamma ray spectra. One 511 keV photon escaping results in a peak at $E_\gamma - m_0c^2$ (the single escape peak) and both 511 keV photons escaping results in a peak observed at $E_\gamma - 2m_0c^2$ (the double escape peak). Pair production only becomes important at energies in excess of 5 MeV, however, as Compton scattering remains the dominant mechanism at energies just exceeding 1.022 MeV.

4.2 High Energy Photon Detectors

It is noted in section 4.1 that materials with high Z are most suited for the absorption of gamma rays and, as such, high energy photon detectors use such materials. There are two main detector types that will be considered in this section; Germanium detectors and scintillator materials.

4.2.1 Germanium Detectors

Germanium (Ge) detectors are a favourite choice of detector for spectroscopy missions requiring excellent energy resolution [1][2]. The Ge detector, like other semiconductor detectors, is a large reverse-biased p-n junction diode. At the junction between the p and n type materials, the migration of electrons and holes results in a region of net zero charge, known also as the depletion region. The net positive and negative charges on opposite sides of the junction result in an electric field gradient across the depletion region.

When a gamma ray interacts with the germanium (see section 4.1) an electron-hole pair is produced in the depletion region. The pair will then be accelerated to the edges of the detector, resulting in an electrical current. This measured current is proportional to the energy of the interacting gamma ray, and can therefore be determined.

It is necessary to maximise the size of the depletion region in the Ge since this is the active part of the detector material. This volume can be increased by the application of a reverse-bias, where the width of the depletion region is expressed by:

$$W_d \propto \left(\frac{V}{N} \right)^{\frac{1}{2}} \quad [4.5]$$

Here, V = the bias voltage applied and N = the impurity concentration in the material. Natural purity Ge only maintains a depletion region of a few millimetres. The only way to increase the width of the depletion region is, therefore, to increase the purity of the material.

Extremely pure Ge is now available due to advances in manufacturing techniques. Such high-purity Germanium has an impurity concentration of approximately 1 part in 10^{12} , resulting in a depletion depth of several centimetres. It can also be stored at room temperatures, unlike other doped Ge materials e.g. Ge(Li) that require deeply cooled storage (77 K) in order to prevent diffusion of the doping substance.

The shape of the Ge crystal also has an effect on the depletion region volume. A cup-shaped crystal results in the electric field being more uniform, extending the active volume.

The energy required to make an electron-hole pair in Ge is $\sim 3\text{eV}$. Gamma rays, with energies of a few hundred keV thus result in many of these pairs being produced, leading to good resolution

and low statistical fluctuations. It is also necessary to cool the detector to 70- 85 K in order to reduce electron noise due to electrons being thermally excited across the very small (0.67 eV) band gap at room temperature. Note that the germanium is both the absorbing medium and the detector from which the energy of the gamma ray can be established.

Table 4.1 shows some positive and negative aspects of germanium detectors.

Advantages of Ge Detectors	Disadvantages of Ge Detectors
Excellent energy resolution (0.2 % at 662 keV)	Cryogenics
Good history of use in space applications	Thermal cycling
	Radiation hardness – Annealing required
	Limited volume

Table 4.1 A summary of advantages and disadvantages of using a Ge detector for gamma rays

4.2.2 Scintillator Detectors

Some of the most recent developments in high-energy detectors are in the genre of scintillator detectors. Certain inorganic scintillators have been shown to display very competitive energy resolutions, as well as having further advantageous properties over semiconductor detectors. The following is a list of desirable characteristics seen in the best organic scintillators.

- High light output (photons/MeV)
- Fast scintillation speed (ns)
- Good energy resolution (% , R_{FWHM})
- High density (ρ , gcm^{-3})
- Large crystal size ($10\text{-}100\text{ cm}^3$)
- Low cost per cm^3
- Low afterglow
- Low background count rate

Scintillators usually constitute a host material, e.g NaI, and is then doped with an impurity e.g Tl. Light production within a scintillator material results from a complex sequence of excitation and de-excitation processes. The impurity in the material is chosen to produce a luminescent centre energetically intermediate between the valence and conduction bands of the host material.

When a gamma ray interacts within the crystal through one of the above processes (section 4.1), the resultant electrons in turn produce electron – hole pairs. These diffuse to the neighbourhood of the luminescent centres and form excited states that decay with visible emission.

Photomultiplier tubes (PMT) with a typical gain of $\sim 10^6$, and an output pulse that is ideally proportional to the incident gamma ray energy, is used. The energy of the gamma ray can then be determined from the resultant electric current produced by the PMT.

Inorganic scintillators tend to be very radiation hard and require no active cooling – both very advantageous characteristics for many space applications.

This section will consider four scintillator detectors of interest to the Gamma Ray Lens [3][4].

4.2.2.1 BGO

BGO, or Bizmuth Germanate ($\text{Bi}_4\text{Ge}_3\text{O}_{12}$), is a popular, commercial scintillator detector used for many applications, from medical diagnostics to high-energy astrophysics. BGO is a very dense scintillating material and, as such, has a very high stopping power. Its commercial availability, as well as the ability to make it in large quantities, makes this the scintillator of choice when large quantities of scintillating material are required. For example, BGO was used aboard INTEGRAL in the SPI instrument for the anticoincidence shielding.

The main drawbacks of BGO as a detector are the low light yield of the material, the slow response time, poor energy resolution ($\sim 15\%$ @ 662 keV) and the fact that BGO can activate when irradiated, causing secondary events in the detector and increasing noise. See table 4.2 for a summary of important scintillator properties.

4.2.2.2 LYSO

LYSO is the commercial name for Cerium doped Lutetium Yttrium Orthosilicate ($\text{Lu}_{2(1-x)}\text{Y}_{2x}\text{SiO}_5:\text{Ce}$). It has recently become commercially available and is now being used extensively in the US for medical applications. LYSO has a similar density and stopping power to BGO, yet shows a marked improvement in energy resolution ($\sim 10\%$ @ 662 keV), light yield and response time. LYSO has more than seven times the light output than BGO and a decay time that is approximately seven times faster, too. It also has the benefit of having a scintillation emission compatible with most photo multiplier tubes (PMTs), at 420 nm. See table 4.2 for a summary of important scintillator properties.

4.2.2.3 LuAP

Lutetium Aluminium Perovskite, or LuAP, is another scintillator currently under development. Again, LuAP offers a further improvement in energy resolution, being approximately 7-9% at 662 keV. The light yield of LuAP is about half that of LYSO, yet is still a large improvement on BGO. The major advantage of LuAP over other organic scintillators is its extremely fast decay time; 17 ns compared with 300 ns for BGO and 40 ns for LYSO.

Currently, LuAP is not commercially available and is difficult to make due to its brittle nature. Large crystals have been made, however, the largest by a Scottish company called Photonic Materials (fig. 4.4). Activation within the crystal could still pose a problem, increasing the background noise in the detector. See table 4.2 for a summary of important scintillator properties.



Fig. 4.4 Photograph showing the largest LuAP crystal reported to date

4.2.2.4 Halide Scintillators

Halide scintillators have been used since the very early days of x-ray and gamma ray astronomy with the introduction of the alkali halide scintillators in the 1960s. NaI and CsI were generally replaced by semiconductor detectors due to the pursuit of very high-energy resolution, semiconductors being at the forefront of research in detector physics today for this reason. Recent developments in halide scintillator detectors, however, have re-introduced these materials to space applications and, with significant development, could potentially be used in high-energy astrophysics missions.

Ce^{3+} doped Lanthium Chloride ($\text{LaCl}:\text{Ce}$) and lanthium bromide ($\text{LaBr}:\text{Ce}$) are two such advanced halide scintillators. The energy resolutions of $\text{LaCl}:\text{Ce}$ and $\text{LaBr}:\text{Ce}$ are extremely promising, being [5] 3.3 and 2.8 % at 662 keV respectively. Such resolutions are competitive with some semi-conductor detectors such as Cadmium Telluride, CdTe, (~5% at 662 keV). One major advantage of inorganic scintillators is the radiation hardness of the material. A huge drawback of semiconductor materials is the damage incurred by radiation. Ge detectors, for example, can accept ~ 1krad of radiation and CdTe ~ 10 krad compared to 1 Mrad for $\text{LaBr}:\text{Ce}$. Clearly, for longer duration missions or for missions in harsh radiation environments, organic scintillators have a large advantage. See table 4.2 for a summary of important scintillator properties.

Currently, both $\text{LaBr}:\text{Ce}$ and $\text{LaCl}:\text{Ce}$ are in the developmental stage and are not widely commercially available. $\text{LaCl}:\text{Ce}$ is in a more advanced stage of development, with methods of

improving the manufacture of LaBr:Ce to commercial standards being investigated. The largest LaCl:Ce and LaBr:Ce crystals to date are 350 cm³ and 2.3 cm³ respectively.

Other scintillator materials have even greater potential for improving energy resolution. Two such examples are Lanthium Iodide (LaI:Ce) and Lutetium Iodide (LuI:Ce). Theoretically, both material types should provide an energy resolution to rival the majority of new compound semiconductors, while having all of the advantages of organic scintillators (Radiation hardness, no active cooling). Very little development has been focused on these materials to date, and preliminary investigations have shown problems with getting the detectors to perform well. Resolutions of ~1% should eventually be achievable with these detectors, possibly better (the theoretical best resolution for LuI:Ce is ~0.6 % at 662 keV), if considerable development activities are pursued.

Material	Density [g/cm ³]	Emission Maximum [nm]	Decay Constant	Refractive Index	Light Yield [ph/MeV]	Resolution @ 662 keV
BGO	7.13	480	300 ns	2.16	8000	15%
CsI(Tl)	4.51	550	0.6/3.4 µs	1.79	65000	8%
NaI(Tl)	3.67	415	230 ns	1.85	43000	6%
LYSO	7.1	435	48 ns	1.81	32000	6%
LuAP	8.4	365	17 ns	1.94	17000	8%
LaCl:Ce	3.79	350	28 ns	1.9	49000	3.3%
LaBr:Ce	5.3	420	18 ns	-	61000	2%
LuI:Ce	5.6	474	23 ns	-	50000	1%*

* Not measured

Table 4.2 Summary of important scintillator properties for various inorganic scintillators

4.2.3 Compton Detectors

The MAX mission (section 6.1.2) is expected to improve background rejection using a Compton Detector. The principle behind a Compton telescope is as follows. An incident gamma ray of energy E_γ is identified by two successive interactions in two detector layers, D_1 and D_2 . The interaction of the gamma ray with D_1 results in a Compton scatter of the gamma ray, transferring energy E_1 to an electron in the detector material that in turn scatters at an angle ϕ . The scattered photon then is detected in the second detector, D_2 , and loses its remaining energy, E_2 . Equation [4.6] allows the estimation of the scattered angle, ϕ , as a function of the two measured energies, E_1 and E_2 .

$$\cos \phi = 1 - \frac{m_e c^2}{E_2} + \frac{m_e c^2}{E_1 + E_2} \quad [4.6]$$

As both interaction locations are known, the incident gamma ray is also known to lie on the surface of a cone with half angle φ around a direction (χ, ψ) of the scattered ray.

P. Jean et al [6] conducted an estimation of the background counts for three different types of gamma-ray observatories; a coded aperture mask, a Compton telescope and a Laue diffraction lens using a 3x3 pixel Ge detector. In order to conduct the comparison, the simulations assumed an effective area of 500 cm² and an integration time of 10⁶ seconds of each telescope type. Figure 4.5 shows the result of these simulations.

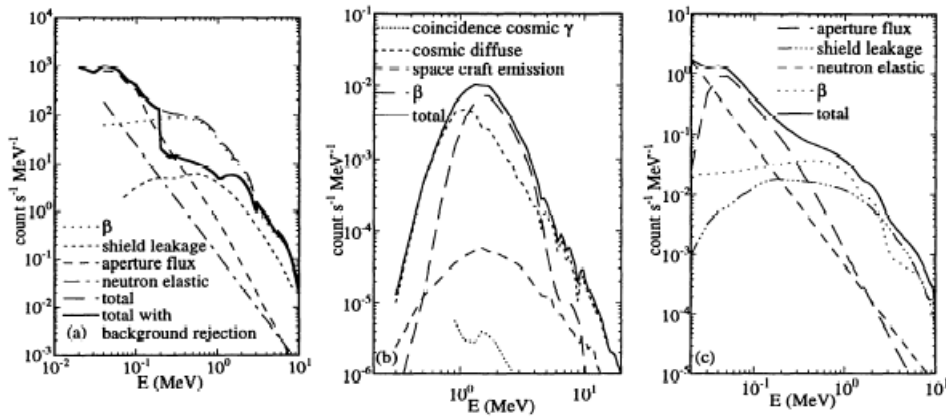


Fig. 4.5 Estimated total background for a) a coded mask telescope, b) a Compton telescope and c) a diffraction lens telescope [6]

It can be seen from Fig. 4.5 that the Compton telescope provides the best background rejection capability of the three detector types investigated. One of the ideas in the MAX proposal is to use this type of detector to further decrease the background contribution, while still employing a Laue focusing optic. Fig. 4.6 shows the expected gain in sensitivity using the TGRS Ge detector, and scaled for background reduction using Compton kinematics.

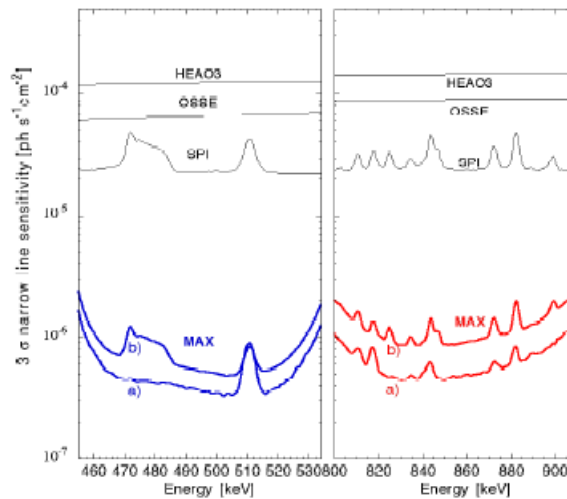


Fig 4.6 3 σ line sensitivity of MAX compared with other earlier missions. MAX performance is based on a) the background of the TGRS Ge detector, scaled using Compton kinematics for background rejection and b) on the measured background of the SPI/INTEGRAL Ge detectors

The possibility of using Compton background rejection techniques for the Gamma Ray Lens needs serious further consideration.

4.2.4 Polarisation Detectors

Another brief statement made in the MAX literature [7] introduces the idea of using a strip Ge detector, Si/CdTe matrix, or single segmented Ge detector to perform high level spectroscopy, which is also capable of measuring the polarisation of the incident photons. As noted in section 2.1.6, there appears to be a science case for the incorporation of a polarimeter in the GRL.

There are many published papers on the prospect of detectors capable of performing both polarimetry and spectroscopy simultaneously [8] [9] [10].

An IASF/CNR group led by E.Caroli reports to have developed a detector capable of performing good polarisation measurements for the CACT μ S balloon experiment and the CIPHER coded mask telescope. [11]. It is suggested that a pixellated CdTe/CZT or Ge detector, acting as both scatterer and a detector, dramatically increasing the efficient area and therefore sensitivity with regards to polarimetry, will be suitable to conduct polarisation measurements while also simultaneously conducting spectroscopy. It is expected that from a 300cm² detection area and 20hr exposure we can expect a minimal detectable polarisation level of $\sim 0.2\%$ for 100 mCrab flux. The GRL is likely to experience much smaller fluxes than this, although exposure times are also likely to be longer. Fig 4.7 shows the detector for the CIPHER CdTe position sensitive spectrometer for gamma ray polarimetry. Such a detector is capable of providing $\sim 2\%$ energy resolution at 511 keV.

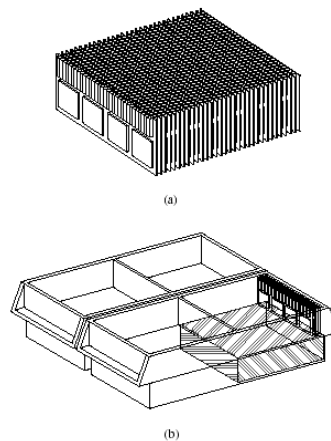


Fig. 4.7 a) One of the four CIPHER PSD basic modules, b) possible mechanical structure for the four module PSD.

The potential of incorporating a geometry capable of polarisation measurements in the GRL mission is of interest and should be investigated further.

4.3 The Miniature 50-80 K Pulse Tube Cooler

Germanium detectors provide excellent energy resolution, although one major drawback of Ge detectors is the requirement for active cooling – something which, in previous missions, has resulted in a great mass and power requirement increases of the payload. New developments, however, have been made in active cooling systems. This section introduces one such technology that has potential applications for the GRL.

The Miniature 50-80 K Pulse Tube Cooler (MPTC) has been developed by Air Liquide and offers a major mass and power saving on previous cryogenic systems. Fig. 4.8 shows a photograph of the MPTC.

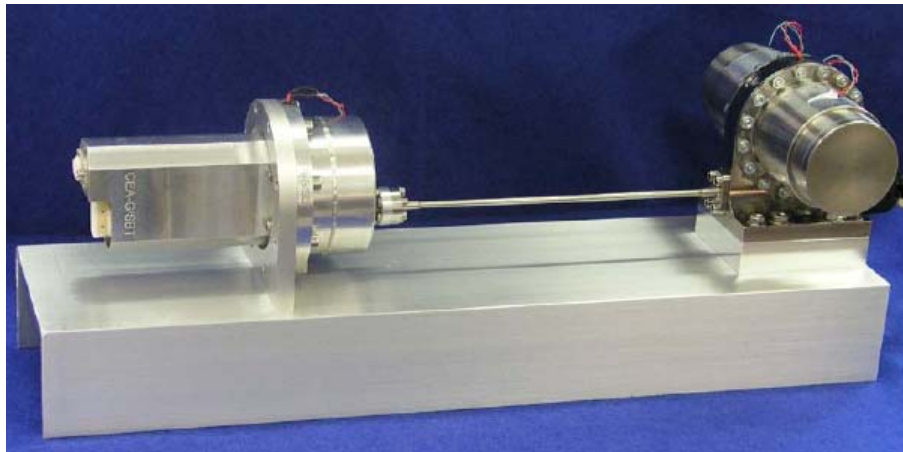


Fig. 4.8 The Miniature 50-80 K Pulse Tube Cooler, as developed by Air Liquide, France

The total mass of the MPTC is 2.8 kg and has an operating power requirement of 35.3 W. The length of the MPTC is 0.48m, including the 0.2m connecting tube. Vacuum thermal tests have been performed on the cooler, including load lines and parasitic heat losses for various thermal environments, input powers and orientations. The MPTC has also undergone extensive mechanical and vibration testing.

The specifications of this cooler are ideal for the active cooling of a space-borne germanium detector, the low power consumption and mass of the MPTC being significantly smaller than previously flown cryogenic systems [12].

4.4 References

- [1] <http://www.phys.jyu.fi/research/gamma/publications/akthesis/node1.html> (February 2005)
- [2] X-ray detectors in astronomy, G. W Fraser, Cambridge Astrophysics Series, 1989
- [3] Scintillators, A. Owens, ESA Presentation, Payloads and Advanced Concepts Office, 2004
- [4] <http://www.photonicmaterials.com> (February/March 2005)
- [5] Hallide Scintillators (Thesis), E. van Loef, Delft University Press, 2003
- [6] Instrument Concepts for high resolution Gamma-ray spectroscopy, P. Jean et al, Astron. Astrophys. Suppl. Ser. 120, 673-676 (1996)
- [7] The MAX mission: focusing on high sensitivity gamma-ray spectroscopy, P. von Ballmoos et al, Proceedings of the 5th INTEGRAL Workshop, Munich 16-20 February 2004, ESA SP-552
- [8] CACT μ S: A small CdTe array for a prototype balloon experiment, E. Caroli et al., Nuclear Instruments and Methods in Physics Research A 513 (2003) 357-361
- [9] PoGO: The polarised gamma-ray observer, S. Larsson and M. Pearce, Nuclear Instruments and Methods in Physics A, 2004
- [10] Measuring polarisation of high-energy gamma rays, G. Barbiellini et al., Nuclear Instruments and Methods in Physics A 518 (2004) 195-197
- [11] A CdTe position sensitive spectrometer for hard X-ray and soft Gamma-ray polarimetry, E. Caroli et al, Nuclear Instruments and Methods in Physics Research A 477 (2002) 567-573
- [12] Miniature 50 to 80 K Pulse Tube Cooler Development and Performance Testing, Air Liquide, ESA/ESTEC contract No. 14896/00/NL/PA, Document Ref: DTA/DTED/TT/TT/03.1066, Feb 2004

5. Sensitivity Analysis

It is important to note that the key figure of merit for the Gamma Ray Lens is sensitivity. Sources in the soft gamma ray regime, for example, supernovae type Ia, tend to have fluxes of $\sim 10^{-6}$ photons $\text{cm}^{-2}\text{s}^{-1}$. Assuming a total observation time of 10^6 seconds and time bins of 100 ks required to observe the time evolution of the spectral line, the required effective area of the optic can be calculated if it is also assumed that ~ 1000 photons per time bin are required to perform modest line spectroscopy. An effective area of $\sim 1\text{m}^2$ is needed to achieve 1000 photons per time bin [1]. The sensitivity achieved by a given mission configuration will be established and used to assess scientific performance.

A model has been developed in order to evaluate the line sensitivity of a Laue diffraction telescope as a function of geometry, material properties, background and so on. The main principles of the model are described in this section.

5.1 Input to the model

Input parameters and geometries to be used by the GRL sensitivity model are read from an input file. Table 5.1 lists the key parameters used by the model with example values and units. Table 5.2 gives an example of a geometry used to test the simulation – the MAX mission parameters (section 6.1.2). A given model run may include a single geometry or many (when assessing sensitivity as a function of focal length and optics radius).

Parameter	Value (example)	Units
crystal mosaicity	30.	[arcseconds FWHM]
peak efficiency (Ge)	0.33	[$\times 1$]
peak efficiency (Cu)	0.22	[$\times 1$]
fill factor	0.85	[$\times 1$]
co-alignment	30.	[arcseconds FWHM]
detector thickness	3.	[cm]
PSF radius to include	1.	[\times sigma]
energy resolution (intrinsic)	0.4	[% FWHM]
line width to include	1.	[\times sigma]
detection significance	3.	[\times sigma]
integration time	1.e6	[s]
Ge lattice constant	5.66e-10	[m]
Cu lattice constant	3.62e-10	[m]
ring width	1.	[cm]
file containing background	SPI_background.dat	

Table 5.1 GRL model input parameters

f [m]	Ge_in [cm]	Ge_out [cm]	Cu_in [cm]	Cu_out [cm]
133	97	110	87	96

Table 5.2 MAX geometry simulated in order to test the sensitivity model

5.2 Model Description

Having read in the input parameters, the model steps through the geometries to be simulated. For each geometry, it first steps through the individual Ge and Cu crystal rings from inside to outside, calculating the contribution to the effective area as follows...

1. Calculate the Bragg energy [keV] to which the ring is tuned according to the equation

$$E_B = \frac{1}{1000q} \frac{hc}{2d \sin\left(\frac{r}{2f}\right)} \quad [5.1]$$

where d is the atomic plane spacing [m], r is the ring radius and f is the telescope focal length (r and f in the same units).

2. Calculate the standard deviation of the energy distribution [keV]

$$\sigma_E = 1000q \frac{2d}{hc} E_B^2 \sigma_\theta \quad [5.2]$$

where σ_θ is the standard deviation of the angular distribution of the crystal planes (derived from the mosaicity). Note that this value is optimistic as it does not include factors such as warping or misalignment due to the deployment mechanism.

3. Calculate the geometrical area of the ring $A_g = 2\pi r dr$
4. Define the contribution of this crystal ring to the effective area as a Gaussian distribution

$$A_e(E) = A_g p f \exp\left(-\frac{(E - E_B)^2}{2\sigma_E^2}\right) \quad [5.3]$$

where p is the peak Laue diffraction efficiency of the crystals and f is the fill factor. This cycle of steps is repeated to add the contribution of all Ge and Cu crystal rings to $A_e(E)$, giving the total effective area of the GRL as a function of energy. This is then used to calculate the line sensitivity as follows. The 1σ radius of the PSF on the focal plane [cm] is calculated

$$\sigma_{\text{PSF}} = 100f \sqrt{\sigma_m^2 + \sigma_{\text{CA}}^2} \quad [5.4]$$

where σ_{ca} describes the angular distribution of the crystal co-alignment in radians. σ_{PSF} and the detector thickness d , give the detection volume in the focal plane for any number (n) of 1σ PSF radii.

$$V = \pi(n\sigma_{\text{PSF}})^2 d \quad [5.5]$$

and the line sensitivity as a function of energy is then given simply by,

$$\text{line sensitivity (E)} = \frac{n}{Q(E)A_E(E)} \sqrt{\frac{B(E)V\Delta E}{t}} \text{ photons cm}^{-2}\text{s}^{-1} \quad [5.6]$$

where n is the required detection significance (i.e. $n=3$ for a 3σ detection), $Q(E)$ is the detector quantum efficiency as a function of energy and t is the integration time. ΔE is the energy width to be included which is determined by the detector energy resolution or the intrinsic width of the astrophysical line, whichever is broader. $B(E)$ is the background in the detectors per unit volume as a function of energy. For this work a real background spectrum has been adopted from the Germanium detectors in the INTEGRAL SPI instrument. SPI uses anti-coincidence shields for background rejection and by adopting the SPI background (fig. 5.1), we implicitly assume that we will achieve a similar degree of background rejection.

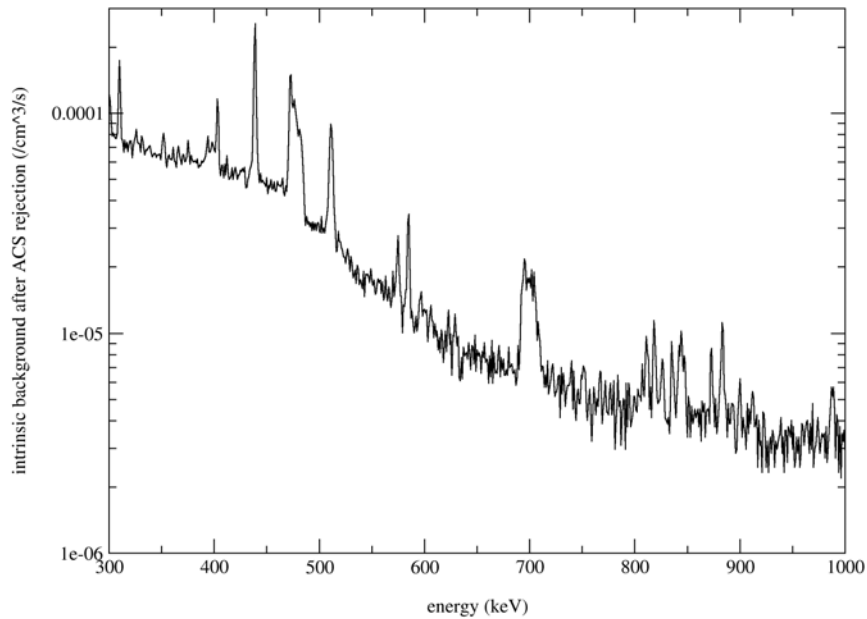


Fig. 5.1 SPI intrinsic background after background rejection

5.3 Model output

The sensitivity model generates the following output files:

QE.out is the detector quantum efficiency as a function of energy, calculated from the linear attenuation coefficients of Ge and the specified detector thickness (figure 5.2).

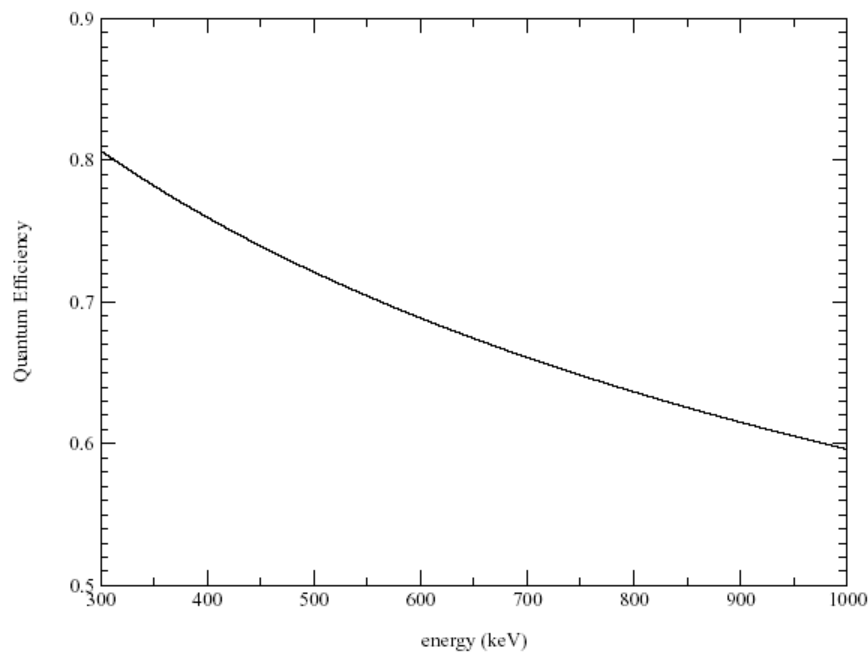


Figure 5.2 Quantum Efficiency of 3cm thick Ge detectors as a function of energy

background.out is the background per unit volume in the detectors as a function of energy. This is generated by extracting the background from an INTEGRAL SPI observation and expressing it in terms of unit volume rather than per detector.

Aeff.out is the effective area of the GRL Configurations simulated as a function of energy.

Sens.out is the sensitivity of the GRL configurations simulated as a function of energy.

geosens.out is the sensitivity of the GRL configurations simulated as a function of geometry at one or more selected energies.

All output files are simple ascii text format.

5.4 Results

In order to test the sensitivity analysis model, the geometry of the MAX Laue lens was investigated, with the resultant sensitivity analysis compared to the reported sensitivity. Figure 5.3a shows the result of the GRL sensitivity model for the MAX geometry and 5.3b the projected sensitivity for the MAX mission as reported in [2].

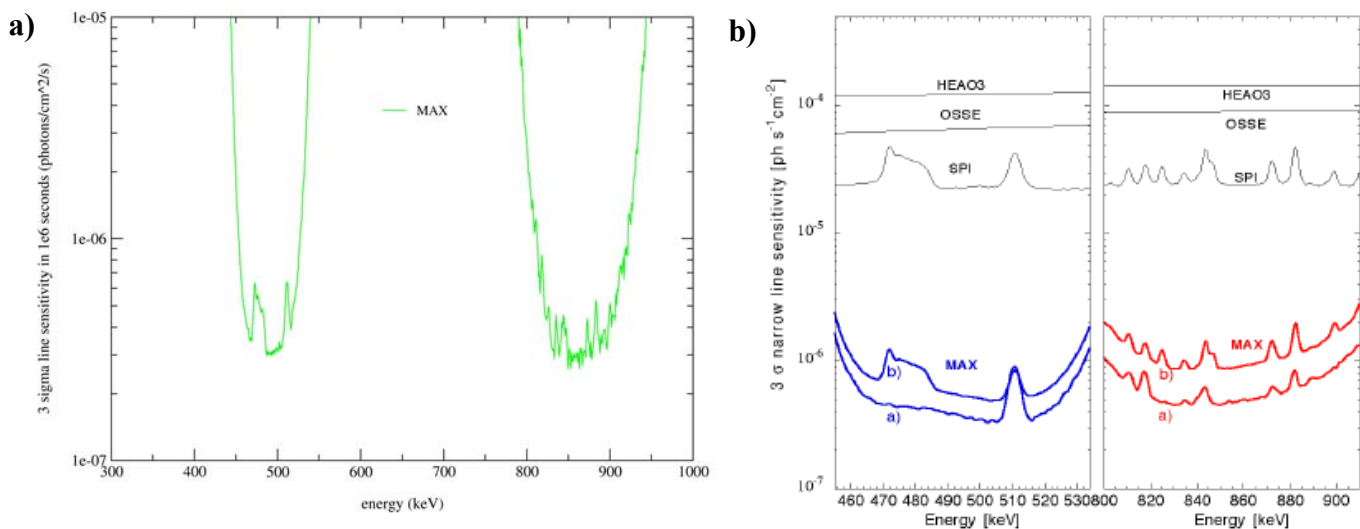


Fig 5.3a The 3σ sensitivity analysis result for the MAX mission using the sensitivity model developed for the GRL mission. **5.3b** 3σ narrow line sensitivity of MAX compared with the achieved sensitivities of earlier missions, as reported in [2]. Curve (a) is based on the TGRS Ge detector, scaled for background reduction, whereas (b) is based on the measured background of INTEGRAL SPI.

It can be seen from comparing figures 5.3a and b that the model developed for the GRL is in very close agreement with the model used by the MAX mission team. The MAX team has assumed a further improved background rejection development over INTEGRAL SPI (MAX curve (a) in 5.3b), however, the GRL model will continue to assume a background rejection similar to SPI.

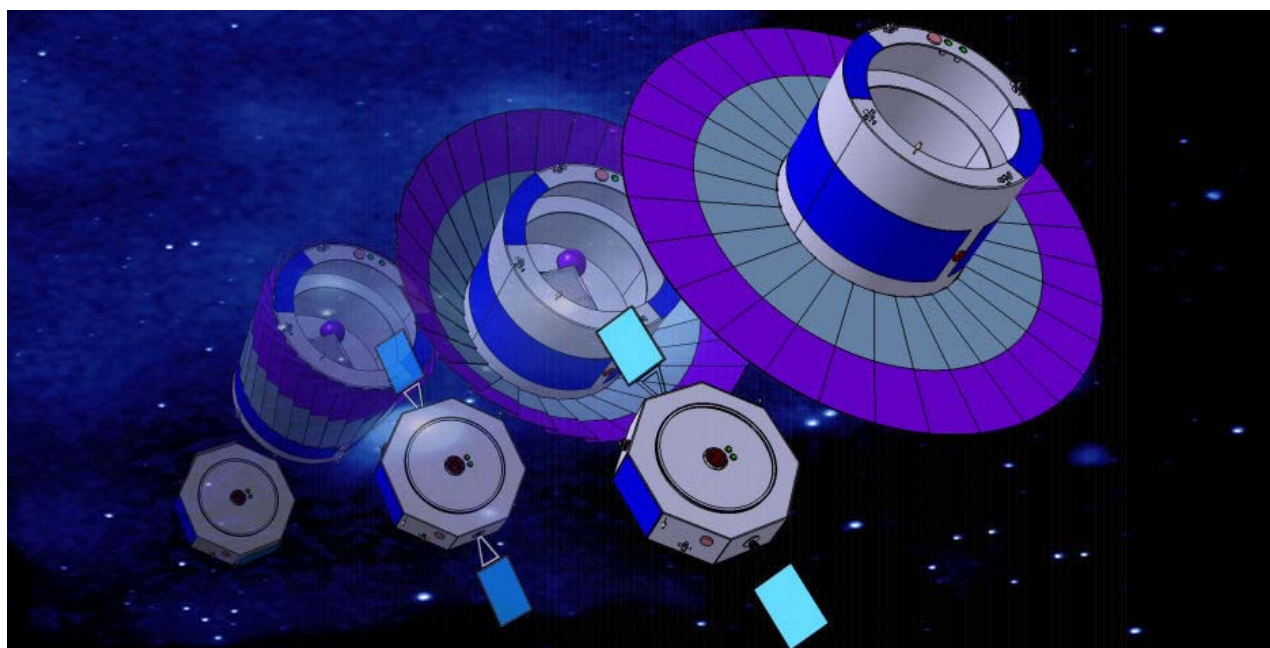
5.5 References

- [1] A comparative study of possible future nuclear astrophysics missions, M. Beijersbergen, Cosine Report, CSC-ODS-TN5, 2004
- [2] The MAX Mission: focusing on high sensitivity gamma-ray spectroscopy, P.von Ballmoos et al., Pre-print, prepared for the INTEGRAL workshop 2005 (See Appendix A).

PART II

GAMMA RAY LENS

MISSION DESIGN



6. Other Missions Useful to the GRL Design

There are three very relevant missions that were used as references in the Gamma Ray Lens TRS: Claire, a gamma-ray focussing Laue lens balloon demonstration, MAX, the subsequently proposed Laue lens formation-flying mission and XEUS, ESA's proposed X-ray observatory for the post-XMM Newton era. This section outlines these 'missions', highly relevant to the GRL study.

6.1 Claire and MAX

This section will outline two of the most significant 'missions' relevant to the Gamma Ray Lens: CLAIRE, a narrow band Laue lens experiment carried on a high-altitude balloon in June 2001 and MAX, a mission subsequently proposed by the same CESR group responsible for CLAIRE. MAX will use a broad band Laue lens to investigate gamma ray lines in regions of explosive nucleosynthesis. A narrow band lens uses different crystal planes to focus all crystals to a small (~ 20 keV) energy band, likely detecting one gamma-ray line. A broad band lens uses a much smaller number of planes, coupled with increasing ring radii, to cover a larger energy band (> 100 keV).

6.1.1 CLAIRE

The CLAIRE project was a research and development activity conducted by a team in CESR, Toulouse, France, lead by Peter von Ballmoos. The primary aim of the activity was to demonstrate the feasibility of Laue Diffraction as a means of focusing gamma rays. CLAIRE was flown on June 14th 2004 on a stratospheric balloon by the French Space Agency, CNES. The aim was to observe the Crab nebula and, using a Laue lens, focus 170 keV photons onto a 3x3 Ge detector.

6.1.1.1 The CLAIRE Instruments

The CLAIRE lens consisted of 556 germanium crystals mounted on 8 rings. The lens was a narrow band-pass lens, where all crystals were oriented such that each ring focused photons of $170 \text{ keV} \pm \sim 10 \text{ keV}$. The geometric area of the lens was 511 cm^2 , concentrating the photons to a focal point 1.5 cm in diameter at a focal length of 277 cm. Fig. 6.1 shows the CLAIRE optic.



Fig 6.1 The CLAIRE lens, being mounted on the balloon gondola

The focal plane instrument used in the CLAIRE project consisted of a 3x3 array of high purity Ge detectors (fig.6.2) [2]. The detectors were housed in a cryostat, cooled by liquid nitrogen. Background rejection was aided using a CsI:Tl side shield and BGO collimators.

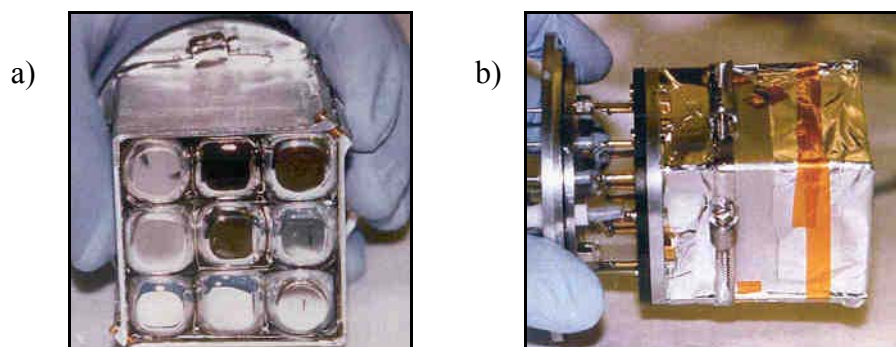


Fig. 6.2 a) Front-on view of the 3x3 Ge array detector and b) profile view of the detector array

The CLAIRE gondola (fig. 6.3) provided stabilisation to the gamma ray lens to a few arcseconds. Developed by the balloon division of CNES, the gondola has two separate pointing stages. Firstly, one system provides stabilisation to within 10 arcminutes. Then, a fine pointing system,

based on a gimbal, is capable of pointing the lens to within a few arcseconds of its target. In order to accurately point the lens at the source (on the ground as well as in flight), a rotating

optical telescope with a CCD camera is mounted in the center of the instrument. When looking at an optical source while this telescope is rotated, the image on the CCD describes a circle whose center gives the direction of the rotating axis. This invariant pixel is then used to represent the

lens axis. The 3m balloon structure is mainly constructed of carbon fibre spars and honeycomb platforms, the total balloon payload weighing 500 kg.

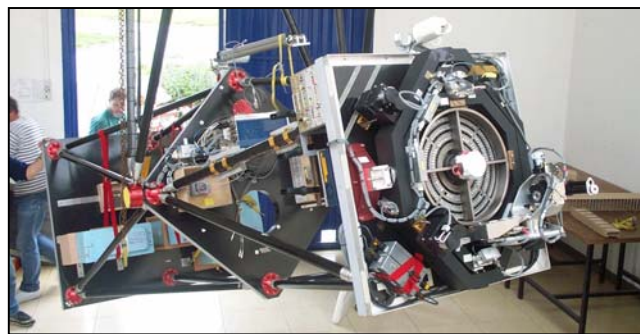


Fig. 6.3 The CNES-built gondola, holding the CLAIRE lens and detector array

6.1.1.2 The CLAIRE Balloon Flight

The CLAIRE flight lasted nearly six hours at its nominal flight altitude, having been launched from the CNES base in Gap-Tallard in the French Alps. It was recovered close to Bergerac in Southwest France. Figure 6.4 shows the flight path of CLAIRE.

The anticoincidence shield reduced the background detected by a factor of 10, the continuum count being 2.3×10^{-4} counts $s^{-1} \text{ keV}^{-1} \text{ cm}^{-3}$ at 170 keV [3]. The measured energy resolution during flight was ~ 2.5 keV FWHM.



Fig. 6.4 The CLAIRE balloon flight path. Takeoff at Gap-Tallard in the French Alps, landing in southwest France approx. 6 hours later.

Before and after the balloon flight, the diffraction efficiency of the lens was measured using a ^{57}Co source, both tests showing virtually identical efficiencies of $\sim 7\%$ at 122 keV (assuming a mosaicity of $70''$).

6.1.1.3 CLAIRE Results

The flight background spectrum (fig 6.5) shows that the background is dominated by three main lines: 139.7 and 198.4 keV from Ge transitions and the e^+e^- annihilation line at 511 keV.

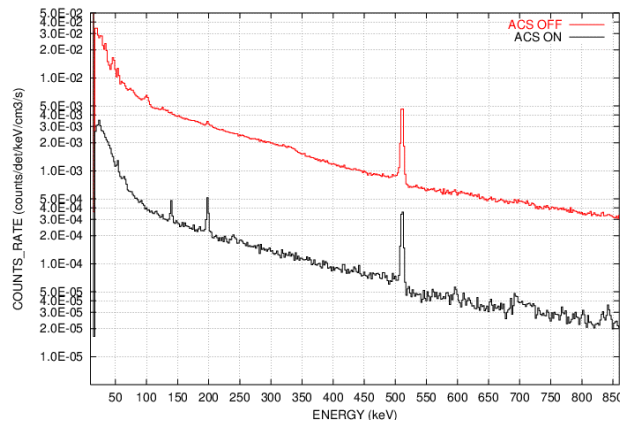


Fig. 6.5 CLAIRE background flight spectra showing the ACS both on and off

A comprehensive simulation of the observation was made and a 4.5σ detection was expected. Initial data analysis did not result in a positive detection of the Crab, however (Haloïn et al., 2003). It was found that an offset occurred due to a prismatic effect in the pointing system CCD sun-filter which would result in a broadening of the 170 keV peak to 8 keV FWHM. As a consequence of the uncertainty of the focal spot position, 30 data analysis trials were made. The most statistically significant of the trials was found by assuming offsets of +5 mm and +10 mm in the vertical and horizontal directions respectively.

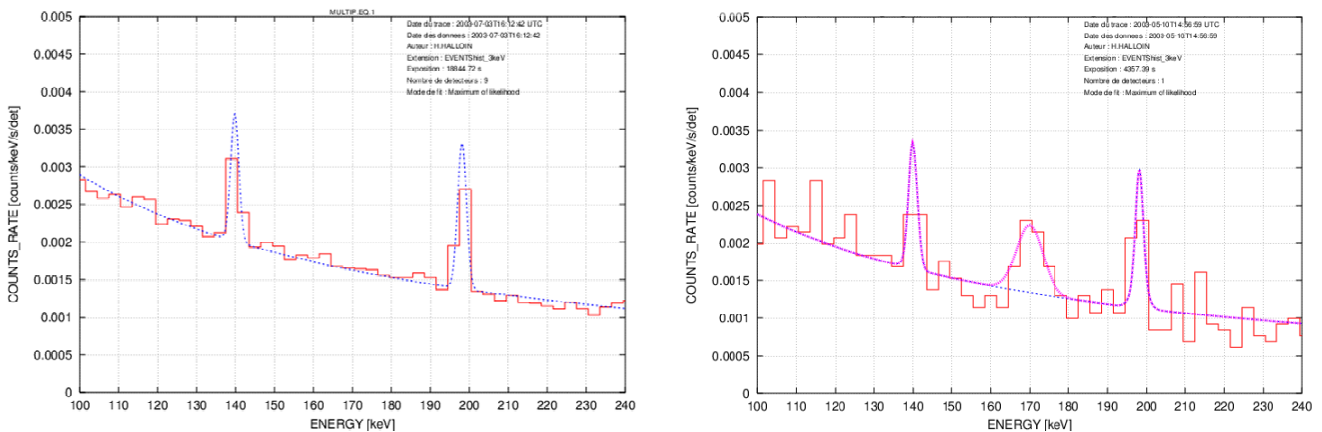


Fig 6.6 a) Background spectrum for single events and b) Reduced spectrum for single events recorded during time intervals with good Crab pointing at 170 keV

Figure 6.6b shows the reduced spectrum for single events recorded during time intervals with good Crab pointing at 170 keV. An excess of 33 photons were detected, corresponding to a significance of 3σ (~ 0.99898).

6.1.1.4 CLAIRE Conclusions

During the 2001 CLAIRE experiment, an astrophysical source was observed with a Laue Gamma-ray lens for the first time. This experiment for the first time, demonstrated the potential of a Laue lens for use in nuclear astrophysics. The experience gained in the CLAIRE project will be invaluable for any future Laue lens mission.

6.1.2 MAX

With the concept of a Laue lens demonstrated with the CLAIRE project, the CESR group have moved their emphasis to a space-borne mission called MAX. A space-based mission would allow significantly longer observation times, longer focal lengths, bigger masses and more stable observations. MAX is currently baselined for an L2 Orbit. This section introduces the mission concept behind MAX and its expected performance.

6.1.2.1 The MAX Mission Science Objectives

The reference science objectives used in the MAX mission focus on the investigation of gamma ray lines in regions of explosive nuclear synthesis. In particular, it is cited [7] that the primary scientific objective of MAX is to study the 847 keV $^{56}\text{Ni} \rightarrow ^{56}\text{Co}$ decay from supernovae Ia. Supernovae Ia are standard candles and understanding the intensity, shape and shift of the gamma ray line will aid in determining a more accurate model for this important astrophysical phenomenon. Another important objective is the study of the 511 keV line, which is expected to arise from many sources (see section 2.1.4). MAX's capability for measuring polarisation could potentially be crucial in resolving the 'MeV blazar' problem. From these primary science objectives, the two energy bands observed with MAX are 460-522 keV and 825-910 keV.

6.1.2.2 The MAX Instruments

The long focal length of the MAX gamma ray lens results in a two-spacecraft formation-flying concept (fig 6.7): an optic spacecraft carrying the Laue lens and a detector spacecraft placed 133m away at the focal point of the lens. The Lens module is composed of 8200 crystals of copper and germanium, the crystals mounted in 24 concentric rings. The inner rings are made of copper, focusing the higher energy photons to the focal point, whereas the outer rings are of germanium and focus photons from the lower energy band of interest. Table 6.1 shows a summary of the lens parameters.

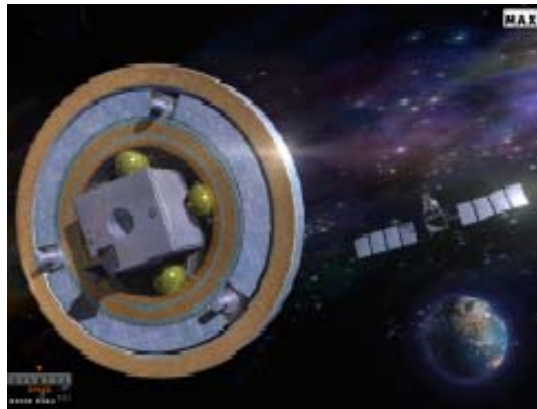


Fig. 6.7 An artists impression of MAX, showing the two spacecraft flying in formation

Crystal Material	Inner Radius	Outer Radius	Energy Band
Copper	0.87m	0.96m	825-910 keV
Germanium	0.97m	1.10m	460-522 keV

Table 6.1 Summary of the MAX Laue lens parameters

The expected effective area of the MAX lens is shown in figure 6.8.

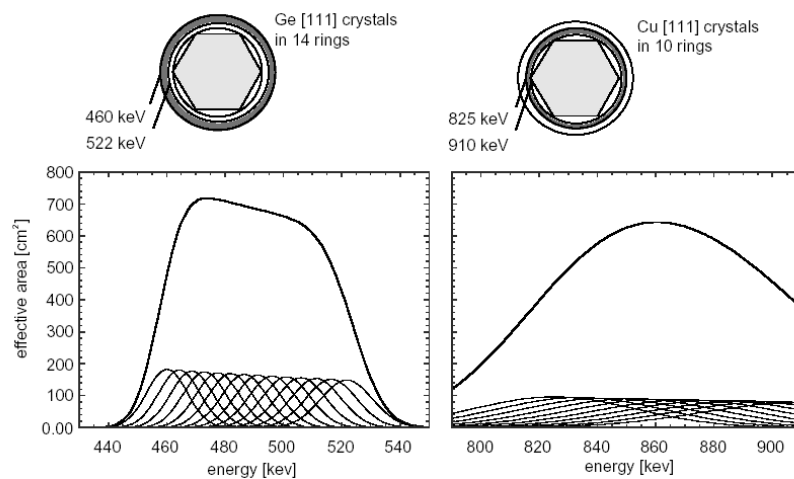


Fig. 6.8 Expected effective area curves for the two MAX crystal rings

The baseline detector for MAX is a stack of planar Ge detectors using orthogonal strips. Other alternative detectors are mentioned in MAX literature, including 1) a single high purity Ge detector (SPI/INTEGRAL type) actively shielded by a BGO scintillator and passively cooled, 2) an efficiency optimized narrow FOV Compton camera featuring Si strips and CdTe pixels (Takahashi 2003) or 3) an array of low temperature calorimeters (detection of photons produced by impinging photons, Giuliani, A., 2001) [6]

There are advantages in using a detector providing localization of the gamma-ray interaction. The focal spot can be tracked across the focal plane, off-axis detection is enabled and simultaneous background observation is conducted by pixels not encountering the focal spot. In addition, systems with 3D event localisation allow Compton kinematics to be used, which significantly reduces background counts (see section 4.2.3).

There is also the possibility of placing a larger FOV monitor on MAX. For example, an optical monitor could provide contemporaneous high precision multicolour photometry for the pointed target, particularly useful for Supernova observations. The monitor would have a large field of view and good angular resolution, capable of resolving the target from the host galaxy's light. An X-ray monitor could also be used, where only a coded mask on the optic spacecraft is required since a suitable detector exists on the DSC. The X-ray monitor may also allow the alignment of the spacecraft to be verified by detecting the high-energy emission from the weaker source.

6.1.2.3 Mission Architecture and Budgets

It is expected that MAX could be ready for launch in 2010 assuming the Phase A study can be conducted in a 12 month period starting in 2005. In conjunction with EADS Astrium, preliminary mass and power budgets have been established (fig. 6.9) [7].

	LENS SATELLITE	DETECTOR SATELLITE
PLATFORM	266	283
Structure	78	78
AQCS/GNC	14	14
Chemical propulsion	50	67
Thermal	10	10
Data Handling	24	24
Power	58	58
RF Communication	33	33
FF PAYLOAD	30	70
RF metrology	24	24
Optical metrology	2	19
Cold gas propulsion	0	23
FF Interface Unit	4	4
SCIENCE PAYLOAD	252	72
Crystals set	180	
Supporting frame	72	
Passive radiator		24
Detection plane		36
Electronics		12
TOTAL	548 kg	425 kg

Fig. 6.9a Preliminary Spacecraft Mass Budgets for both Lens and Detector Spacecraft, including 20% margin

	Observation	Earth comms	Re-targetting
PLATFORM	136	136	160
AOCS/GNC	25	25	25
Chemical propulsion			24
Thermal	36	36	36
Data handling	20	20	20
Power	18	18	18
RF Communications	36	36	36
FORMATION FLYING	24	24	24
SCIENCE PAYLOAD	24	24	24
TOTAL (W)	184	184	208

	Observation	Earth comms	Re-targetting
PLATFORM	136	136	160
AOCS/GNC	25	25	25
Chemical propulsion			24
Thermal	36	36	36
Data handling	20	20	20
Power	18	18	18
RF Communications	36	36	36
FORMATION FLYING	48	24	24
SCIENCE PAYLOAD	156	156	156
TOTAL (W)	340	316	340

Fig. 6.9b Preliminary Power budgets for the lens (left) and detector (right) spacecrafts, including 20% margin

The mission will be based in a natural Lissajous orbit at L2. As can be see in figure 6.9a), the combined total mass of both spacecraft is approximately 1000kg and has led to the Soyuz ST Fregat being chosen as launcher (see Appendix A). The launch capability of a Soyuz ST to L2 is approximately 2000 kg. Figure 6.10 shows the two spacecraft in the launch stack.

The spacecraft are expected to separate directly after launch, and fly independently to L2 at a safe distance of a few tens of kilometres where they will be injected into L2 and establish formation flight with a series of course and fine RF and optical metrology systems.

Further detail on the proposed MAX metrology and formation flying and other spacecraft systems can be obtained in [7].

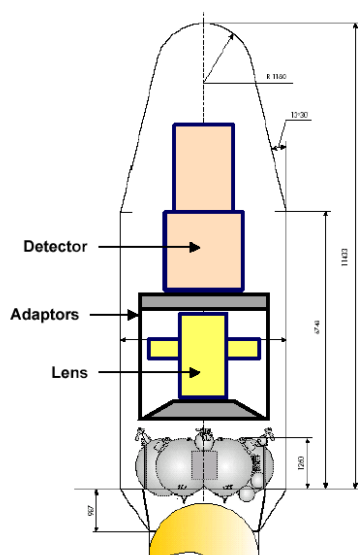


Fig. 6.10 Lens-Detector launcher accommodation in the Soyuz-ST fairing

6.1.2.4 MAX Performance

The figure of merit for MAX is the narrow line sensitivity of the configuration. Figure 6.11 shows the expected narrow line sensitivity of the two energy bands in MAX, as well as shows the improvement expected on previous gamma ray missions. The background rejection in these figures is assumed to have improved on the INTEGRAL rejection through the use of Compton kinematics.

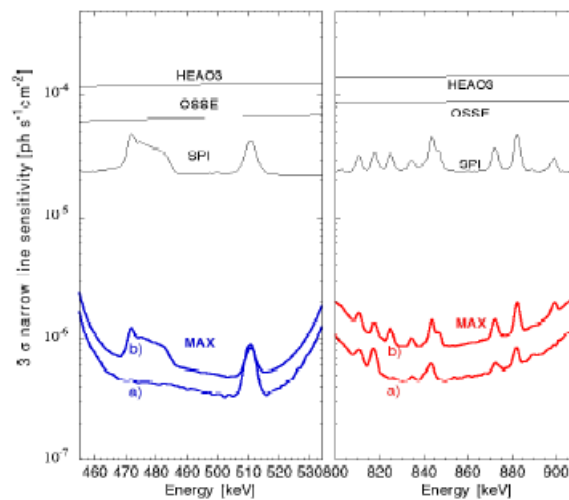


Fig. 6.11 3σ narrow line sensitivity of the MAX mission in the two energy bands of interest.

It can be seen from figure 6.11 that the MAX mission is expected to greatly improve on previous missions with respect to narrow line sensitivity. The angular resolution of the lens is related to the mosaic width of the crystals and, for MAX, is expected to be approximately 45 arcseconds. It is important, also, to note that the MAX lens is not an imager, but a focuser.

6.1.3 Conclusions

The MAX mission consists of two relatively small spacecraft flying in formation in a low Earth orbit. Computer models have been produced to estimate the narrow line sensitivity of the Laue lens and it has been shown to have a significant improvement on previous missions such as INTEGRAL. The MAX mission concept has provided insight into how a Laue Gamma Ray Lens mission could be investigated, and provided a means by which the models constructed for the GRL could be tested and verified.

N.B. The MAX mission is still in a process of evolution. The most recent document [6] from the MAX team reports some changes to the lens configuration, including the values in table 3.1

6.1.4 References

- [1] CLAIRe's first light, Peter von Ballmoos et al., *New Astronomy Reviews* 48 (2004) 243-249
- [2] CLAIRe: Premieres Lumieres d'une Lentille Gamma, Huber Halloin, Thesis, 2003
- [3] CLAIRe gamma-ray lens: flight and long distance test results, H. Halloin et al., SPIE 2003.
- [4] A Gamma Ray Lens for Nuclear Astrophysics, P. Von Ballmoos, Internal presentation, ESTEC 2004
- [5] MAX – A gamma-ray lens for nuclear astrophysics, P.von Ballmoos et al., SPIE 2003.
- [6] The MAX Mission: focusing on high sensitivity gamma-ray spectroscopy, P.von Ballmoos et al., Pre-print, prepared for the INTEGRAL workshop 2005.
- [7] Small-Sat Platforms and Formation Flying: An opportunity for the Gamma Ray telescope, MAX, J. Borde and P. Von Ballmoos, preprint paper 2005.

6.2 XEUS

XEUS, the X-ray Evolving Universe Spectroscopy mission, is a potential successor to XMM-Newton as ESA's primary X-ray observatory. With a higher energy observation capability, combined with a very large effective area, XEUS will provide an enormous extension of scientific capability. Large technological leaps are required in order to realise the large effective area, and the desired energy band. There are many similarities between the XEUS mission and the Gamma Ray Lens, both technologically and operationally. This section will introduce the concepts of the XEUS mission and will draw particular attention to the similarities between XEUS and the GRL missions.

6.2.1 The XEUS mission

6.2.1.1 Scientific Objectives and Specifications

As the name implies, XEUS will observe sources associated with the evolution of the X-ray universe. The goals of XEUS are to study the evolution of the hot baryons in the Universe and, in particular, to detect massive black holes in the earliest AGN and to estimate their mass, spin and red-shift. XEUS will study the formation of the first gravitationally bound, Dark Matter dominated systems, and will conduct high-resolution spectroscopy in the investigation of the evolution of metal synthesis. Characterisation of the intergalactic medium through the study of absorption line spectra will also be undertaken.

In order to meet these scientific objectives, a large effective area and high spatial resolution are required. An effective area of $\sim 10\text{m}^2$ at 1 keV is desired, with a spatial resolution of 2-5''. This will result in a sensitivity improvement of ~ 200 times greater than XMM-Newton. Such demanding scientific requirements will be met by exploiting the novel technology of Silicon Micropore Optics (See section 3.1.3.1)

The Silicon Micropore Optics will be coated in a multilayer mirror coating. The multilayer mirror technology will greatly increase the energy capability of the observatory, allowing observations of hard X-rays up to approximately 40 keV. In addition, the multilayer mirror will automatically provide an extremely large collecting area at lower energies, enabling the investigation of bright nearby objects with dedicated high-throughput, polarimetric and time resolution detectors.

The prime science goals may be divided into four main themes: 1) the evolution of large scale structures; 2) the birth and growth of the first massive black holes and their effect on the growth of galaxies; 3) the study of gravity in the strong field limit and the search for deviations from General Relativity and 4) the study of matter under extreme (supra-nuclear) conditions. High-energy studies address key questions in astronomy and cosmology, the unprecedented sensitivity and timing capabilities of XEUS extending these investigations into the next stage of X-ray astronomy [1].

6.2.1.2 The Mission Baseline

The original XEUS mission configuration [2] using XMM-style nested nickel shells, required the rendezvous of the mirror spacecraft with the International Space Station, where robotic assembly would increase the mirror diameter – using mirror segments delivered by the Space Shuttle - in order to meet the effective area requirements. This extremely expensive and complex mission scenario would have been prohibitive and, as such, the XEUS Science Advisory Group endorsed the study of a revised mission scenario. Two XEUS studies were conducted in 2004 at the ESTEC Concurrent Design Facility (CDF). One of the main aims of the new mission baseline is to have complete autonomous deployment of the mirror, avoiding the complexity added to the mission by visiting the ISS.

In order to realise this main objective, new novel optics are under development [3]. Silicon Micropore Optics (see section 3.1.1) allow for extreme mass and volume reduction, without losing effective area and/or resolution. The current state of development of this technology is promising, ensuring that a 10m^2 effective area with a 2-5'' spatial resolution will be achievable with a single launch and autonomous deployment [4].

There are three main options with regard to the mission launcher: 1) A dual launch configuration utilising two Soyuz Fregat 2-1b, the MSC and DSC launched at separate times (2050 kg per launcher payload capability); 2) a single launch using the Ariane 5 ECA (6800 kg payload capability) and 3) a single launch with a US Delta Heavy launcher (9300 kg payload capability). The current baseline configuration assumes an Ariane 5 launch. The payload capabilities quoted are for direct injection trajectories to L2.

The large mirror, with $\sim 10\text{m}^2$ effective area, requires a large focal length of $\sim 50\text{m}$. As such, two spacecraft will be used: the mirror spacecraft (MSC) and the detector spacecraft (DSC) since one spacecraft is impractical. Currently, ESA is expected to provide the MSC while the USA and Japan would provide contributions in the other mission elements e.g. the launcher, DSC and metrology systems. The two spacecraft will be launched as a stack (fig. 6.12), utilising an Ariane 5 long fairing, the DSC mounted on 'top' of the MSC.

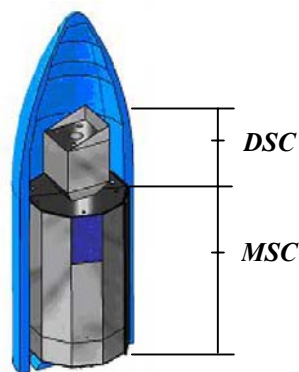


Fig. 6.12 MSC and DSC stacked in the long fairing of the Ariane 5

After launch, the spacecraft, still in stacked configuration, enter the cruise, or BBQ (1 rpm), mode where outgassing and decontamination occurs. Following the final injection manoeuvres, the spacecraft separate and are deployed, moving a safe distance away from each other. After deployment of the mirror, only cold gas propulsion is used by the MSC in order to avoid contamination of the optics.

The mission will be based in a zero-eclipse halo orbit at the second Libration point, L2 (fig.7.1), making use of the negligible gravitational gradient ($\sim 10^{-13} \text{ s}^{-2}$). See section 7 for a more detailed account of the orbit selection.

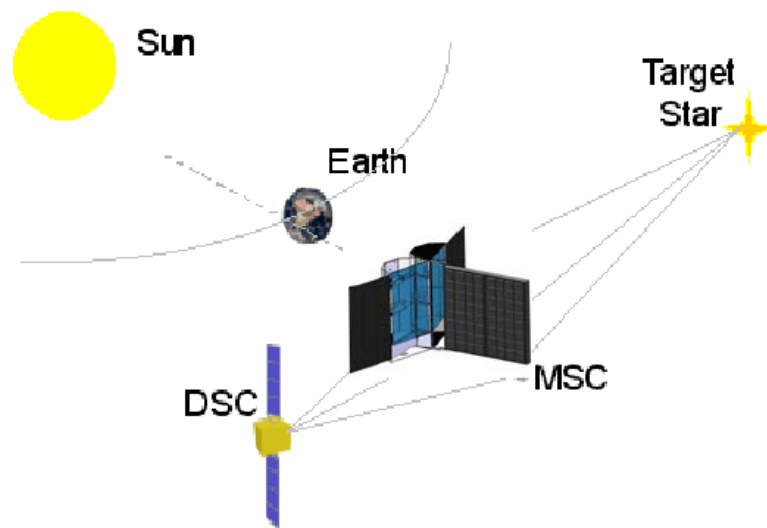


Fig 6.13 XEUS spacecraft elements configuration in target orbit at L2

Formation flying between spacecraft is an important driver of the mission, the nature of the optics onboard XEUS having stringent alignment requirements if the scientific specifications are to be realised. The optical metrology system has the following requirements if alignment of the spacecraft is to be maintained.

- Longitudinal metrology to 750 μm to maintain the focus
- Lateral metrology to 330 μm to control the focal spot on the 5mm detector on the DSC
- Continuous pitch and yaw measurement to ± 10 arcseconds, which allows ± 1 arcminute attitude control to avoid vignetting.

The average time of an observation is 3×10^5 seconds (~ 3.5 days). The mission duration is expected to be 15 years + 5 years extension (also the lifetime of the MSC). It is also expected that the detector spacecraft will be replaced at its end of life (~ 5 years) or when newer, improved detectors become available. XEUS is expected to be launched in the 2015-2025 timeframe.

6.2.1.3 XEUS Design Drivers

The CDF studies conducted for the XEUS mission recognised key design drivers. The following is a list of the key issues that drive the design of the XEUS mission, as reported in the XEUS CDF study [5].

- Formation Flying and Rendezvous
 - Major issue for DSC AOCS: required relative range error during nominal formation keeping imposes autonomous control system
 - Ranging accuracy from ground segment: operations and rendezvous strategy
- MSC Lifetime
 - The long lifetime of the spacecraft imposes very low consumables, simple and reliable design of the service module.
- Launch vehicle, cruise phase and injection strategy
 - Drives the maximum launch mass (mirror area), cost and programmatics
 - Composite launch has direct impact on the cruise phase (MSC design)
- Petal mass:
 - Petal mass is strongly dependant on:
 - Petal location
 - Petal size
 - Number of petals
 - How the mirror is populated by the petals
 - Total mirror performance (science output) depends on the above petal characteristics. Petals are a large contributor to the total MSC wet mass.
- Petal Interface:
 - Requires a large number of actuators on MSC and optical detection system to compensate for initial mirror misalignment
 - Petals locking during launch
- Temperature gradients in the mirror plane:
 - Direct impact on MSC configuration e.g. sun shield
- Temperature gradients along the mirrors in the optical axis:
 - Off-normal sun angle to be limited to about 5°
- Mirror contamination prevention
 - BBQ mode until outgassing is completed
 - Protect the mirror during the outgassing procedure
 - Use Hydrazine thrusters only in the closed configuration. Once deployed, the MSC will use only cold gas for AOCS manoeuvres.

See appendix D for a table summarising the XEUS mission and MSC design.

N.B. The ESA CDF studies did not consider the DSC in detail as the DSC concept is to be provided by the Japanese Space Agency (JAXA). However, the following critical issues for the DCS have been identified.

- Cryogenic chain design & performance
- Payload accommodation
 - Detector type
 - Lifetime

6.2.2 Gamma Ray Lens: XEUS Similarities

There are many key similarities between the Gamma Ray Lens and the XEUS mission. The following highlights areas where the Gamma Ray Lens mission will benefit through the lessons learned in XEUS, drawing attention to similarities in the mission profile as well as similarities in various subsystems. Subsystem similarities will allow good estimation of preliminary budgets.

- **Mission Analysis / Mission Control**
 - Location of orbit (L2)
 - Type of orbit (Halo)
 - Same duration launch windows
 - Launcher type (Ariane 5)
 - Single launch
 - Trajectory and injection manoeuvre
 - Formation flying operations
- **Baseline Mission**
 - 2 Space craft (Optic and Detector)
 - Single launch using Ariane 5 launcher
 - Lens spacecraft only rotates at its centre of gravity – no translation manoeuvres during target acquisition
 - Detector spacecraft, virtually locked to the lens spacecraft, translates as well as slews around its centre of mass during target acquisition
 - The Gamma Ray Lens requires a larger focal length than XEUS
 - Mass budget similarities for certain subsystems: Thermal, Communications, Data Handling, AOCS, Power

- **Design Driver Similarities**
 - Formation flying and rendezvous
 - Minimal consumables on optic craft
 - Launch vehicle and injection strategy
 - Stack architecture
 - Large MSC element
- **Similar Subsystems**
 - AOCS: Classical AOCS design
 - Communication
 - Optical and RF metrology
 - Power
 - Data handling

6.2.3 Conclusions

It is evident that there are many similarities between the XEUS mission and the Gamma Ray Lens. With XEUS as a precursor, the Gamma Ray Lens would benefit greatly. Much of the research and development for XEUS is directly transferable or capable of extrapolation for use in the GRL mission. As such, many of the subsystem values used in the XEUS budgets are also used to compile the budgets for the Gamma Ray Lens. The XEUS CDF sessions have also aided the design of the GRL mission baseline, when the crossover areas discussed in this section were taken into account.

6.2.4 References

- [1] Science with XEUS – the X-ray Evolving Universe Spectroscopy Mission, A. N. Parmar et al., SPIE, SCI-SA/053, 2004
- [2] XEUS: an X-ray Observatory for the Post-XMM era, M J L Turner et al., The Next Generation of X-ray Observatories: Workshop Proceedings, University of Leicester, XRA97/02, 1997
- [3] Status of X-ray Optics Development for the XEUS Mission, Marcos Bavdaz et al., SPIE Proceedings, 2004/SCI-A/010
- [4] XEUS Mission Reference Design, M. Bavdaz et al., SPIE Proceedings, 2004/SCI-A/012
- [5] XEUS CDF Study Report, CDF-31(A) October 2004

7. Orbit Selection

The Gamma Ray Lens is reliant on the following requirements to achieve its science goals.

- Long, stable observations for formation flying between two spacecraft
- Typical observation times of ~2-3 weeks
- Large portion of the sky visible at any one time
- Stable thermal environment
- Low number to no eclipse periods
- Minimal radiation damage to the detectors and other systems
- Launcher capable of efficiently lifting a large mass
- Low Δv requirements for orbit insertion and maintenance

Choice of orbit will depend on the mission requirements, so a trade-off will be made on different orbit types. Low Earth Orbit (LEO), Geostationary Earth Orbit (GEO), Highly Elliptical Orbit (HEO) and orbits at L2, the Sun-Earth Co-linear libration point, will be considered.

7.1 Orbit Type and Trade-off

For the purpose of this trade-off the different orbit types will be rated -2, -1, 0, 1 or 2 based on negative, neutral or positive characteristic with regard to the mission requirements.

Mission Requirement	LEO	GEO	HEO	L2	Weighting
Stability and maintenance Δv	-2	0	-1	2	1
Observation period	-2	-1	0	2	1
Visibility of the sky	-2	0	1	2	1
Thermal environment stability	-1	1	0	2	0.5
Eclipse periods	-2	-1	-1	2	0.5
Radiation environment	-1	1	-1	1	0.25
Communications and ground operations	0	2	1	0	0.25
Launcher capacity	2	-2	0	-1	1
Total	-8	2	-1	10	-
Weighted Total	-5.75	-2.25	-0.50	7.25	-

Table 7.1 Table outlining the trade-off between orbit types for the GRL mission requirements

Table 7.1 summarises a basic trade-off in order to establish the best orbit for the gamma ray mission. The mission requirements are based on both spacecraft working simultaneously to meet the scientific objectives. As the configuration requires ‘non-keplarian’ formation flying between two satellites, during the trade-off the two spacecraft were considered as one system.

The trade-off clearly shows that the most suitable orbit that meets the mission requirements is the region around the Earth-Sun co-linear libration point L2, ~1.5 million kilometers from Earth (1/100 AU – see fig. 7.1). Low Earth Orbit is clearly unsuitable for this mission, scoring low on the trade-off. Formation flying in LEO is extremely difficult and could be potentially hindered through atmospheric drag. Eclipse periods are also extensive and frequent at LEO. HEO and GEO are both quite neutral orbits, where formation flying is less difficult than at LEO, although again, eclipse periods are frequent. The only drawbacks of an L2 orbit are the significantly lower launcher performance and the less favourable communication and ground station coverage.

A spacecraft at L2 will benefit from high stability, a relatively benign and stable radiation and thermal environment, and, over the period of one year, it would be possible to observe every part of the sky. For a mission requiring no eclipse period over its lifetime, L2 is ideal.

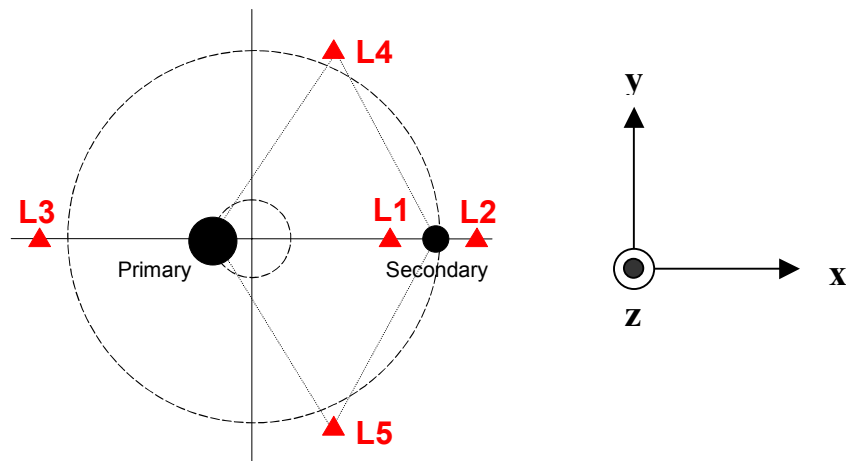


Fig. 7.1 The five libration points in the three-body problem and the related reference coordinate system.

7.2 L2 Orbit Type

Two potential classes of orbit are available around L2; Lissajous and Halo orbits.

7.2.1 Lissajous Orbits

Lissajous are the most studied L2 orbit types, with no less than five spacecraft expected to enter such an orbit from 2007. Lissajous orbits result from the stable solutions of the linearised equations of the ‘circular restricted three-body problem’. These orbits are essentially the natural orbital motion about the Lagrange points.

The main characteristics of Lissajous orbits are;

- Small orbital amplitude about L2 (in the order of 500,000 km)
- Enters the Earth’s penumbra approximately every 6 years
- Large insertion Δv required (in the order of 100 – 200 ms^{-1})

Fig. 7.2a) and b) show the expected lissajous orbit for the DARWIN mission [5]. Darwin is also a formation flying mission with ~ 4 spacecraft working in unison as a nulling interferometer. The spacecraft are expected to fly approximately 30m – 50m apart.

After approximately 6 years into the Lissajous orbit, the amplitude becomes greatly decreased and the spacecraft will enter the Earth’s penumbra, or shadow, and will become eclipsed. This is avoidable through an additional manoeuvre, increasing the orbital amplitude. The minimum Δv required for such a manoeuvre is 15 ms^{-1} . As the eclipse is avoidable using additional manoeuvres, for the purpose of the orbit trade-off the extra Δv is considered as opposed to eclipse period. A lissajous orbit would require at least an additional 115 ms^{-1} Δv for the purpose of orbit injection and eclipse avoidance compared to the halo orbit requirements (see section 7.2.2).

a)

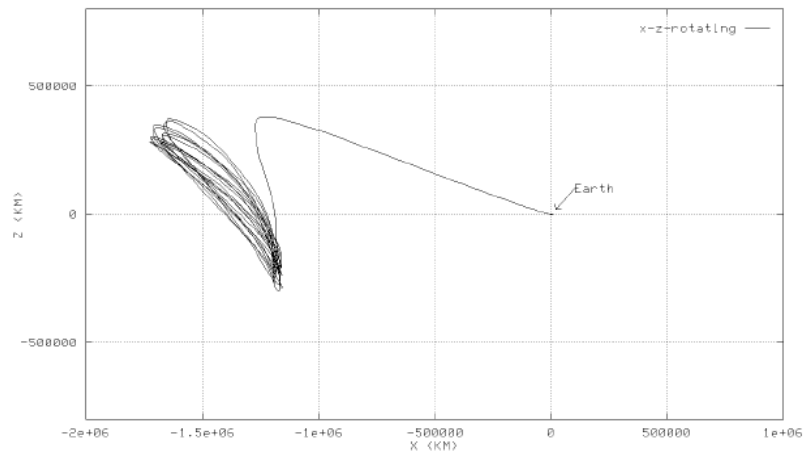


Fig. 7.2a) The Lissajous orbit as projected for the DARWIN planet-finding mission at L2. The sun is in the positive x direction.

b)

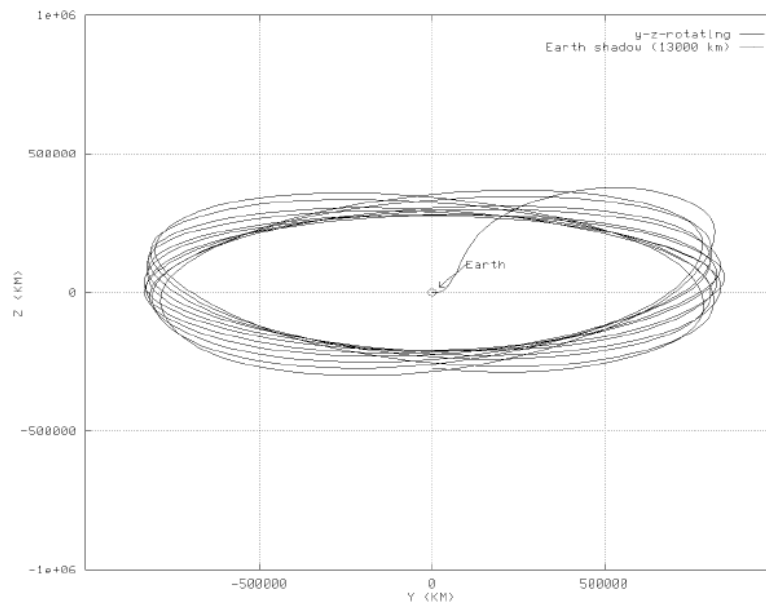


Fig. 7.2b) The same Lissajous orbit as above, from the viewpoint of the sun-direction.

7.2.2 Halo Orbits

A Halo orbit is quasi-periodic, resulting in very small perturbations and, hence, low orbital maintenance Δv . Halo orbits occur when the in-plane and out-of-plane motions are equal. Only small orbital maintenance manoeuvres, $\sim 5\text{cm.s}^{-1}$, are required every 20 days in order to maintain

the orbit. This results in a relatively small yearly orbital maintenance requirement of $1\text{--}2\text{ ms}^{-1}$ per year.

The key characteristics of a Halo orbit are;

- No eclipse period is experienced
- Large orbital amplitude (in the order of 800,000 km)
- No Δv required for orbit injection
- Low maintenance Δv required

Halo orbits result in a zero eclipse period over the mission due to their much larger amplitude than Lissajous figures. Comparing Fig. 7.2 and Fig 7.3 demonstrates the larger amplitude of Halo orbits. This larger amplitude introduces the need for a steerable or wide beam antenna for ground station communication.

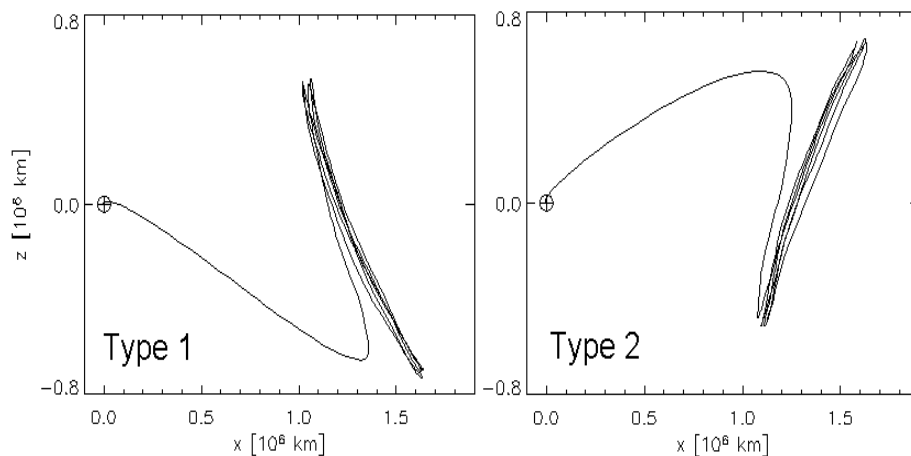


Fig 7.3 Two types of Halo Orbit

There are two types of Halo orbit achievable. One has its northern part tilted towards the Earth, the southern part tilted away. The other is its mirror image (fig. 7.3). In fig. 7.3, Earth is at the origin and the sun is in the negative x direction. The z direction is out of the ecliptic plane.

It is important to note that a large advantage of a halo orbit is the absence of an insertion Δv . Fig 7.4 shows the decrease of Δv required for insertion into larger L2 orbits.

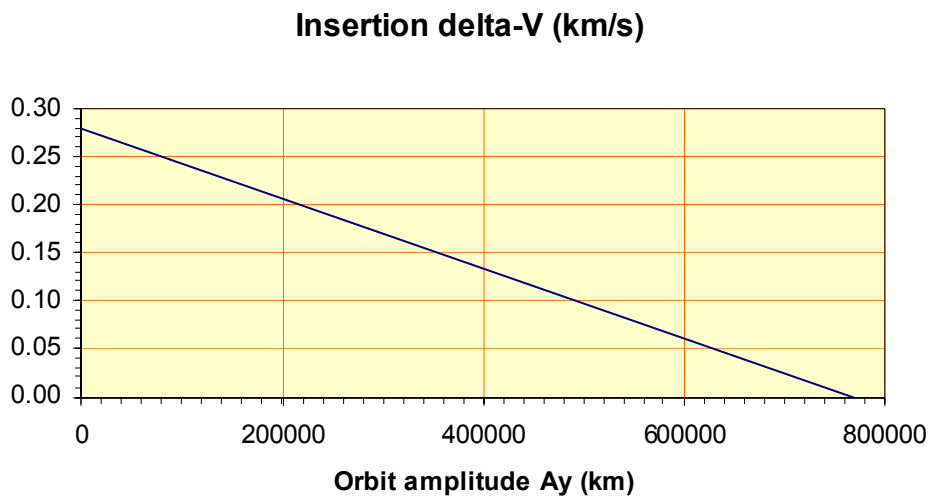


Fig. 7.4 Insertion Δv required at L2 as a function of orbit amplitude

As an example, XEUS is to be placed at L2 in a Halo orbit, primarily due to the requirement of no eclipse periods during the mission lifetime of ~20 years. The Gamma Ray Lens mission also

requires no eclipse period, although the projected mission lifetime is likely to be of the order of 10 years, extendible to 15 or even 20 years. The mission lifetime requirement arises from the science goal of observing the time evolution of type Ia supernovae. One evolution observation lasts approximately 80 days and, as the number of supernovae occurring per year are very limited, a long mission lifetime is necessary in order to observe a significant number of sources.

The trade off between the two different types of L2 orbit is simply the extra manoeuvres for injection and to remain out of eclipse in Lissajous, versus a moveable medium gain or wide-beam antenna while in Halo orbit. As the duration of the gamma ray mission is to be maximised, it is likely that two or three anti-eclipse manoeuvres will need to be performed if a Lissajous orbit is used. For this reason, also taking into consideration the relatively low telemetry needs of the mission, a wide-beam antenna in halo orbit is more attractive. It reduces the complexity of the mission as well as reduces the Δv requirement. For this reason, it is baselined to assume a Halo orbit at L2.

7.3 Orbit Selection Conclusions

In order to determine the best orbit for the GRL, a trade-off between orbit types was made. LEO, GTO, HEO and L2 orbits were considered. It was determined that in order to meet the mission objectives, an L2 orbit is by far superior to the other orbit types.

The two different L2 orbits, Lissajous and Halo, were then considered. It was shown that a Halo orbit, with a large amplitude (fig 7.3) would be the most suitable figure, benefiting from a lower number of orbital manoeuvres and zero eclipse periods during the mission. Maintenance manoeuvres will require a Δv of $\sim 1\text{-}2\text{ ms}^{-1}$ a year.

7.4 References

- [1] XEUS CDF Study Report, CDF-31(A) October 2004
- [2] ESA Presentation, Guy Janin, 2004

8. Mission Profile 1 – Soyuz Fregat

The Soyuz launch vehicle is an extremely reliable, relatively cheap rocket that, in recent years, has been used by ESA to launch science missions from Baikonour in Kazakhstan. The projected upgrade for this vehicle, the Soyuz Fregat (see Appendix A), will be available for launch from Kourou, the ESA space port, and so is considered as a potential launch vehicle for this mission.

8.1 Orbit Insertion

8.1.1 Direct Insertion to L2

Provided that a specific launch window is adhered to, direct injection of the spacecraft into L2 is possible. The Δv required to insert the craft into this orbit is small (fig. 7.4) and has no major impact on fuel requirements. Direct injection using a Soyuz-2.1b allows a maximum of 2050 kg to be launched. An Ariane 5 ECA, in comparison, is capable of 6800 kg direct launch to L2. Once the Halo orbit is established (section 7.1.2.), small manoeuvres can be used to remove the unstable part of the orbital motion. A direct launch benefits from simplicity, as well as a basic launcher cost, as no additional stages are required. The gravity loss from such a launch is also minimal.

8.1.2 L2 Insertion via Highly Elliptical Transfer Orbit (HEO)

An alternative, second option to direct injection was investigated using a Highly Elliptical Transfer Orbit to L2. In order to realise a HEO transfer, an additional propulsion unit is required as an upper stage. This also increases the launch capacity of the Soyuz-2.1b to a maximum of ~2300 kg. Table 8.1 shows the trade-off between the two launch options for the Souyuz-2.1b from the XEUS CDF run.

	Direct	HEO
Payload Mass	2050 kg	2300 kg
Additional Propulsion Unit	No	Yes
Launch window (for DSC)	One day every six months	No Restrictions
Radiation Dose	Low	High if many HEO revolutions
Gravity Losses	No	High
Injection Dispersion Correction	Marginally possible with AOCS	Comfortable with propulsion unit
LEOP duration	A few days	+ time in HEO
Eclipses	Short (75 min)	Several Hours
Mission Complexity	Low	Extra manoeuvres required
Mission Risk	Minimum	Additional risk attached to propulsion unit & manoeuvres

Table 8.1 Table showing the trade-off of direct Vs HEO launch for the XEUS mission.

The conclusion of this trade-off in the XEUS CDF was that, as long as the spacecraft mass could be limited to 2050 kg, a direct insertion to L2 is more desirable. It is more efficient and contains less risk than the HEO scenario. However, for a dual launch, where a rendezvous between crafts is required, a HEO transfer scenario is likely to be required to overcome the extremely small launch window constraint. In this scenario, the spacecraft will be launched into a HEO parking orbit where it will wait for the exact moment of L2 injection, in order to make the rendezvous with the first craft. In this way, the launch window can be made as large as desired.

For HEO, maintenance manoeuvres are required in order to maintain the perigee height. If the perigee decreases, there is a danger of entering the high atmosphere. It has been shown that for each 90000 km orbit, the perigee decreases by ~ 5 km. This results in $\sim 4 \text{ ms}^{-1} \Delta v$ required each week spent in HEO.

HEO results in large gravity losses. In order to reduce such losses, the HEO manoeuvre should be made in 2 steps (e.g. 180x40000 km, then 180x90000 km).

8.1.3 Launch Windows

Ideally, the Gamma Ray Lens would be launched in one Soyuz-2.1b from CSG, Kourou. Such a launch will have a window of two ten-week periods per year. The main constraint on this launch window is the inclination of the transfer orbit – the inclination is to be low in order to maximise launcher performance. The inclination is considered low when below 28.5° . Again, if required, this launch window can be increased using a propulsion module and a HEO transfer.

If a dual launch is unavoidable due to mass constraints, then a spacecraft rendezvous will be required. The XEUS mission analysis determined that, when a rendezvous manoeuvre between two spacecraft is required at L2, the launch window for the *second* craft is extremely small – just 1 day every 6 months. This constraint makes direct injection of the second spacecraft highly unlikely as, very often, launch postponements occur. In order to rectify this problem, a highly elliptical insertion orbit (HEO) was investigated. It was found that such an orbit is desirable under certain circumstances, as it allows the launch window to be extended by a few weeks. Sitting in a HEO, the spacecraft can be transferred to L2 injection without danger of launch postponement at the designated time (see section 8.1.2) [2].

8.1.4 Launch Profile Conclusions

A single launch, direct injection to L2 using a Soyuz 2-1b from Kourou is most desirable, on the condition that the mass of the two spacecraft is limited to 2050 kg. If the mass cannot be restricted to this, but can be kept below 2300 kg, a single HEO transfer can be used with the aid

of an additional propulsion module. HEO is, however, less desirable than direct injection (Table 8.1) due to increased mission complexity and the additional cost of the extra propulsion module.

A direct launch results in a launch window of two ten-week periods per year, calculated in order to utilise a low ($<28.5^\circ$) transfer orbit inclination.

If a dual launch is required, then a rendezvous manoeuvre will be needed. The first craft will have a launch window of two ten-week periods, as with a single launch. In order for a successful rendezvous, however, the *second* craft, if sent via direct injection, will only have a launch window of one day every six months. It is necessary, therefore, to at least launch the second craft via HEO in order to extend the launch window (section 8.1.3). The first craft may also be sent via HEO if the extra mass capability of the additional propulsion unit is required.

8.2 Optics Spacecraft (OSC)

8.2.1 Payload

The payload on the OSC is the Laue crystal lens. Using the effective area model (3.3.2) a lens suited to the fairing size and mass capability of a Soyuz-ST Fregat 2-1b was designed. The lens was optimised for two energy bands; 460-522 keV using the (111) plane of Germanium and 825-910 keV using the (111) plane of Copper. Table 8.2 outlines the main characteristics of the lens.

Material	Germanium	Copper
Energy Band	460-522 keV	825-910 keV
Inner Radius	3.18 m	2.85 m
Outer Radius	3.6 m	3.14 m
No. of rings	43	30
Volume of each crystal	1cm ³	1cm ³
No. of crystals (Packing factor = 0.85)	77736	427322
Mass	443 kg	449 kg
Focal length	436 m	436 m

Table 8.2 Main characteristics of the Laue gamma-ray lens, designed for a Soyuz-ST Fregat 2-1b.

Note that the lens size is larger than the diameter of a Soyuz ST fairing, implying the use of a deployment mechanism for the lens. A packing factor of 85% is also assumed, along with a 5% system margin for the crystal mass estimate.

8.2.2 Subsystems

At this stage in the TRS an in-depth investigation into each subsystem on board the OSC is not required. Once a baseline mission configuration is chosen on the basis of the achievable sensitivity, a more thorough investigation of subsystems can be undertaken. A brief description of the key subsystems is included here.

- **AOCS** – The spacecraft will have a classical AOCS control system as proposed in the XEUS CDF studies. Hydrazine thrusters can be used, as the risk of contaminating the Laue lens is negligible due to the high-energy photons that will be of interest. Table 8.3 shows the stability requirements of the GRL.

- **Metrology** – A metrology system modified from XEUS is assumed, having three main subsystems; 1) Coarse RF metrology, 2) Fine RF metrology and 3) Optical metrology. The OSC will not house the lasers required in optical metrology, but will have reflecting blocks used by the range finding and interferometer instruments onboard the DSC. Further work is required on establishing if the XEUS metrology system is capable of functioning for a 500m focal length or whether an original system is required.
- **Propulsion** - The propulsion of the OSC will be carried out using the AOCS system.
- **Thermal control** - Thermal gradients could pose a problem to the spacecraft through warping, causing misalignments in the crystal lens. To prevent this, the lens will be covered in multilayer insulation (MLI). This will not affect the crystal lens performance, as the thin aluminium of the MLI will not attenuate the high-energy photons. A thermal analysis is required, but it is expected that using MLI will prevent any significant gradients and warping effects.
- **Communication** - The optic spacecraft will only store and transmit housekeeping data, meaning that only low gain antennae are required on the OSC.
- **Data Handling** – This will be sized for housekeeping data only. No science data is collected on the OSC.
- **Power** – The power requirements are low on the OSC due to standard subsystems used. GaAs triple junction solar cells will be used where possible, with silicon cells also an option. Zero eclipse period allows any batteries to be very small.
- **Mechanisms** – A deployment mechanism is necessary for the crystal lens. It is expected that a simple, low risk spring-hinge mechanism could be used for this purpose.

Direction	Attitude Requirement
Longitudinal Direction	± 1 m
Lateral Direction	± 8.5 cm
Angle Error	± 1 arcminute

Table 8.3 Formation flying attitude requirements for the GRL Soyuz Fregat mission

Table 8.3, showing the formation flying requirements for this mission, quotes three errors. The longitudinal direction refers to motion along the line-of-sight axis between the two spacecraft. The angles involved with the Laue optics, being extremely small, result in a relatively large

longitudinal error allowance between the two spacecraft. Sensitivity will decrease, however, as the PSF size increases on the detector, meaning the longitudinal error should be kept minimal.

Perfect formation flying will result when the line of sight of the DSC, and line-of-sight of the OSC coincide with each other. The lateral direction refers to the motion of the DSC line-of-sight drifting away from the OSC line-of-sight yet remaining parallel to it. This is governed by the size of detector.

The angle error value, as the name suggests, refers to the maximum angle that the DSC line-of-sight and the OSC line-of-sight can diverge before the focal spot is lost.

8.2.3 System Budgets

For the purpose of sizing the mission and establishing preliminary system budgets, however, it is necessary to assume some values for the subsystems. There are many similar spacecraft that can be used for preliminary estimates of mass and power budgets. Table 8.4 shows a list of subsystems, the spacecraft each subsystem was based on, and the reason for this decision. The subsystem values used to estimate the GRL system budgets were scaled to reflect the GRL size.

Subsystems	Spacecraft	Reasoning
<ul style="list-style-type: none"> • AOCS (Hydrazine thrusters, 3 axis stabilised) • Thermal control (passive) • Power • Communications • Data handling • Metrology 	XEUS	The mission architecture of XEUS is extremely similar to the GRL. As XEUS is also at L2, the subsystems for XEUS are chosen specifically for this environment. As such, many of the XEUS subsystems can be scaled for GRL preliminary budgeting.
<ul style="list-style-type: none"> • Structure • Harness 	Eddington	The XEUS structure and harness is very mission specific and was therefore not transferable to the GRL. Eddington, also an L2 mission, was more akin to the GRL in size and, therefore, these subsystems were based on Eddington.
<ul style="list-style-type: none"> • Payload 	Gamma Ray Lens	The GRL payload – the crystal lens – is specific to this mission and was not, therefore, taken from any other.

Table 8.4 Table summarising the source and reasoning behind the system budget values

The preliminary mass and power budgets for the OSC are shown in table 8.5 and 8.6 respectfully.

System	Mass (kg)	Margin (%)	Total Mass inc. Margin (kg)
Communication	20	10	22
Data Handling	10	20	12
AOCS	30	5	32
Propulsion	17	5	18
Power	50	10	55
Metrology	1	10	2
Harness	30	20	36
Instruments	849	5	892
Structure	300	20	360
Thermal	25	20	30
Mechanisms	25	20	30
Pyrotechnics	5	20	6
Adapter	-	-	50
Dry mass	-	-	1545
System Margin	-	20	309
Total Dry Mass + Margin	-	-	1854
Propellant	-	100	110
Total OSC mass	-	-	1964

Launcher Capability (kg)	2050
Available Mass (kg)	86

Table 8.5 System level mass budget for the OSC (Soyuz Fregat 2-1b mission)

System	Power inc. 20% Margin (W)
Communication	87
Data Handling	30
AOCS	74
Power	16
Metrology	0
Instruments	0
Structure	0
Thermal	30
Mechanisms*	0
System Margin	20 %
Total Dry Power + Margin	284 W

Table 8.6 Preliminary power budget for the OSC. *A simple spring-lock mechanism is assumed for deployment.

The final expected mass of the OSC is 1964 kg, within the 2050 kg direct insertion limit. However, this also shows that two separate launchers are likely required, with the detector spacecraft carried on a second Soyuz Fregat launcher to L2.

8.3 Detector Spacecraft (DSC)

8.3.1 Payload

The payload of the detector spacecraft is an array of ~ 64 small Ge detectors (pixels), each detector 3 cm x 3 cm x 3 cm, covering an area of $\sim 570 \text{ cm}^2$. The size of the detectors are larger than those used in CLAIRE (1 cm x 1 cm x 4 cm), yet smaller than those used on INTEGRAL (6 cm diameter hexagons, 7 cm thick), reflecting the size of the PSF on the focal plane. The 1σ PSF is a circle ~ 7.6 cm in diameter, therefore hitting ~ 9 detectors on the focal plane. Pixellation of the detector aids background rejection in two main ways. Firstly, the size of the detector is chosen to minimise the active size of the focal plane, reducing background counts. Any photons detected outside of the PSF on the focal plane can then be discounted as background. Secondly, a detector outside of the PSF can be used to simultaneously measure background counts while other detectors observe the PSF from a gamma ray source. The simultaneous background observation will aid background rejection.

A smaller focal plane detector would result in more stringent formation flying, since the size of the focal plane is used to derive the spacecraft formation requirements. The large overall area of the focal plane instrument, $\sim 570 \text{ cm}^2$, allows the formation flying of the spacecraft to be relaxed, particularly in the lateral direction (table 8.3). If the formation flying requirements are determined to be too difficult to achieve, it is possible to change the size of the focal plane to account for this, provided an array of detectors, or pixels, is used. A large number of detectors also allows for detector failure, providing a high level of payload redundancy.

An anticoincidence system such as the BGO shield used on INTEGRAL SPI is also expected to be incorporated in the payload design, allowing for a similar level of background rejection.

8.3.2 Subsystems

An in-depth study into the various spacecraft subsystems for the Soyuz Fregat-sized GRL mission was not undertaken at this stage. However, for the purpose of establishing preliminary budgets, the various spacecraft subsystems are briefly considered below.

- **AOCS** – As with the OSC, the DSC will have a classical three-axis stabilised AOCS control system. Hydrazine thrusters will be used..
- **Metrology** – The active part of the optical metrology system will be based on the DSC – for example, the lasers as used in XEUS for the Laser Rangefinder and Dual λ Interferometer [2]. Once again it should be noted that further work is required in order to establish whether the XEUS system is scalable to the 500m GRL focal length. If this is not possible, another type of metrology system would be required.
- **Propulsion** - The propulsion of the DSC will, again, be carried out using the AOCS system. No insertion Δv is required, allowing the AOCS thrusters to perform the required manoeuvres.
- **Thermal control** – The thermal control system is expected to be passive for the DSC, except for the payload which will require cooling to $\sim 80\text{K}$ by a cryo-cooler. Depending on the position of the cryogenics in the spacecraft, it may be necessary to use heat pipes to transport heat to radiators. A thermal analysis is required.
- **Communication** - The DSC will transmit both housekeeping and science data. For this reason, a medium gain antenna will be used in order to transmit data to Earth. It is still expected, however, that science data rates will be small due to the low numbers of photons associated with gamma ray astronomy, housekeeping data dominating the data transmission. This is yet to be determined.
- **Data Handling** – This will be sized for both housekeeping and science data. The memory size of the data handling system will depend greatly on the ground station coverage of the mission, but is not likely to be a mission driver due to the low expected data volume.
- **Power** – The power requirements are low on the DSC due to standard subsystems used. GaAs triple junction solar cells will be used on two deployed solar arrays. The cryogenic system required for the detector is expected to require low power (30 W) due to advances in cryogenic systems.
- **Mechanisms** – A standard deployment mechanism will be required to deploy the two solar panels.

8.3.3 Systems Budget

Table 8.7 and 8.8 show the preliminary mass and power budget for the Soyuz Fregat-sized DSC. The values used for the budgets have been scaled from the XEUS and Eddington missions, or roughly calculated for the GRL.

System	Mass (kg)	Margin (%)	Total Mass inc. Margin (kg)
Communication	25	10	28
Data Handling	20	20	24
AOCS	25	5	26
Propulsion	17	5	18
Power	35	10	39
Metrology	40	10	44
Harness	20	20	24
Instruments	180	20	216
Structure	190	20	228
Thermal	25	20	30
Mechanisms	5	20	6
Pyrotechnics	5	20	6
Adapter	-	-	50
Dry mass	-	-	738
System Margin	-	20	148
Total Dry Mass + Margin	-	-	886
Propellant	-	100	300
Total DSC mass	-	-	1186

Launcher Capability (kg)	2300
Available Mass (kg)	1114

Table 8.7 Preliminary mass budget for the DSC (Soyuz Fregat 2-1b mission)

System	Power inc. 20% Margin (W)
Communication	87
Data Handling	31
AOCS	49
Power	19
Metrology	65
Instruments	150
Structure	0
Thermal	100
Mechanisms	0
System Margin	20 %
Total Dry Power + Margin	601 W

Table 8.8 Preliminary power budget for the DSC

From the DSC mass budget, it is evident that the mass of the spacecraft, 1186 kg, is well within the 2300kg payload capacity of a Soyuz Fregat to L2 using a HEO injection.

8.4 Mission Configuration

The two spacecraft will be launched in two separate Soyuz-2.1b Fregat launchers from Kourou in French Guyana. First, the OSC will be launched and, as outlined in 8.1.1, will be injected directly to L2. The spacecraft will deploy the lens as soon as the final mid-course corrections are made, in order to minimise the risk of mechanism failure due to the environment during cruise.

The DSC will be launched via HEO using an additional propulsion module as outlined in 8.1.2. HEO is used in order to avoid the strict launch window requirements on a second direct launch. As a result of using the additional propulsion module, the payload capability is also increased to 2300 kg.

In order to establish formation, the two spacecraft will fly within a few kilometres using RF metrology and, using the optical metrology systems, establish a locked formation flying distance of 436m.

Observations will last for 14-30 days, the spacecraft re-pointing after each observation to the next target. Re-pointing is performed by the OSC turning on it's centre of mass and the DSC maintaining the formation lock by moving in a arc as well as turning on it's centre of mass. If a SNe Ia is reported during an observation, it may be necessary to pause the observation in favour of the new SNe Ia target. This is in order to follow the light curve evolution as outlined in

section 2.1.1. Breaks in the observation of many source types are acceptable and can be continued at a later time.

8.4.1 Effective Area

The result of the effective area analysis of the Soyuz Fregat-size Laue lens is shown in figure 8.1. The figure also compares the effective area of the GRL to the MAX mission. Table 8.9 outlines the parameters input into the model (section 3.3.2).

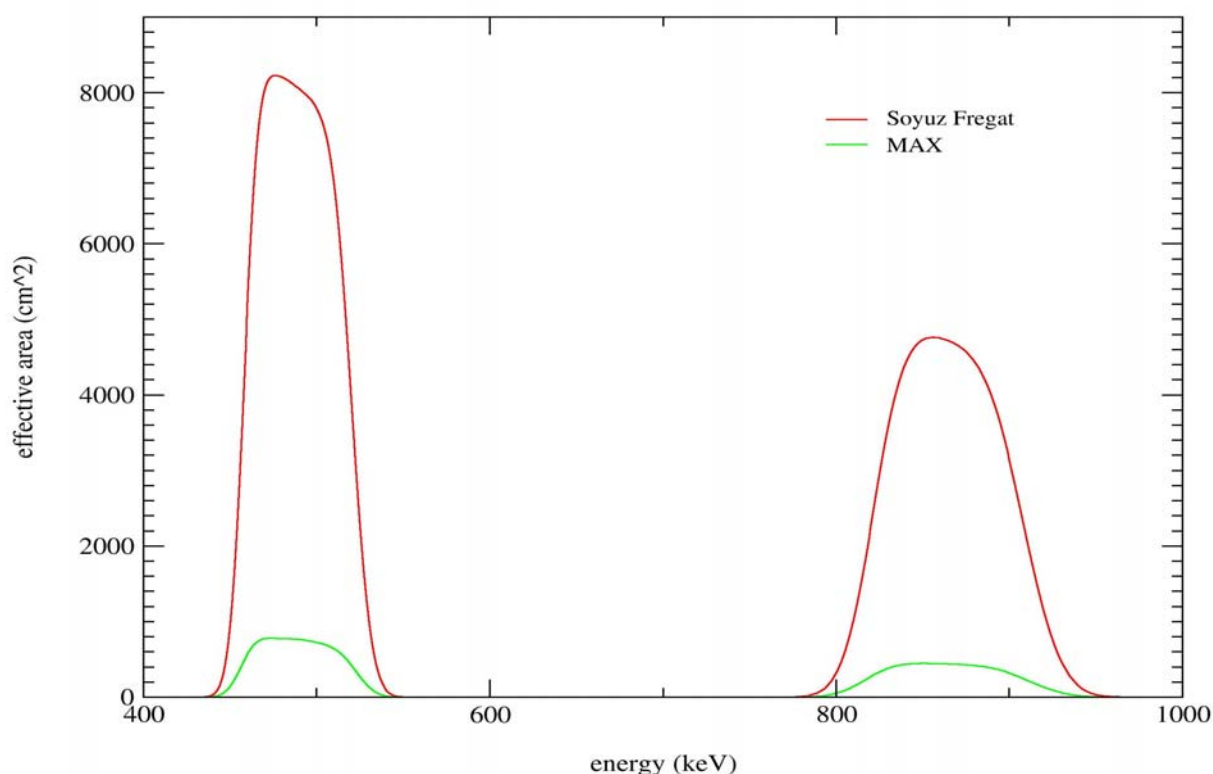


Fig. 8.1 Laue Lens effective area analysis of the Soyuz Fregat configurations. The MAX effective area is also shown here for comparison.

Configuration	f [m]	Ge in [cm]	Ge out [cm]	Cu in [cm]	Cu out [cm]
MAX	133	97	110	87	96
Soyuz Fregat	436	318	360	285	314

Table 8.9 Parameters input into the effective area model to establish the effective area of the MAX and Soyuz Fregat configurations

8.4.2 Sensitivity Analysis

The sensitivity model was used to establish the sensitivity of the Soyuz configuration. The results of this analysis are shown in figure 8.2. Tables 5.1 and 8.9 outline the parameters used to conduct the sensitivity analysis. The curves for the MAX mission are included here for comparison.

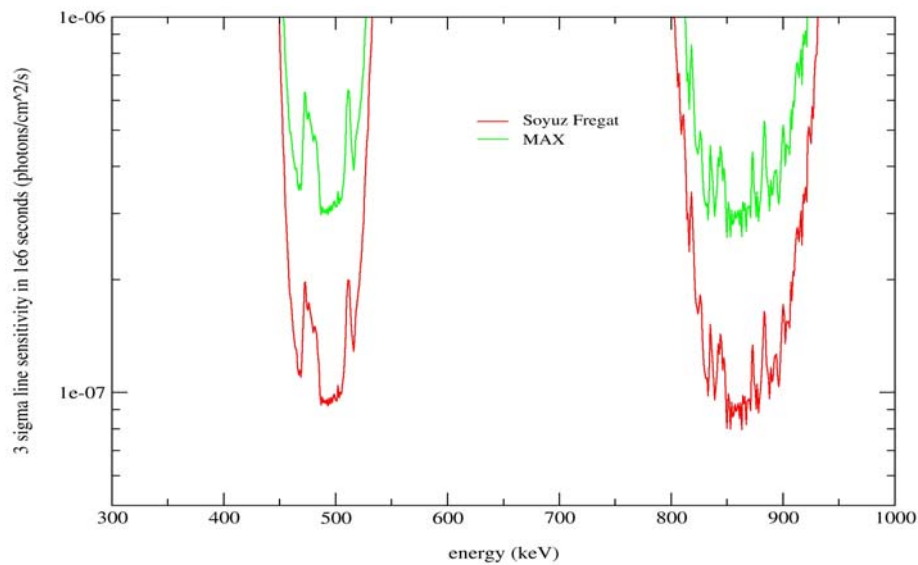


Figure 8.2 The 3σ line sensitivity for the Soyuz 2-1b GRL configuration. The MAX configuration is included for comparison.

8.5 Soyuz Fregat Mission Conclusions

It can be seen from figure 8.2 that the sensitivity of the Soyuz Fregat GRL configuration results in a sensitivity of $\sim 1\text{--}2 \times 10^{-7} \text{ ph.cm}^{-2}\text{s}^{-1}$ in the two energy bands of interest. It can be seen from figure 8.3 that this provides approximately two orders of magnitude improvement on SPI INTEGRAL ($\sim 1\text{--}4 \times 10^{-5} \text{ ph.cm}^{-2}\text{s}^{-1}$), even without further improvement in background rejection.

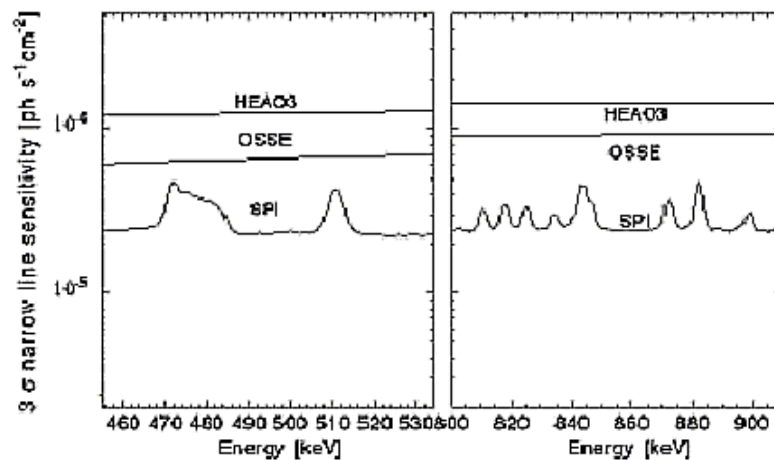


Fig. 8.3 3 σ line sensitivity of SPI INTEGRAL and other previous high-energy astrophysics missions

As stated in section 2.2, a sensitivity of a few $\times 10^{-7} \text{ ph.cm}^{-2}\text{s}^{-1}$ is the minimum requirement for the GRL. This is achieved according to the sensitivity analysis presented here. However, the desired $10^{-8} \text{ ph.cm}^{-2}\text{s}^{-1}$ is not achievable with this configuration. A greater effective area and/or increased background rejection will be required to achieve this.

Another drawback to this configuration is the inability to observe the lower energy band of interest, 50-300 keV. The prohibitive mass restriction of the dual launch results in this energy band being omitted from this configuration. The dual launch scenario introduces many difficulties in the mission, primarily in the rendezvous between the two spacecraft at L2 requiring a HEO insertion. There is an increased risk factor as a result of two successful launches being required in order to result in a successful mission. The cost of two Soyuz Fregat launches from Kourou is also expected to be comparable to a single Ariane 5 launch. In-depth cost analysis of this scenario was beyond the scope of this TRS, however initial estimates suggest that a mission of this size, complexity and technology requirement is highly unlikely to cost less than 500 million euros.

The prospect of a major increased payload mass, a greater scientific return and a more attractive launch profile from a simplicity and programmatics point of view, results in the Soyuz Fregat profile to be initially discounted as the GRL baseline mission. A larger Ariane 5 configuration will now be investigated in section 9.

8.6 References

- [1] A comparative study of possible future nuclear astrophysics missions, M. Beijersbergen, Cosine Report, CSC-ODS-TN5, 2004
- [2] XEUS CDF Study Report, CDF-31(A) October 2004
- [3] Spacecraft Systems Engineering 2nd Edition, P. Fortescue & J. Stark, John Wiley & Sons, 1998
- [4] SMAD III, J. R Wertz & W. J. Larson, Microcosm Press, 1999

9. Mission Profile 2 – Ariane 5

Section 8.1 introduced a launch scenario consisting of two separate Soyuz Fregat launches which, due to complexity and sensitivity analysis results, has been discounted as the baseline configuration for the GRL. The use of the Ariane 5 launcher to launch the GRL to L2 will allow a greatly increased payload mass, while also providing an increase in fairing volume. The result of this is the ability to perform a single launch carrying both spacecraft to L2. In addition, a second payload – a silicon pore multilayer optic - is introduced to the optic spacecraft, significantly increasing the energy bandwidth and, hence, scientific capability of the mission.

9.1 Single launch Mission Analysis

This section will consider the mission analysis of a single Ariane 5 launch to L2 with an increased payload mass. It is important to note that the difference between the single and dual launch scenarios are in the launcher and resultant payload capability increase. The details of the launch path and final orbit remain the same as those discussed in section 7 and 8.1, as baselined for the Soyuz Fregat dual launch.

9.1.1 Direct Launch

A single, direct launch using the Ariane 5 ECA is capable of placing 6800 kg into Halo orbit at L2 [1]. As stated previously, once the Halo orbit is established, small manoeuvres can be used to remove the unstable part of the orbital motion. A direct launch benefits from simplicity, as well as a basic launcher cost, as no additional stages are required. The gravity loss from such a launch is also minimal. No dedicated upper-stage propulsion module is required. Again, as with the Soyuz Fregat, a single launch results in a launch window of two ten-week periods per year (see section 8.1.3).

9.1.2 HEO Launch

An additional propulsion unit can be added to the launcher in order to increase the spacecraft performance to L2 via a HEO. The launcher can inject the spacecraft into a lower energy HEO and, after separation from the launcher, the spacecraft itself completes the velocity increment to reach parabolic speed. As with the Soyuz Fregat, the HEO launch can be used to extend the launch window if necessary (section 8.1.2).

The selection of the optimum HEO apogee height is the result of an optimisation taking launch performance, gravity loss and spacecraft propulsion unit characteristics such as mass and specific impulse into account.

Two options are available for a HEO using the Ariane 5 ECA, depending on the type of propulsion module used.

- **A solid propellant stage** – For example, the largest stage of the Thiokol Star family: the Star 75 provides a substantial increase in payload mass to L2. It is expected that the optimum HEO orbit will result in a payload capacity of 7600 kg.
- **A bi-propellant stage** – The only bi-propellant stage available in Europe for integration into a spacecraft has a current thrust of 400N that, by the expected launch time of the GRL can be assumed to be 500N. A very large gravity loss is expected from launching such a large mass. Performing the manoeuvre in several steps, however, can reduce the effect of gravity loss and can result in a performance of 7400 kg to L2.

See Table 8.1 for the trade-off between direct and HEO launches as seen in XEUS CDF study conducted in October 2004 [1].

9.1.3 Launch Profile Conclusion

The GRL will baseline a single, direct launch to L2 using an Ariane 5 ECA. A HEO launch profile will only be used if a much greater mass performance is required. The direct launch has a large launch window that should be adequate for the GRL and, for this reason, is unlikely to require a HEO launch in order to extend the launch window further. The single Ariane 5 launch has the great advantage of no rendezvous manoeuvre required between the two spacecraft while providing a vastly improved payload capability to L2 over smaller launchers such as the Soyuz Fregat 2-1b.

9.2 GRL Optics Spacecraft (OSC)

9.2.1 OSC Configuration

The design of the OSC was driven by a number of key factors. Primarily, the configuration was lead by the Laue lens being a ring of very large diameter. The extremely large mass of the crystal lens was also a driving factor behind the design. The ring shape, and the necessity of deployment of the lens, led naturally to a cylindrical bus. The silicon pore optic instrument also has to be unobstructed and is, therefore, held in the centre of the bus with no obstruction in front or behind. Figure 9.1 shows the current baseline configuration for the OSC.

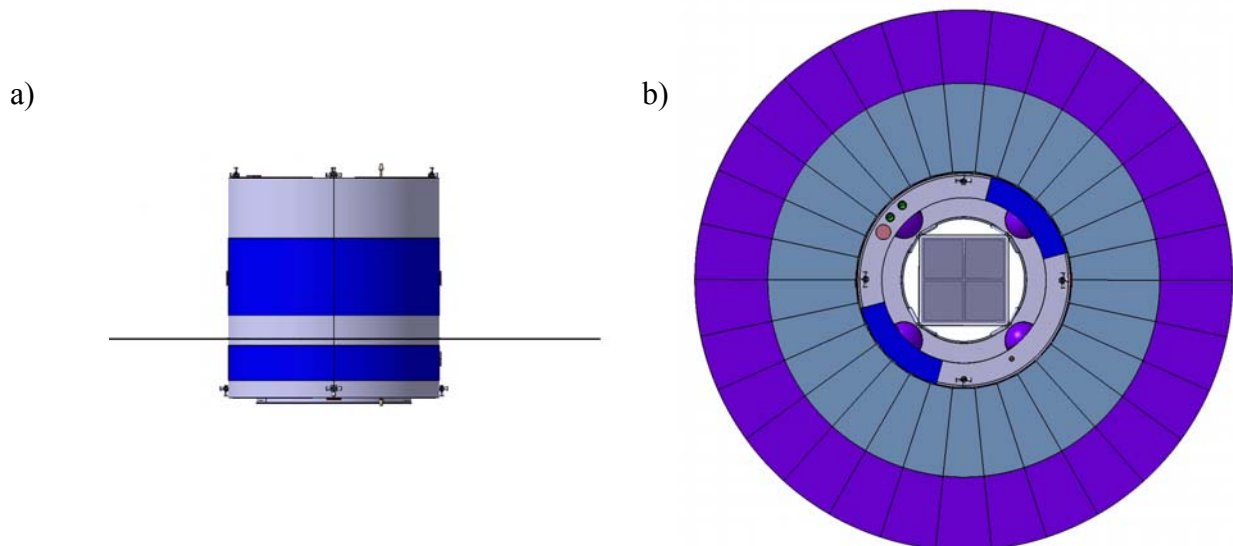


Fig 9.1 Figure showing the baseline configuration of the deployed optic spacecraft. a) OSC side view b) OSC front view. To scale.

When stowed during launch, the petals, which house the very large mass of Ge and Cu crystals, have to be supported sufficiently to survive launch. Figure 9.2 shows the stowed configuration of the OSC. It can be seen that the height of the OSC is governed by the lens diameter, allowing the petals to be secured to the spacecraft in the region of greatest mass. Two stiffening rings will be used within the spacecraft to aid the structural integrity of the bus during launch while supporting the lens petals.

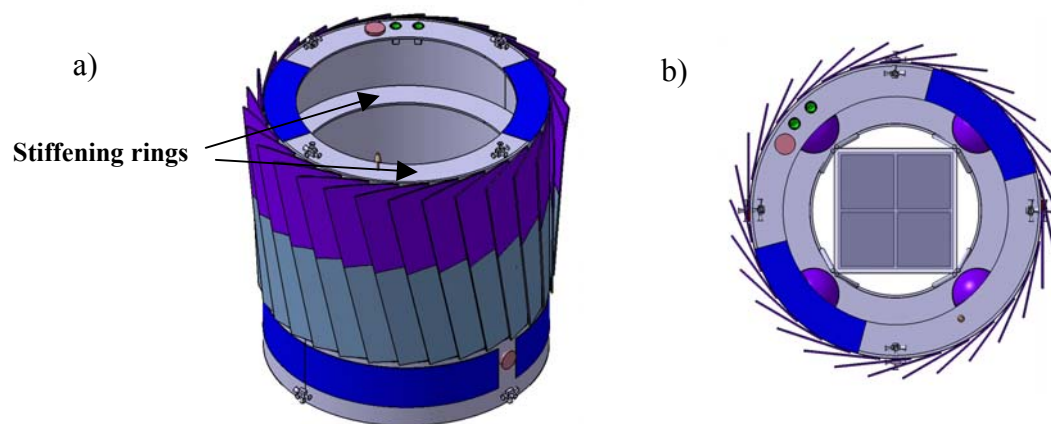


Fig 9.2 OSC stowed configuration. a) Side view and b) top view.

The petals, when stowed, are all angled (fig 9.2 b) in such a way that when opened by the mechanism they turn and lock in the deployed crystal ring without coming into contact with each other, as seen in figure 9.3. It is crucial that the deployment mechanism aligns the crystals precisely in order to minimise the contribution of the petal misalignment to the overall error in crystal orientation (See appendix C). The alignment of the petals is required to be in the order of half an arc minute, comparable to the mosaicity of the crystals.

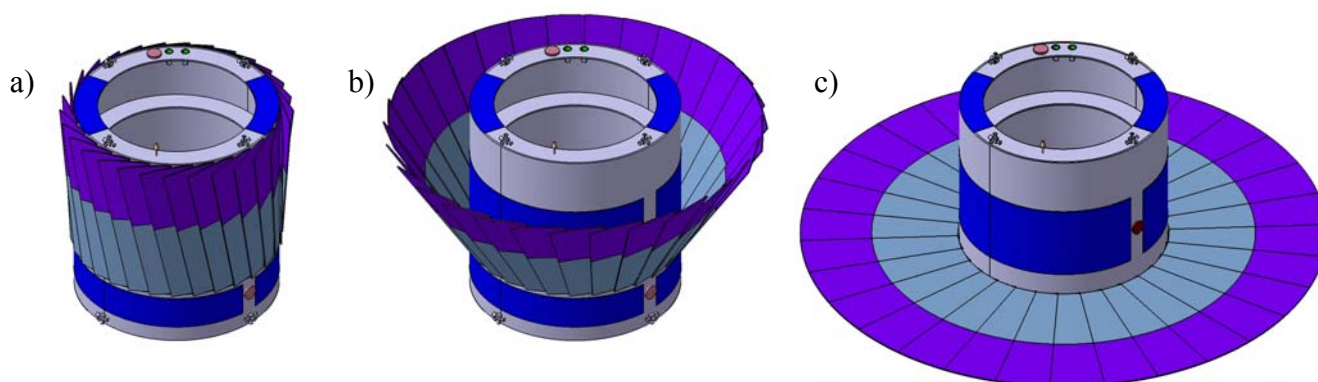


Fig 9.3 The deployment of the Laue Lens optic. a) Stowed configuration, b) semi-deployed configuration and c) the fully deployed lens.

The main OSC dimensions are shown in figure 9.4. When stowed the OSC fits comfortably into the Ariane 5 fairing [4] (see section 9.4).

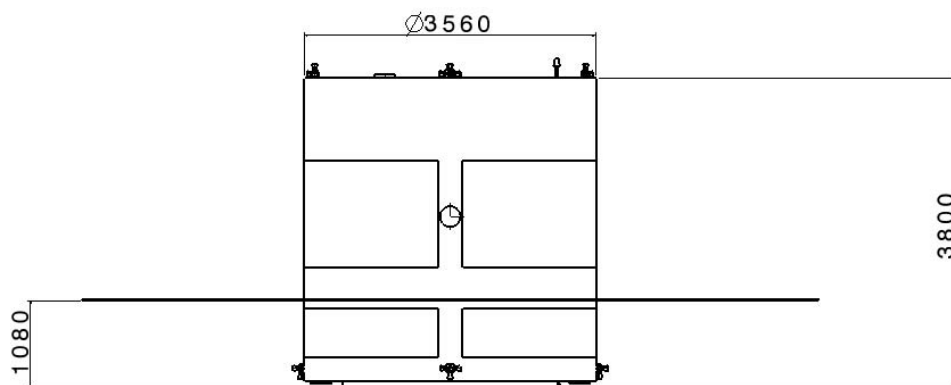


Fig. 9.4 OSC Dimensions

The diameter of the cylindrical bus is driven by the Ariane 5 2624 launcher adapter and the load path of the stacked configuration (see section 9.4.1). The DSC diameter is also driven by these requirements. The thrusters were positioned on the spacecraft to allow for full, three-axis stabilisation and transverse motion. Star trackers and sun sensors are also placed around the craft to provide attitude measurements, while the antennae on the craft provide omni-directional communication capability. Table 9.1 summarises the key configuration design drivers for the OSC.

Configuration Driver	Action
Circular lens, large diameter	<ul style="list-style-type: none"> Novel deployment mechanism Long, cylindrical spacecraft bus
Large mass concentration on the lens ring	<ul style="list-style-type: none"> Support rings used before deployment during launch
Temperature gradient/misalignment control of the optics	<ul style="list-style-type: none"> MLI coating on the Laue lens and Silicon Pore Optic
Unobstructed Silicon Pore Optic	<ul style="list-style-type: none"> Bus is a cylindrical ring with the SiPO supported inside
30° sun angle restriction during observation	<ul style="list-style-type: none"> GaAs and Si solar panels providing adequate power in all orientations Omni-directional communication capability
2624 Ariane 5 adapter	<ul style="list-style-type: none"> Diameter of bus to accommodate this.

Table 9.1 A summary of key configuration design drivers for the OSC

9.2.2 Payload

The larger launch performance of the Ariane 5 ECA allows the inclusion of a multilayer mirror silicon pore optic as a payload, as well as an increased area Laue crystal lens. This section considers the two GRL payloads as baselined for the larger Ariane 5 launcher mission.

9.2.2.1 The Laue Lens

The primary payload on the OSC is the Laue crystal lens. Using the effective area model (section 3.3.2) a lens suited to the fairing size and mass capability of an Ariane 5 was designed. The lens was optimised for two energy bands; 425-522 keV using the (111) plane of Germanium and 825-910 keV using the (111) plane of Copper. Note that the lower energy band has been extended to an even lower energy of 425 keV. This is for two reasons. Firstly, increasing the bang gap of the lens allows the potential for a larger portion of the continuum to be seen in a region of many nuclear lines. These lines can be redshifted and broadened to lower energies so extending the band downwards is advantageous. Secondly, and perhaps more importantly, as the focal length of the lens is set by the energy observed by the outer diameter of the lens, observing a lower energy results in a shorter focal length and, in turn, increases sensitivity as the point spread function incident on the detector becomes smaller.

Table 9.2 outlines the main characteristics of the lens.

Material	Germanium	Copper
Energy Band	425-522 keV	825-910 keV
Inner Radius	3.66 m	3.29 m
Outer Radius	4.5 m	3.63 m
No. of rings	85	35
Volume of each crystal	1cm ³	1cm ³
No. of crystals (Packing factor = 0.85)	184988	64582
Mass	1034 kg	605 kg
Focal length	504 m	504 m

Number of lens petals	30
Mass of crystals per petal	54.6 kg

Table 9.2 Main characteristics of the Laue gamma-ray lens, designed for an Ariane 5. See appendix G for a more detailed mass breakdown of the Laue lens crystals and structure.

Again, the lens diameter is larger than the Ariane 5 fairing (4.57m internal diameter), once again leading to the use of a deployment mechanism for the lens. A packing factor of 85% is also assumed, along with a 5% system margin for the crystal mass estimate. The lens is constructed

of 30 deployable petals, each petal holding a segment of the complete lens ring (fig. 9.5 - the purple region), containing copper and germanium crystals with a mass of 54.6 kg. Figure 9.6 shows the position of the Laue lens and silicon pore multilayer optics (section 9.2.1.2).

Note, also, that in order to minimise warping of the Laue lens due to temperature gradients, the crystals are covered in multilayer insulation (MLI).

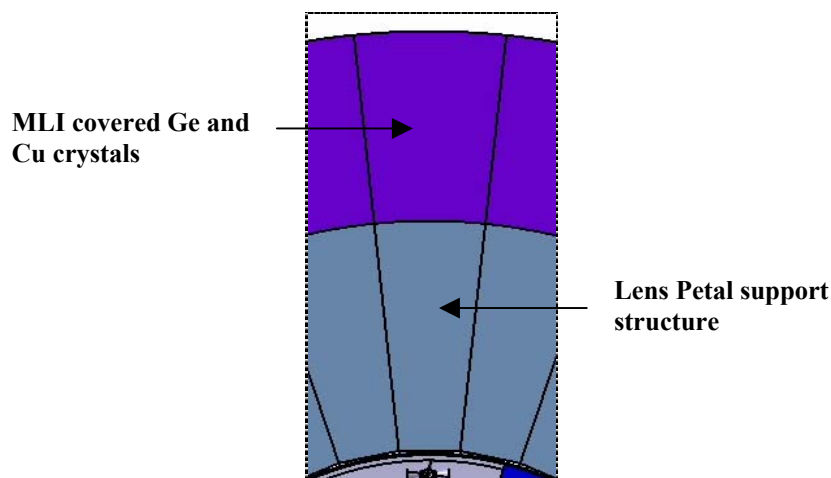


Fig. 9.5 Close-up picture of a lens Petal.

9.2.2.2 The Silicon Pore Multilayer Optic

The science driver behind the addition of the silicon pore optic as a second payload to the OSC is the Compton backscattering of the 511 keV annihilation line. The added mass capability available to the GRL from the use of the Ariane 5 launcher allows this incorporation of an additional payload.

The Compton backscattering effect has been observed (Leventhal & MacCallum 1980; Matteson et al. 1991) and accompanies the 511 keV emission from compact objects. Compton scattering will occur from accreting sources such as black holes.

The result of this Compton scattering is a series of line-like features which appear in the continuum at ~170 keV for single backscattering, ~102 keV for double backscattering and ~74 keV for triple backscattering. This leads to three potential energy-band possibilities;

- An optic optimised for the three energy bands around the Compton backscatter features: ~50 keV – 200 keV

- An optic for the two strongest Compton features: $\sim 70 - 200$ keV
- An optic optimised for the single backscatter event: $\sim 140-200$ keV

It is expected that the efficiency of a multilayer optic at these energies will be greater than the efficiency of a Laue crystals [2]. Also, as the central region of the crystal ring is empty, and in Laue diffraction it is the higher energies that are focused from smaller radii, it is concluded to use silicon pore multilayer optics for this purpose, utilising the free central area of the OSC.

The silicon pore optics will be developed for the XEUS mission, leaving the main driver behind this payload to be the development and design of an efficient multilayer coating. As seen in

section 3.1.2 a multilayer coating can be optimised for a certain energy band. It is necessary, therefore, to know the response of the multilayers for all three possible energy bands above in order to complete a trade-off between them. In order to complete this tradeoff, the following parameters need investigation (for both imaging [Wolter I] and non-imaging [conic] cases).

- The effective area of the Multilayer Mirrors at the stated energies.
- The expected angular resolution and field of view of the mirrors, given the focal length, energy and size of mirror. The focal length is set to 504 m to coincide with the focal point of the Laue lens.
- The efficiency of the mirrors at the given energies.

In order to achieve a complete investigation of the 511 keV annihilation line, we assume that the payload will investigate all three Compton backscatter features in the 50-200 keV region. An area of 2.25 m^2 is available within the Laue lens ring for this payload (figure 9.6). This is equivalent to approximately 4 of the XEUS mirror petals (fig 3.5d).

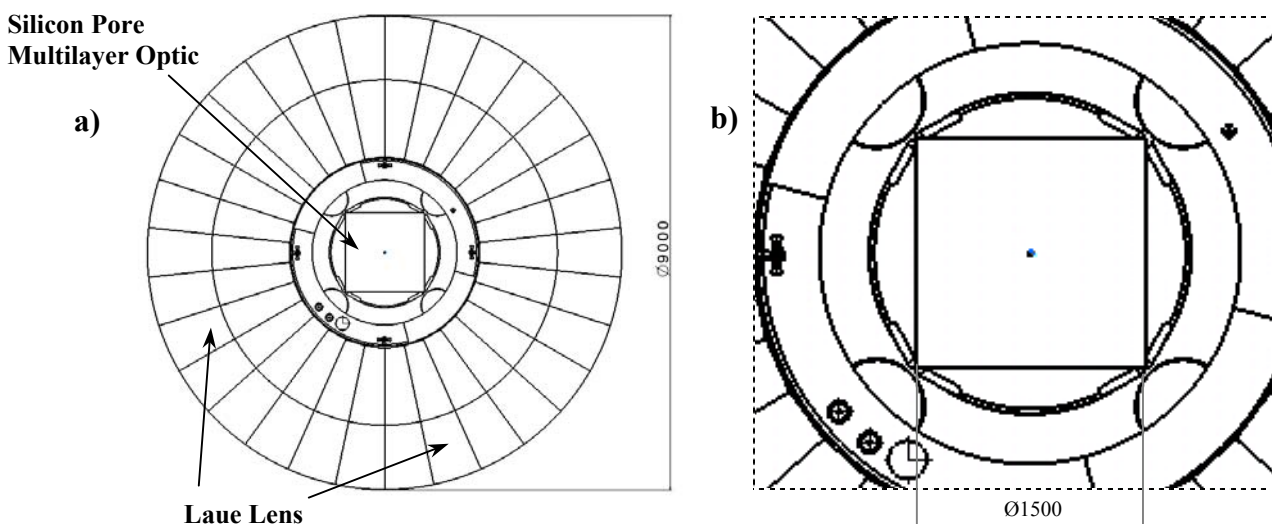


Fig 9.6 The payload positions on the GRL optic spacecraft; a) OSC head-on along the line of sight axis, b) Close-up of the silicon pore multilayer optic.

In the XEUS CFD study [3] it was noted that a key mission driver is the temperature gradient across the X-ray mirrors. Large gradients are unacceptable as they cause the mirror to warp. The GRL is at an advantage over XEUS in that the energies of interest are much higher. To prevent large thermal gradients across the mirror, multilayer insulation is used to conceal the optic. An in-depth thermal analysis of this is required to establish if covering the optic with MLI is sufficient to passively maintain a low temperature gradient across the mirror. The MLI coating will also prevent mirror contamination from the hydrazine propellant used – an issue that has lead the XEUS mission to use a cold gas system.

9.2.3 Subsystems

- **AOCS** – The spacecraft will have a classical AOCS control system as proposed in the XEUS CDF studies. Hydrazine thrusters can be used, as the risk of contaminating the Laue lens is negligible due to the high-energy photons that will be of interest and the multilayer insulation encasing the silicon pore optic. Any residue deposited on the optics from the thrusters should not affect the performance.

The AOCS system on the OSC will utilise course and fine sun sensors, star trackers and a gyroscope, as well as a set of reaction wheels to measure and control the spacecraft attitude.

Table 9.3 shows the stability requirements of the Ariane 5 scenario GRL.

- **Metrology** – The metrology system, again based on XEUS, will have three main subsystems; 1) Coarse RF metrology, 2) Fine RF metrology and 3) Optical metrology. The MAX mission also utilises a similar metrology system. Further investigation is required to determine if the system proposed for the XEUS mission, which flies with a focal length of ~50m, is applicable to the GRL with a significantly larger focal length.
- **Propulsion** - The propulsion of the OSC will be carried out using the AOCS system. This is as a result of the zero insertion Δv required for the halo orbits (section 7.2.2). The OSC will carry approximately 210 kg of propellant. This value is based on an estimated number of observations over the mission lifetime, re-pointings, slews, station keeping and momentum dumping.
- **Thermal control** - Thermal gradients could pose a problem to the spacecraft through warping, causing misalignments in the crystal lens. To prevent this, the lens will be coated in multilayer insulation (MLI). This will not affect the crystal lens performance, as the thin aluminium of the MLI will not attenuate the high-energy photons. A thermal analysis is required, but it is expected that using MLI will prevent any significant gradients and warping effects. Materials with very similar thermal expansion coefficients will also be used to construct the spacecraft in order to minimise warping effects. The mass driver of the thermal control system will be the multilayer insulation.

The long central cylinder of the spacecraft bus could cause shadowing of the lens at certain observation angles. It has been assumed that any thermal gradients induced by shadowing are minimised by the MLI cover, although this requires more detailed investigation. There are two options to limit shadowing of the lens. Firstly, a more constrained observing angle could be employed. This is very undesirable as a key mission objective is to maximise the observation area of the sky at any one time. Alternatively, a less restrictive configuration for the OSC could be conceived where the length of the cylindrical bus is shortened, reducing/preventing shadowing. In this case, a way of supporting the lens while in the stacked configuration would be required.

The silicon pore optic will be enclosed in a MLI case to minimise thermal gradients. More in-depth thermal analysis will determine if this passive measure is sufficient to maintain the thermal gradient within tolerance levels [3].

- **Structure** – The spacecraft structure is to be designed with controlling thermal gradients and supporting the Laue lens as a priority. Materials with equivalent thermal expansion properties should be used as much as possible throughout the structure to prevent warping and misalignment through thermal gradients. Materials such as aluminium or carbon-reinforced plastics could potentially be used. See table 9.1 for further detail on the structure/configuration design.
- **Communication** - The optic spacecraft will only store and transmit housekeeping data, meaning that only low gain antennae (LGA) are required on the OSC. Earth communication will be conducted using X-band low gain antennae. Antennae will also be required for the RF metrology system – these will be S-band LGA.
- **Data Handling** – This will be sized for housekeeping data only. No science data is collected on the OSC.
- **Power** – The power requirements are low on the OSC due to standard subsystems used. The OSC uses body-mounted solar cells. As the GRL is expected to observe in any direction excluding a 30 degree cone towards the sun, in order to maintain the required power level (table 8.4) $\sim 14 \text{ m}^2$ of Si solar panels are used. 1.2 m^2 of GaAs triple junction cells will be mounted on each end of the spacecraft in order to provide adequate power to the spacecraft when observing directly away from or towards the sun. The reason for using the two different cell types is the inability to body mount GaAs triple junction cells to a curved surface. Zero eclipse period allows any batteries to be very small. Figure 9.7 shows the positioning of solar cells on the OSC.

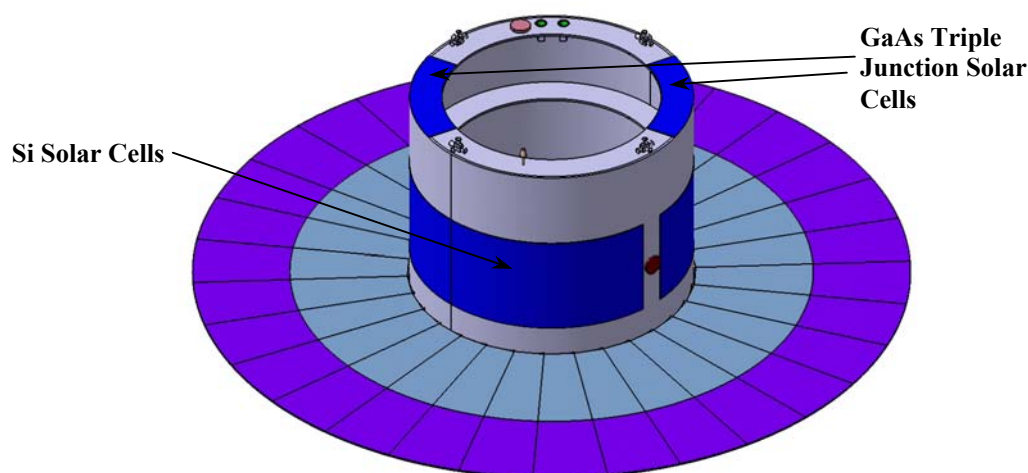


Fig. 9.7 Figure showing the position of Si and GaAs solar cells body-mounted on the OSC

- Mechanisms** – A deployment mechanism is necessary for the crystal lens. It is expected that a simple, low risk spring-hinge mechanism could be used for this purpose. The deployment mechanism requires further investigation.

Direction	Attitude Requirement
Longitudinal Direction	± 1 m
Lateral Direction	± 8.0 cm
Angle Error	± 80 arcseconds

Table 9.3 Formation flying attitude requirements for the GRL Ariane 5 mission

The three errors quoted in table 9.3 are defined in section 8.2.2 and are derived from the formation flying effects on the size and shape of the PSF on the detector. The detector in the DSC (section 9.3.1) is an array of regular hexagons, each with a total area of 405 cm^2 . The 1σ point spread function is $\sim 60 \text{ cm}^2$ in area. The attitude requirements are slightly more stringent due to the larger focal length.

9.2.4 Mass Budget

Table 9.4 shows the preliminary mass budget for the large OSC - Ariane 5 configuration. The maximum dry mass of the spacecraft is 3268 kg including a system margin of 20% (equivalent to 545 kg). For a more in-depth mass budget system breakdown, see Appendix E. The system budgets were considered in greater detail here than in the Soyuz Fregat scenario.

System	Mass (kg)	Margin (%)	Total Mass inc. Margin (kg)
Communication	19	12	21
Data Handling	9	20	11
AOCS	31	5	32
Propulsion	22	5	24
Power	66	10	73
Metrology	1	10	2
Harness	34	20	41
Instruments	1684	5	1774
Structure	485	20	582
Thermal	25	20	30
Mechanisms	25	20	30
Pyrotechnics	5	20	6
Dry mass	-	-	2689
System Margin	-	20	538
Total Dry Mass + Margin	-	-	3227
Adapter	-	-	98
Propellant	-	*	180
Total OSC mass	-	-	3505

*Table 9.4 System level mass budget for the OSC. *The margin on propellant was consistent with the margin philosophy for assessment studies whereby 5% was added to trajectory manoeuvres and 100% for orbit maintenance and attitude control.*

9.2.5 Power Budget

Table 9.5 shows the preliminary power budget for the large OSC - Ariane 5 configuration. The maximum power required by the spacecraft is 284 W. The same power budget was used for the Soyuz Fregat scenario as there is minimal difference made to the power requirements of the spacecraft from the increased payload mass.

System	Power inc. 20% Margin (W)
Communication	87
Data Handling	30
AOCS	74
Power	16
Metrology	0
Instruments	0
Structure	0
Thermal	30
Mechanisms*	0
System Margin	20 %
Total Dry Power + Margin	284 W

*Table 9.5 Preliminary power budget for the OSC. *A simple spring-lock mechanism is assumed for deployment.*

9.3 GRL Detector Spacecraft (DSC)

9.3.1 DSC Configuration

The primary configuration design driver of the DSC was the need to place the OSC on top of the DSC in the stacked configuration (figure 9.8). Placing the detector spacecraft on top of the OSC was not possible due to the Laue Lens mechanism and the ring bus structure. It would have resulted in a large structure mass increase of the OSC bus in order to be capable of supporting the DSC. The DSC had to, therefore, be large and strong enough to support the OSC, which has a much larger mass of ~3478 kg.

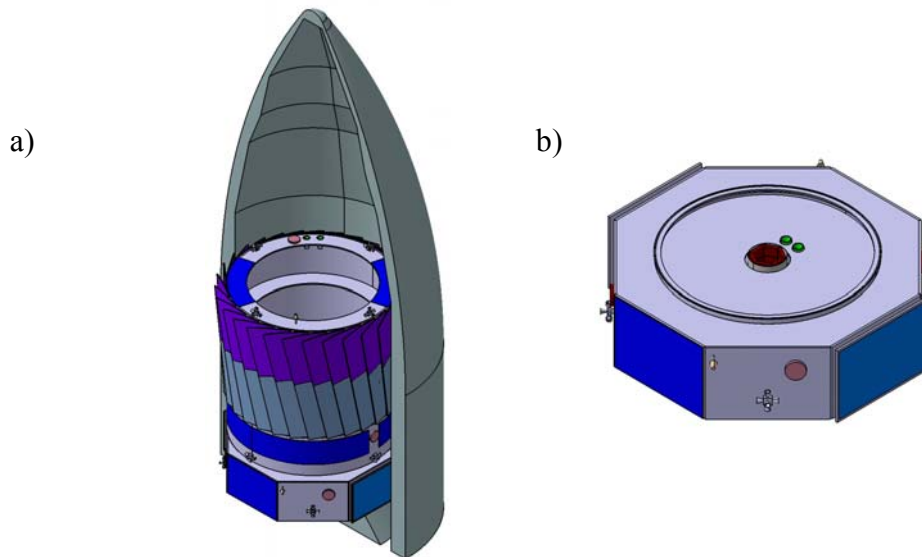


Fig. 9.8a) The spacecraft stack configuration, the OSC on top of the DSC and b) the stowed DSC configuration

As seen in figure 9.9a and b, the detector spacecraft has an internal cylindrical wall within the spacecraft bus. This wall is 2624 cm in diameter, matching the standard launch adapter used in the GRL mission for the Ariane 5 launch. Using this diameter ensures a smooth load path through the OSC and DSC during launch, reducing stresses on the spacecraft. The OSC is also attached to the DSC during launch using a 2624 launch adapter.

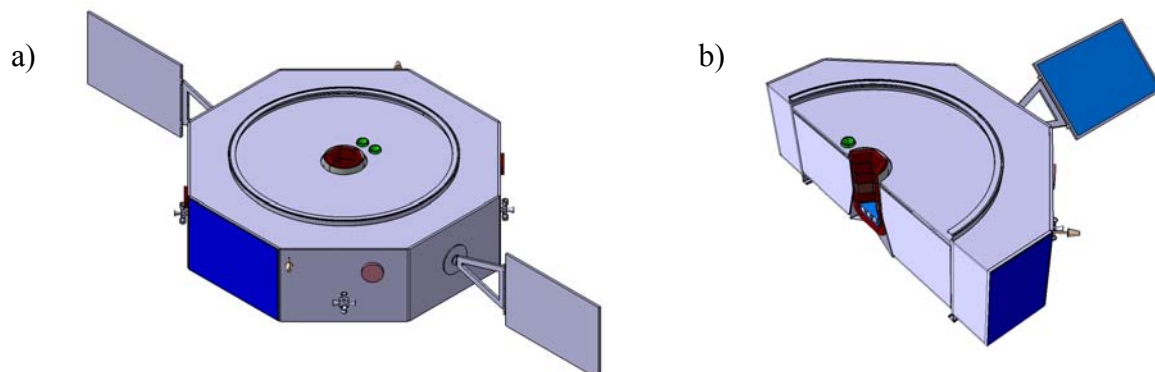


Figure 9.9 The DSC configuration a) fully deployed and b) cut in half displaying the internal cylindrical wall, shear walls and gamma ray spectrometer.

There are also four shear walls cutting the spacecraft into quarters, extending from the detector at the centre of the spacecraft to the outer hexagonal wall. The shear walls provide extra stiffness, as well as flat surfaces to mount the required electronic boxes and instrumentation.

Figure 9.10 outlines the key dimensions of the spacecraft.

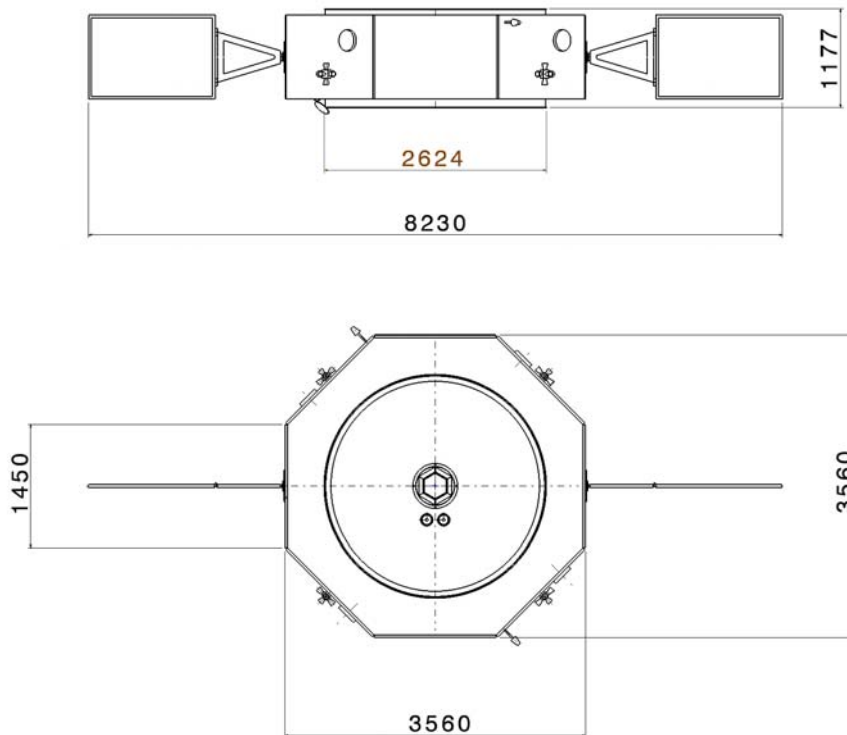


Fig. 9.10 Key dimensions of the DSC

A major mission driver is background rejection. Limiting the background count in the detector is extremely important if sensitivity is to be optimised. The major contribution to the background count is the intrinsic background due to activations within the spacecraft. A great deal of work had been invested in identifying the sources of lines within INTEGRAL's intrinsic background. The GRL should learn from the findings of this research, and aim to design the spacecraft to minimise the line features contributing to the background in the energy bands of interest. Doing this should significantly reduce the background contribution from the spacecraft. For the purpose of this mission baseline, however, we assume the same background rejection as achieved on INTEGRAL SPI, allowing the use of the real SPI background data in the sensitivity analysis.

Another key aspect to the DCS configuration design was the placing of the radiator required to dissipate heat from equipment and, most importantly, from the cryogenic cooler required by the gamma ray spectrometer. One of the spacecraft side walls (coloured blue in figure 9.9a) will act as a radiator and will always see cold space. This will be achieved through turning the spacecraft around the line of sight axis as required. This will not effect the spectrometer results as the orientation of the detector around the line of sight axis is arbitrary.

The thrusters were positioned on the spacecraft to allow for full, three-axis stabilisation and transverse motion. Star trackers and sun sensors are also placed around the craft to provide attitude measurements, while the antennae on the craft provide omni-directional communication capability. A manoeuvrable medium gain antenna is placed on the opposite side to the spectrometer aperture for data transfer to Earth as this side of the craft will be in contact with Earth more often than the other due to a 30 degree sun-angle restraint imposed on the spacecraft.

Configuration Driver	Design Action
Large primary payload detector	<ul style="list-style-type: none"> Height of bus driven by this. Positioned in the centre of the spacecraft.
Below the OSC in the Stack configuration	<ul style="list-style-type: none"> 2624 adapter used to simplify the load path during launch Internal cylindrical wall incorporated to aid load path during launch
Cryogenic system requires heat dissipation	<ul style="list-style-type: none"> Radiator panel positioned on a wall which will continuously face cold space
Data downlink to Earth	<ul style="list-style-type: none"> MGA on a directional boom placed on the opposite side of the spacecraft from the detecture aperture Omidirectional communication

Table 9.6 Summary of the key configuration design drivers for the OSC

9.3.2 Payload

The payload of the DSC is an INTEGRAL SPI-style spectrometer. The focusing optics allows the size of detector to be scaled down, reducing the mass of the spacecraft as well as intrinsic spacecraft background due to activation events. As with the Soyuz Fregat configuration, the Ariane 5 detector uses a Ge pixellated detector array. As with SPI, the GRL array baselined here is made of hexagonal detectors. Each detector is a regular hexagon with an area of 7.8 cm^2 . There are 52 detectors in total, each 3 cm thick. This thickness is optimised for 511 keV as shown in figure 9.11.

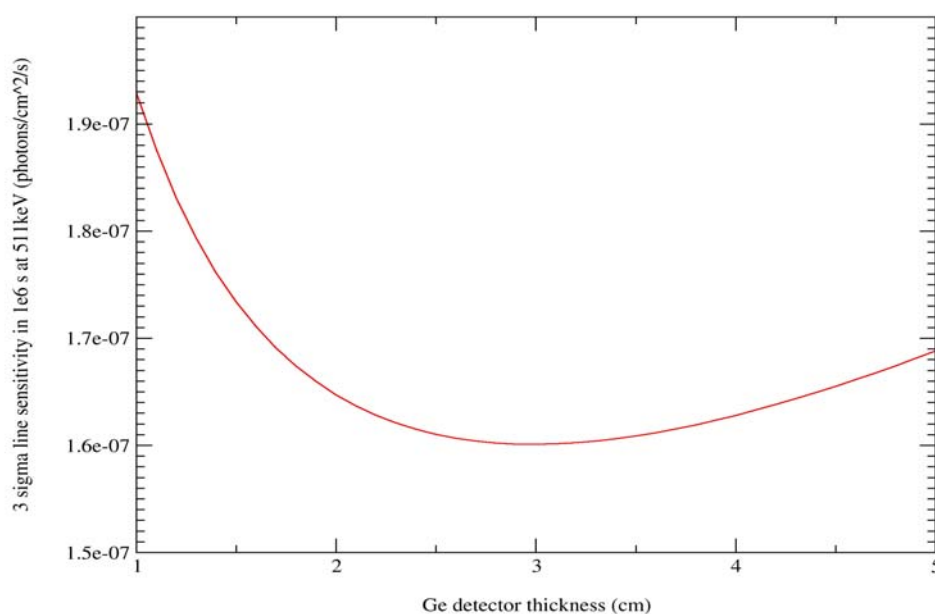


Fig. 9.11 Optimised thickness of Ge for the detection of 511 keV photons

The total detector area is 405 cm^2 . For the Ariane 5 configuration, the 1σ PSF is $\sim 60 \text{ cm}^2$. Table 9.7 reiterates the formation flying requirements for the GRL due to the 1σ PSF size.

Direction	Attitude Requirement
Longitudinal Direction	$\pm 1 \text{ m}$
Lateral Direction	$\pm 8.0 \text{ cm}$
Angle Error	$\pm 80 \text{ arcseconds}$

Table 9.7 Formation flying attitude requirements for the GRL Ariane 5 mission

Figure 9.12 shows the GRL spectrometer setup. The Ge detector array is housed in a cryogenic cold box at the base of the instrument, with the cryogenic ‘cold finger’ extended through the instrument wall to the external radiator. The cryogenic plate cools the Ge crystals to an operating temperature of $\sim 80\text{K}$. As the sensitivity analysis was based on the real INTEGRAL SPI background, we can assume a similar anticoincidence shield made of BGO. However, a material much more suited for use in the anticoincidence shielding is LYSO, however, and has been baselined when calculating the mass budgets. We can expect better background rejection using LYSO due to its more advantageous decay constant, higher light yield and much better energy resolution compared to BGO. It is also commercially available. Each of the anticoincidence crystals will require a photomultiplier of some kind, such as a PMT or an advanced photo diode.

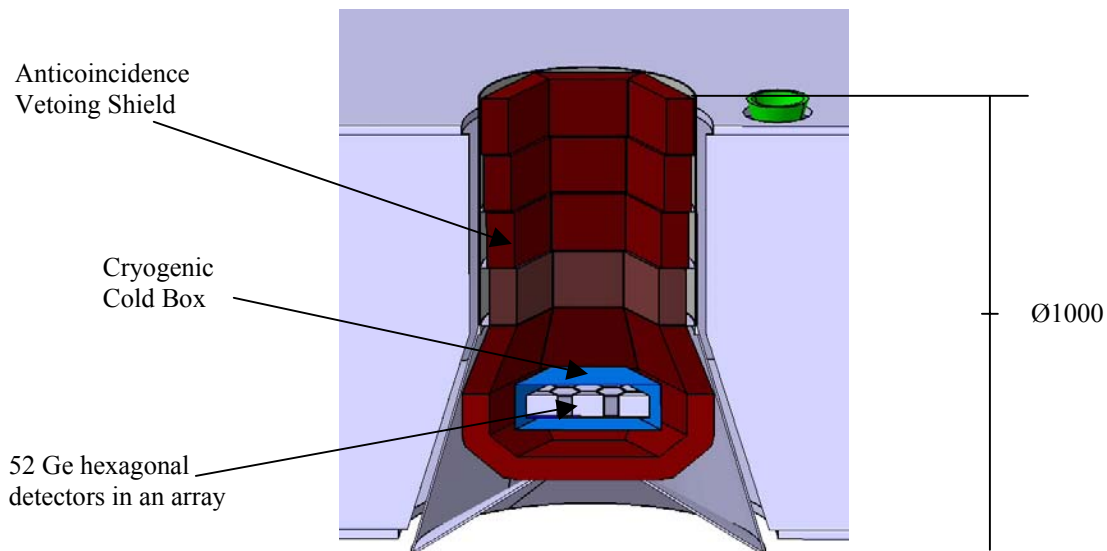


Fig. 9.12 GRL Spectrometer setup

Subsystems associated with the GRL detector payload are the amplifiers, analogue front end electronics, pulse shape discriminator, digital front end electronics, a plastic scintillator vetoing shield surrounding the detector, vetoing particle events, and the data processing electronics.

High voltage ($\sim 4000\text{ V}$) is supplied to each detector, and the output signal is sent to an amplifier, before being directed in parallel to the analogue front end electronics, and a pulse shape discriminator. The latter analyses the shape of the pulse delivered after each gamma ray interaction on a detector and the data is sent to the digital front end electronics.

The events detected through the anticoincidence shield are processed by special veto control unit electronics. Both information from detectors and from the anticoincidence veto shield are sent to the digital front end electronics that prepares and dates all information to be sent to the data processing electronics that, in turn, prepares the telemetry packet to be sent to ground.

9.3.3 Subsystems

As with the Soyuz Fregat configuration, no in-depth subsystem design was conducted at this stage. However, again, for mass budgeting purposes the key subsystems were considered and values for mass and power estimated based on other similar missions either previously flown or under study (XEUS, INTEGRAL etc.). The subsystem budgets were considered in greater detail here than in the Soyuz Fregat scenario, however. See section 8.3.2 for a brief description of the DSC key subsystems.

9.3.4 Mass Budget

Table 9.8 shows the preliminary mass budget for the large DSC - Ariane 5 configuration. The maximum dry mass of the spacecraft is 1284 kg including a system margin of 20% (equivalent to 153 kg). For a more in-depth mass budget system breakdown, see Appendix E

System	Mass (kg)	Margin (%)	Total Mass inc. Margin (kg)
Communication	19	10	21
Data Handling	14	20	17
AOCS	24	5	25
Propulsion	47	5	49
Power	32	10	36
Metrology	39	10	42
Harness	21	20	25
Spectrometer	169	10	187
Structure	195	20	234
Thermal	27	20	32
Mechanisms	5	20	6
Pyrotechnics	5	20	6
Dry mass	-	-	680
System Margin	-	20	136
Total Dry Mass + Margin	-	*	816
Adapter	-	-	98
Propellant	-	-	365
Total DSC mass	-	-	1279

Table 9.8 Preliminary mass budget for the Ariane 5-sized DSC

9.3.5 Power Budget

Table 9.9 shows the preliminary power budget for the large DSC - Ariane 5 configuration. The maximum power required by the spacecraft is 601 W. The same power budget was used for the Soyuz Fregat scenario as there is minimal difference made to the power requirements of the spacecraft from the increased payload mass.

System	Power inc. 20% Margin (W)
Communication	87
Data Handling	31
AOCS	49
Power	19
Metrology	65
Instruments	150
Structure	0
Thermal	100
Mechanisms	0
System Margin	20 %
Total Power + Margin	601 W

Table 9.9 Preliminary power budget for the DSC

9.4 GRL Mission Configuration

9.4.1 Mission Architecture

The two spacecraft will be launched in one single Ariane 5 ECA rocket from Kourou in French Guyana, utilising the short SPELTRA 5660 fairing. As can be seen in figure 9.13, the two spacecraft will be stacked in the fairing with the OSC placed on top of the DSC. The two spacecraft will be connected to each other using a standard 2624 cylindrical adapter, with an identical adapter attaching the stack to the launcher upper stage. The two spacecraft have been designed with the stacked configuration in mind, in particular the detector spacecraft's ability to withstand the load of the much larger OSC during launch. A clear load path has been assured by careful attention in the bus design of both spacecraft, minimising stresses during launch. Tables 9.10 and 9.11 summarise the mass of the GRL stack and the total Δv budget for the mission, respectively.

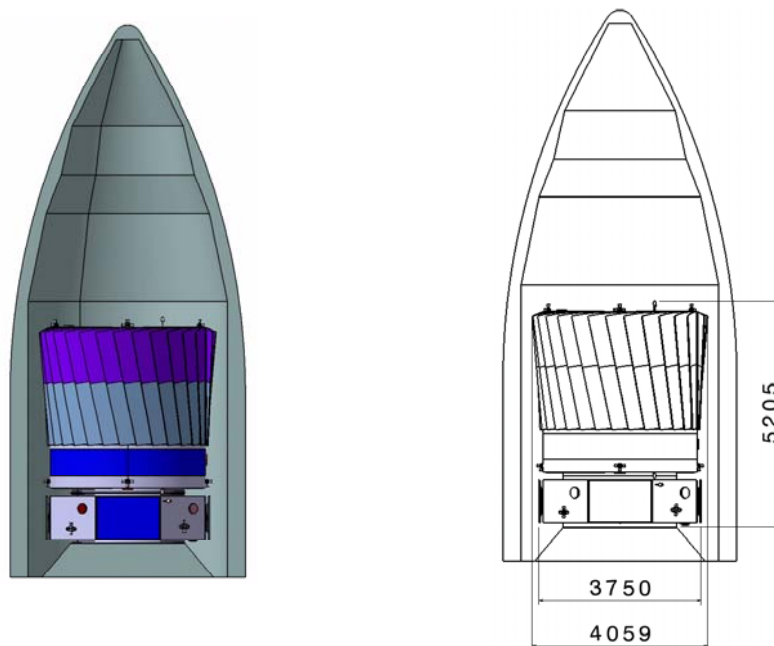


Figure 9.13 The GRL Ariane 5 configuration Stack inside the short SPELTRA 5660 fairing. The spacecraft use two 2624 cm cylindrical adapters.

Both spacecraft will be launched as a stack into an L2 direct injection trajectory as outlined in section 9.1.1. The stack will separate from the upper stage and will cruise together as a single spacecraft until the final mid-course correction manoeuvres are completed, at which point the two spacecraft separate (fig. 9.14). Before separation, the spacecraft will behave as a single craft, with the DSC performing any attitude corrections. Both spacecraft have the capability to generate enough power from the visible solar arrays during the cruise phase.

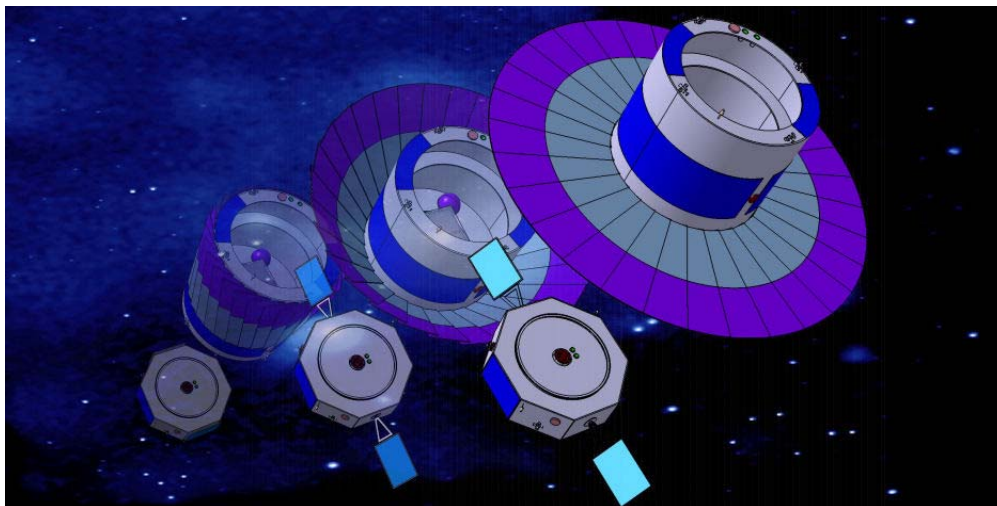


Fig. 9.14 Drawing illustrating the separation and deployment of the two spacecraft on the completion of final course corrections

The spacecraft separate to a safe distance of a few kilometres and cruise to L2 where, using the RF and optical metrology systems, a formation flying lock of 504m is established (fig. 9.15)

	Total Wet Mass + Margins
OSC	3505 kg
DSC	1279 kg
Total Mass	4784 kg
Arian 5 Performance to L2	6800 kg
Surplus Mass Available	2013 kg

Table 9.10 Summary of total spacecraft mass for the stacked configuration

Manoeuvre	Δv	Margin (%)	Δv with Margin
Injection	25	5	26.25
Halo Correction	3	5	3.15
Slewing/Re-pointing	105.5575132	100	211.1150263
	15	100	30
Station Keeping	10	100	20
Momentum Dumping	37	100	74
Total	195.5575132		364.5150263

Table 9.11 Total Δv budget for the GRL spacecraft, based on the separation scenario described above.

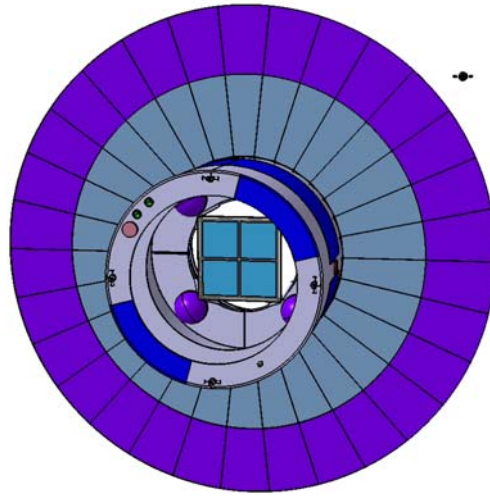


Fig. 9.15 The OSC and DSC in formation flight. The two spacecraft shown here are to scale for a focal length of 504m.

Observations will last for 14-30 days, the spacecraft re-pointing after each observation to the next target. Re-pointing is performed by the OSC turning on it's centre of mass and the DSC maintaining the formation lock by moving in a arc as well as turning on it's centre of mass. If a SNe Ia is reported during an observation, it may be necessary to pause the observation in favour of the new SNe Ia target. This is in order to follow the light curve evolution as outlined in section 2.1.1. Breaks in the observation of many source types are acceptable and can be continued at a later time. A sun avoidance angle of $\pm 30^\circ$ shall be adhered to (see fig 2.2).

Key Mission Drivers	
Formation flying and rendezvous	<ul style="list-style-type: none"> • AOCS design, constant formation control in order to maintain required accuracy
Metrology system	<ul style="list-style-type: none"> • Scaling up of current technology from XEUS and Darwin for much larger focal lengths (~500m)
Laue Crystals	<ul style="list-style-type: none"> • Crystal growth • Crystal characterisation • Mounting on the lens – optimising packing factor • Crystal alignment, metrology and calibration
PSF size	<ul style="list-style-type: none"> • Need to strictly control mosaicity • Inter-crystal alignment • Deployment mechanism alignment accuracy • Spacecraft warping
Silicon Pore Optics	<ul style="list-style-type: none"> • Silicon Pore Optics development • Multilayer coating design for efficient, broad energy coverage; 50-200 keV
Background rejection	<ul style="list-style-type: none"> • ‘Better’ ACS detectors • Designing out intrinsic background lines from the spacecraft • Novel techniques such as compton kinematic rejection
Mission lifetime	<ul style="list-style-type: none"> • Relatively long mission lifetime of 10-15. Poses potential difficulties for detector life since Ge isn’t radiation hard. • Possible development of other high-resolution, radiation hard focal plane detectors – LaI, LuI

Table 9.12 Summary of key mission drivers for the GRL mission

9.4.2 Link Budget and Ground Segment

Table 9.13 shows the preliminary X-band link budget calculated for the GRL, based on a ESA 15m ground station.

Distance [1000 Km]	1600	Downlink Freq [Hz]	8.45E+09
		Uplink Freq [Hz]	7.20E+09
Downlink Data Rate [kbps]	150		
Uplink Data Rate [kbps]	0.5		
Req. Eb/N0 (downlink)	3.00	Antenna Diameter [m]	0.067
		Antenna Efficiency	0.57
		Antenna Gain Downlink [dB]	13.02
		Antenna Gain Uplink [dB]	11.63
Downlink Margin Nom [dB]	6.02		
Uplink Margin Nom [dB]	0.00		
S/C antenna beamwidth [deg]	30.20		

Downlink		NOMINAL
Spacecraft		
Frequency	Mhz	8.45
RF Transmit Power	Watts	30.00
RF Transmit Power	dBW	14.77
Circuit Losses	dB	1.25
Antenna Gain	dB	13.02
Pointing Losses	dB	0.00
Spacecraft EIRP	dBW	26.54
Propagation		
Link Range	km	1600000.00
Free Space Losses	dB	235.06
Atmospheric Losses	dB	0.50
Polarisation Mismatch	dB	0.02
Total Propag Loss	dB	235.58

Ground Station		
Antenna Gain	dB _i	60.19
Pointing Loss	dB	0.10
Total Circuit Losses	dB	0.10
System Temp at Rx input	K	57.18
	dB-K	17.57
Receiver G/T	dB/K	42.52
<u>Receiver S/No</u>	<u>dBHz</u>	<u>61.98</u>
<u>Received power</u>	<u>dBm</u>	<u>-119.05</u>
Data Recovery		
Modulation Loss	dB	0.79
Implementation Loss	dB	0.40
Data Rate	bps	150000
Received Eb/No	dB	9.02
REQ Eb/No (BER 1e-5)		3.00
<u>Link Margin</u>	<u>dB</u>	<u>6.02</u>

Table 9.13 Preliminary X-band link budget for the GRL

At L2, as the orbital period is so long (~one orbit every 180 days) the geometry between ground station and the GRL evolves primarily due to the rotation of the Earth. As such, one ground station access per day is possible. The duration of this access is dependant on a) the declination of the 2-spacecraft formation and b) the latitude of the ground station.

Assuming a 5 degree minimum elevation angle, the daily access duration is shown on figure 9.16 for three ESA ground stations – namely Kourou (5.25°N) as solid line, Villafranca (40.46°N) as dotted line and Perth/New Norcia (31.58°S) as dashed line [5].

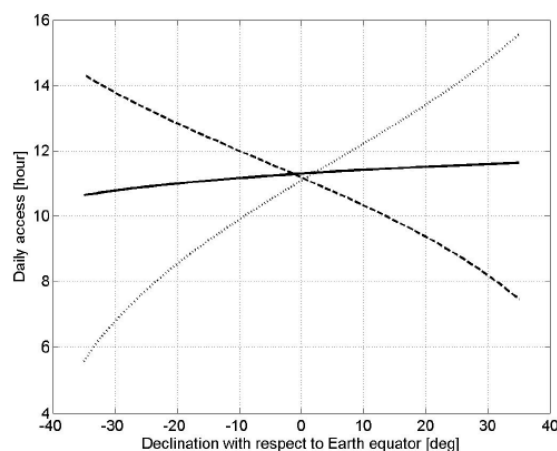


Fig. 9.16 Ground station access duration at a lagrangian point

It can be seen from figure 9.16 that an equatorial ground station guarantees at least ten hours of access per day given that the spacecraft declination with respect to the Earth is less than 35 degrees. For this reason it is recommended that the GRL utilises an equatorial ground station such as the 15 m antenna at Kourou.

The final choice of ground station will also need to take seasonal effects into account, as well as availability, as the station may be utilised for other missions. Seasonal effects and availability are both likely to reduce the access time for the GRL. We assume, therefore, an access time of ~8 hours per day. Further mission analysis is required to determine more accurate ground station access times for the GRL.

The GRL data rate is yet to be calculated. It is assumed that the data rate is similar to INTEGRAL which, like the GRL, is background limited. This assumption needs to be confirmed, although if a higher data rate is needed, increasing the power of the transmitter, implementing larger spacecraft antennae, or utilising larger ground stations are all viable options.

9.4.3 Laue Lens Effective Area

The result of the effective area analysis of the Ariane 5-size Laue lens is shown in figure 9.17. The figure also compares the effective area of the GRL to the MAX mission, as well as the previous Soyuz-Fregat configuration. Table 9.14 outlines the parameters input into the model (section 3.3.2).

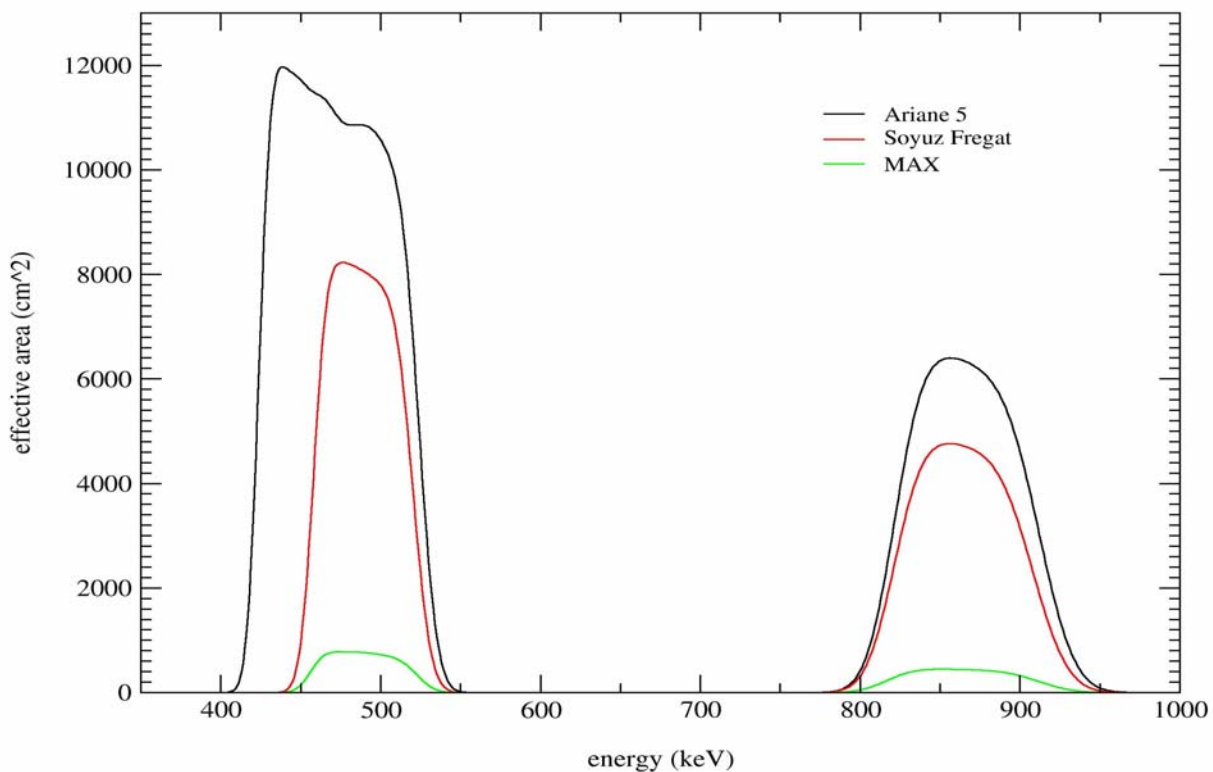


Fig. 9.17 Laue Lens effective area analysis of the Ariane 5 and Soyuz Fregat configurations. The MAX effective area is also shown here for comparison.

Configuration	f [m]	Ge_in [cm]	Ge_out [cm]	Cu_in [cm]	Cu_out [cm]
MAX	133	97	110	87	96
Soyuz Fregat	436	318	360	285	314
Ariane 5	504	365	450	328	363

Table 9.14 Input parameters for the Ariane 5 configuration effective area analysis and comparison configurations

9.4.4 Sensitivity Analysis

The sensitivity model was used to establish the sensitivity of the Ariane 5 configuration. The results of this analysis are shown in figure 9.18. Tables 5.1 and 9.14 outline the parameters used to conduct the sensitivity analysis. The curves for the MAX mission and the Soyuz Fregat configuration are included here for comparison.

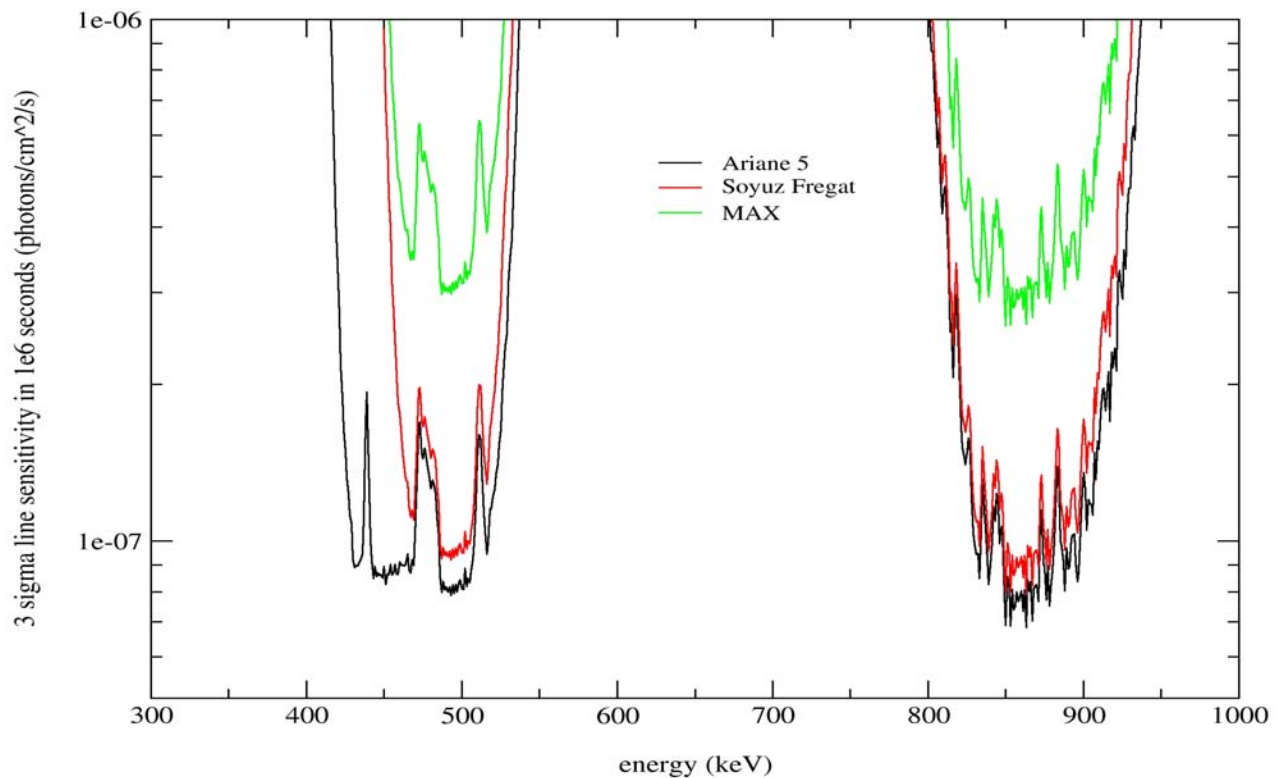


Fig. 9.18 Results of the Ariane 5 configuration sensitivity analysis for the GRL, also showing the results of the Soyuz Fregat and MAX analyses for comparison

9.5 Ariane 5 Mission Profile Discussion

The effective area figure 9.17 clearly shows a large significant increase in effective area for the Ariane 5 Laue lens compared to both Soyuz Fregat and MAX configurations. However, the increase in sensitivity for the larger configuration is significantly less impressive (fig. 9.18). Only a small (1.5 – 2 times) improvement is achieved on sensitivity, providing $8 \times 10^{-8} - 2 \times 10^{-7} \text{ ph.cm}^{-2}\text{s}^{-1}$.

The reason for this is the size of the PSF. The larger Ariane 5 mission requires a greater focal length, which results in a larger PSF. This requires a larger volume of detector causing the background contribution to increase. A large portion of the sensitivity gained from increased effective area is lost through an increase in background. Figure 9.19 a) shows how increasing the focal length of the lens counteracts the increase in effective area for the two Laue lens energies of 500 keV and 850 keV.

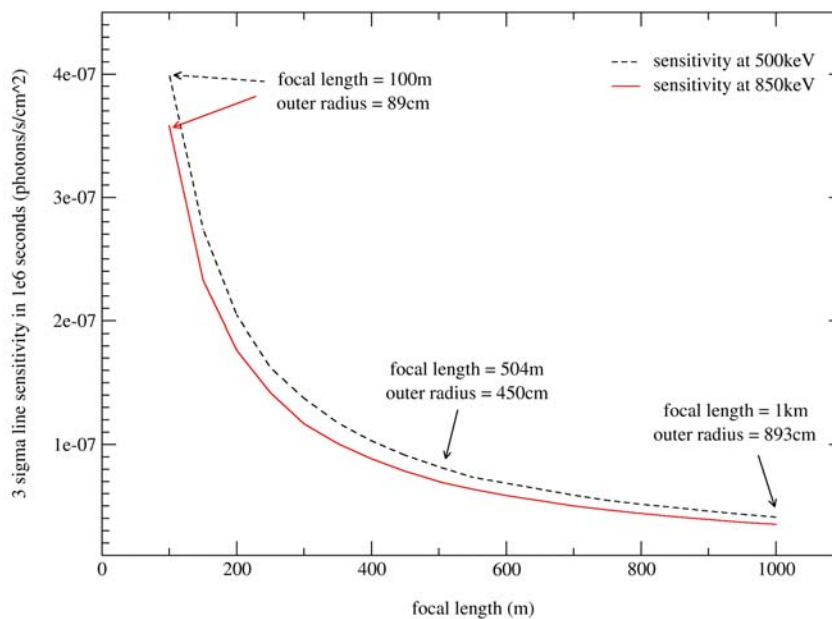


Fig. 9.19 a) 3σ line sensitivity versus focal length for 500 keV and 850 keV

The sensitivity of the Ariane 5 configuration is a great improvement on INTEGRAL, however, and achieves better than the minimum sensitivity science objective of a few times $10^{-7} \text{ ph.cm}^{-2}\text{s}^{-1}$. This configuration also meets the other stated science requirements of observing the three energy bands of significance; 50-200 keV using the silicon pore optics and 460-522 keV and 825-910 keV using the Laue lens.

If it is deemed necessary to further increase the sensitivity of the telescope, it is clear from figure 9.19 a) that increasing the area of the optic is not the most efficient means of doing so. The most effective way of achieving this goal is through background rejection. This study has assumed a

pessimistic background rejection capability identical to SPI INTEGRAL. It is likely that through better anticoincidence systems or novel background rejection techniques that the background count can be significantly reduced. The aim would be to ultimately reach a point where the sensitivity is no longer background limited, as now, but becomes photon limited. Figure 9.19 b) and c) show the 3σ line sensitivity versus focal length curve for 850 keV differs for varying fractional levels of SPI background.

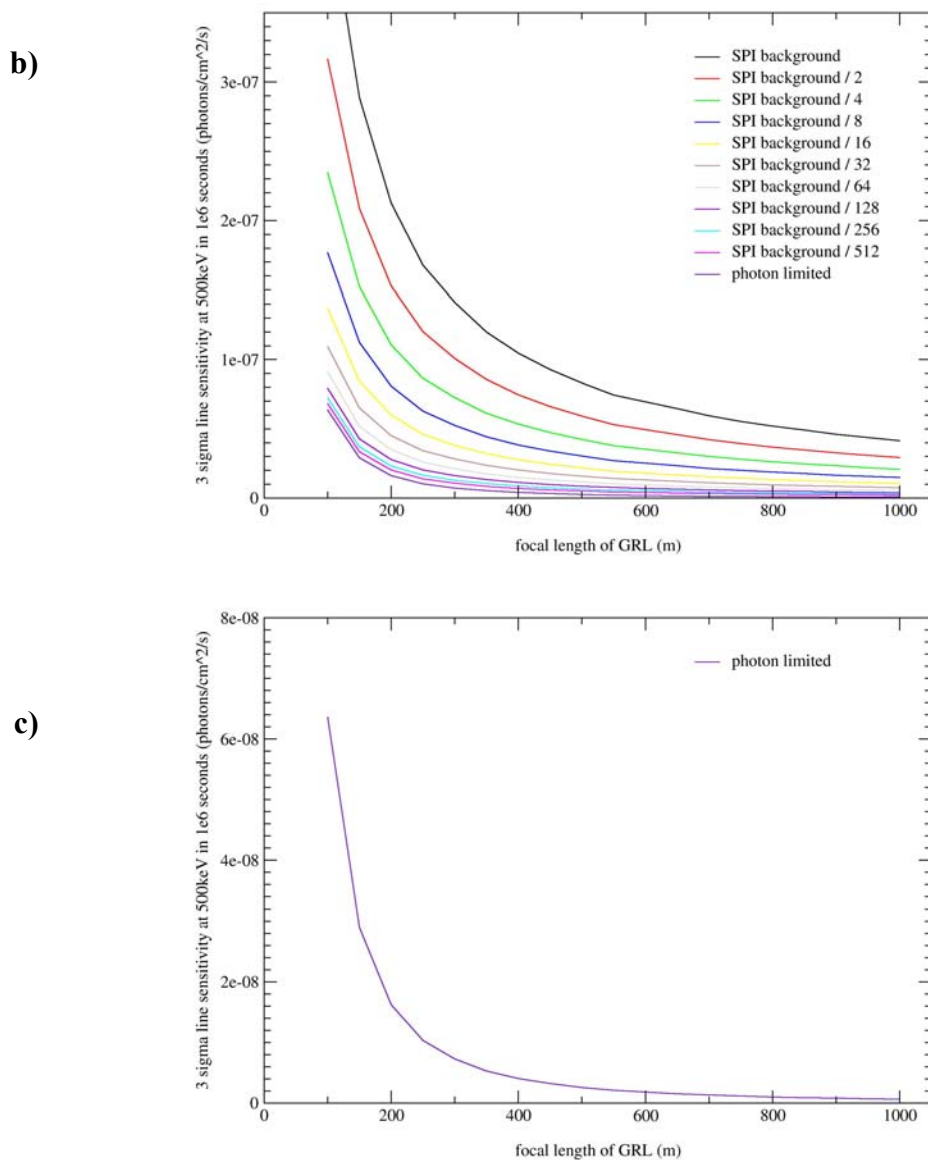


Fig. 9.19 b) 3σ line sensitivity versus focal length for 850 keV, including various increased levels of SPI INTEGRAL background rejection and c) the Photon Limited case.

It is clear from figure 9.19 c) that reaching a photon limited case is very desirable. The GRL would benefit from a massive increase in sensitivity: up to $\sim 10^{-9} \text{ ph.s}^{-1}\text{cm}^{-2}$. Increasing sensitivity requires, therefore, significant effort in developing new and improved background rejection techniques.

The primary science advantage of using the Ariane 5 configuration over the Soyuz Fregat isn't necessarily a significant increase in sensitivity, but an increase in science return from the added energy bandwidths, both from the Laue lens and the addition of the silicon pore multilayer optic.

An effective area and sensitivity analysis of the silicon pore optic is yet to be conducted, so the performance of this optic at the stated energies is unknown. However, it is known that the reflection efficiency of the optic increases with focal length due to the small angle dependence. Some long focal length multilayers have been simulated previously by Cosine [6] and have shown some promising results. Figure 9.20 shows the result of one such simulation.

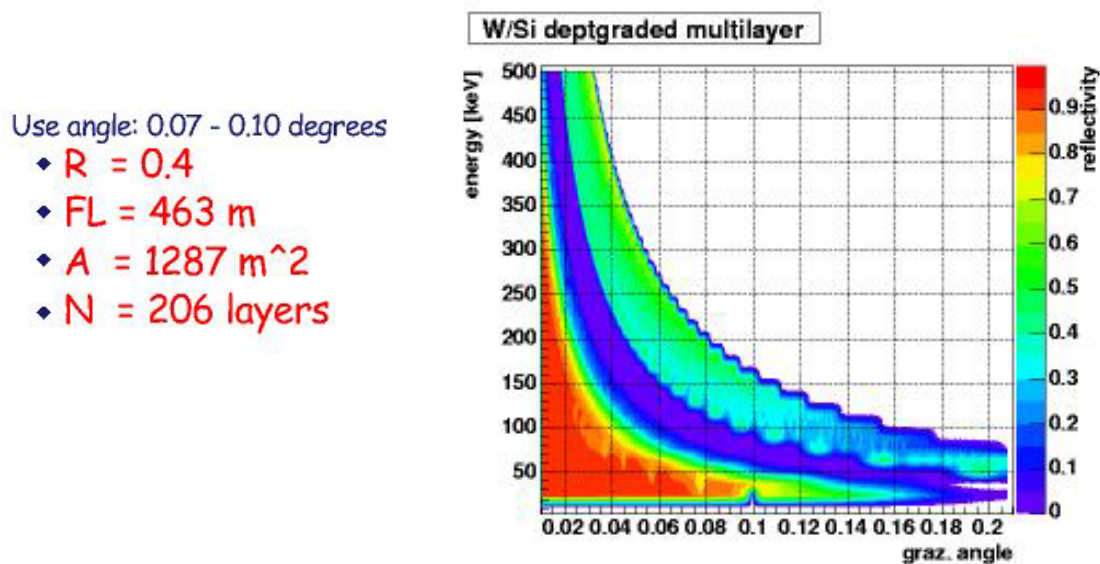


Fig. 9.20 Cosine simulation result for a multilayer mirror, focal length $\sim 463 \text{ m}$

Table 9.10 shows that the current Ariane 5 configuration has a mass of $\sim 4760 \text{ kg}$, leaving $\sim 2000 \text{ kg}$ of payload capability unused. We know that increasing the effective area of the stated energy bands results in a very small improvement of sensitivity and is, therefore, not likely worth the additional mass. However, there is the possibility of making the energy band larger, making the lens less monochromatic. Table 9.15 outlines the parameters of an example extended Ariane 5 configuration, figures 9.21 and 9.22 showing the effective area and sensitivity analysis.

Configuration	f [m]	Ge_in [cm]	Ge_out [cm]	Cu_in [cm]	Cu_out [cm]
MAX	133	97	110	87	96
Soyuz Fregat	436	318	360	285	314
Ariane 5	504	365	450	328	363
Extended Ariane 5	356	259	450	232	256

Extended Ariane 5 Lens mass	2204 kg
Extended Ariane 5 total wet payload mass	5282 kg

Table 9.15 Input parameters for the extended Ariane 5 configuration effective area analysis and comparison configurations

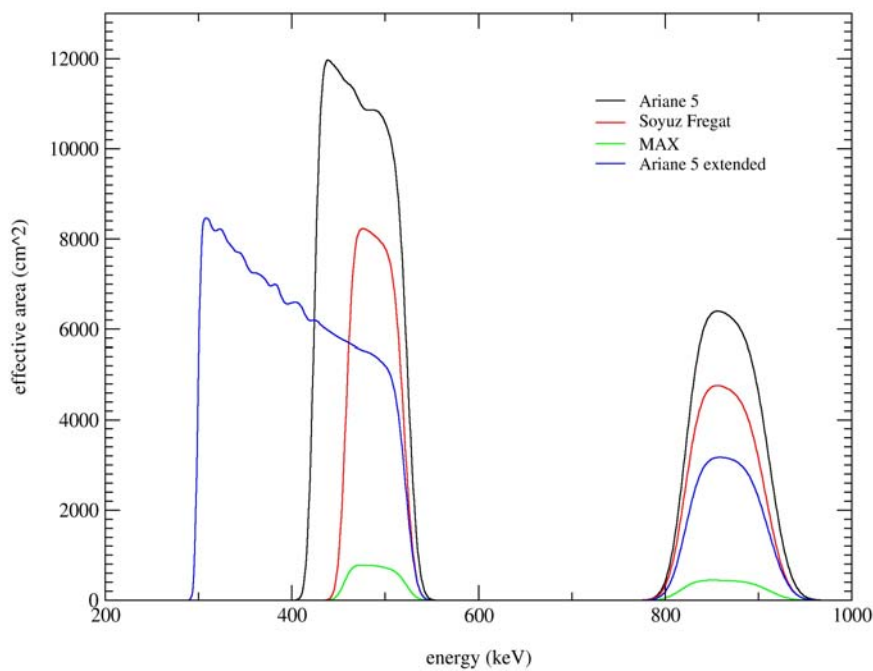


Fig 9.21 Effective area of the extended Ariane 5 configuration, with the original Ariane 5, Soyuz and MAX configurations included for comparison

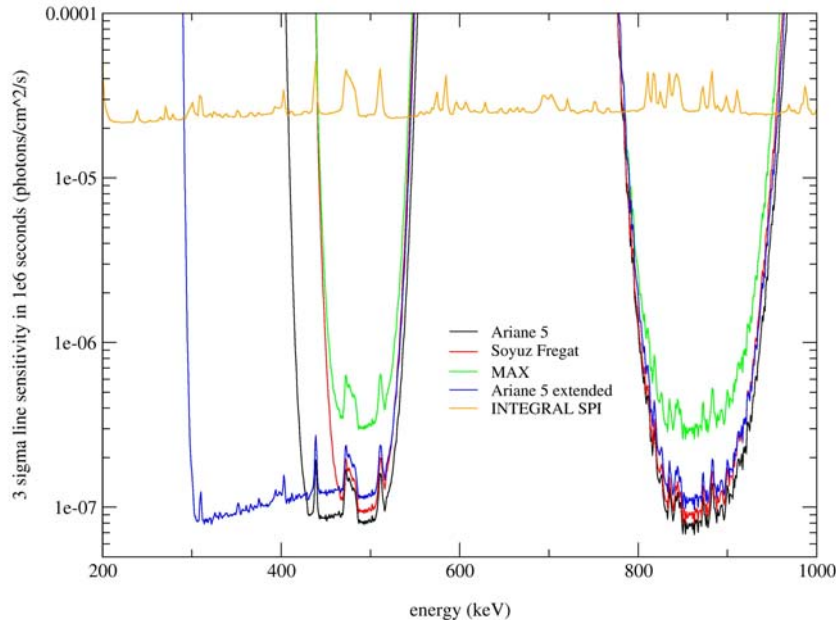


Fig. 9.22 3σ line Sensitivity analysis of the extended Ariane 5 configuration, with the original Ariane 5, Soyuz and MAX configurations included for comparison. The sensitivity of SPI INTEGRAL is also included here.

From figure 9.22 it can be seen that the lower energy band has been extended downwards to 300 keV. The configuration also benefits from a smaller focal length, also. Table 9.15 shows the extended configuration mass to be only 5282 kg, an increase of only 520 kg, with 1500 kg of unused payload capability. Different configurations of lens can be investigated using the developed effective area and sensitivity tools.

It is also important to note that the packing factor of crystals in the Laue lens will affect the effective area and hence sensitivity of the mission. Currently, a packing factor of 85% is assumed for the Laue lenses modelled here, although the MAX team [7] expect that a fill factor of 90-95% is achievable. Alternating the fill factor across the lens will also allow you to design an effective area/sensitivity profile suitable for a specific mission, as well as allowing a reduction in lens mass (see section 3.3.2).

Another important consideration is whether an additional monitor payload should be incorporated into the OSC. The Optical Monitor Camera (OMC) onboard INTEGRAL, for example, has found many uses and aids in source identification. An optical monitor could potentially be beneficial to the GRL, particularly as the optical emission from SNe Ia precedes the gamma ray emission. An optical monitor could be used to detect and locate SNe Ia. The mass available on the Ariane 5 configuration should easily accommodate an optical monitor telescope. The telescope should have a wide field of view and good angular resolution.

9.6 Ariane 5 Mission Profile Conclusions

In conclusion, both Ariane 5 configurations meet the GRL science requirements as established in section 2.2, with the extended Ariane 5 configuration also providing additional coverage of the 300-460 keV energy band. The extended Ariane 5 configuration demonstrates clearly that the Laue lens need not be considered as a monochromatic instrument, but could in fact be used to investigate areas of the continuum. Coupled with a multilayer silicon pore optic optimised for energies up to 300 keV, the continuum from 1-522 keV could be investigated. The Laue lens would give a 3σ continuum sensitivity of $\sim 3 \times 10^{-9} \text{ ph.cm}^{-2}\text{s}^{-1}\text{keV}^{-1}$.

The ultimate decision on mission configuration will result from a trade-off between cost and scientific return but, as with all science missions, the scientific return of the GRL is subjective. The trade-off required can be clearly seen in the various configurations investigated in this report, most notably in the two extreme cases of the Soyuz Fregat and the extended Ariane 5 GRL configurations. The Soyuz Fregat GRL mission is very capable of achieving results of scientific worth, although achieving all of the science requirements defined in section 2.2 requires additional investment in the larger Ariane 5 configuration.

9.7 References

- [1] CDF Study Report – XEUS, the X-ray Evolving Universe Spectroscopy mission. CDF-31(A), October 2004
- [2] Cosine Presentation, ESTEC, 2005
- [3] XEUS CDF Study Report, CDF-31(A) October 2004
- [4] Ariane 5 User Manual, Issue 3, March 2000
- [5] Current Status of MAX mission analysis, V. Martinot et al., Alcatel 2005
- [6] Cosine presentation, ESTEC, 2004.
- [7] Teleconference with Peter Von Ballmoos (MAX group), 2004.

10 Future Work & Potential Technology Development Activities

The primary goal of the Gamma Ray Lens Technology Reference Study is to establish areas for further research, work and potential technology development. Throughout the course of this study, numerous areas of required further investigation have been recognised, some GRL specific, others transferable to other space missions. This section will outline these findings.

10.1 Future Activities

- **Gradient Crystals** – Section 3.2.6 introduces the concept of gradient crystals. These are crystals whose plane distance ('d' in Bragg's equation) varies with position through the thickness of the crystal - analogous to the gradient multilayer mirrors also introduced in section 3.

It is a recommendation that a theoretical lens configuration composed of gradient crystals be investigated. New models for both sensitivity and effective area need to be established for gradient crystals. References [1] and [2] introduce the concept of gradient crystals and discuss some potential Laue lens configurations, including gamma-ray imaging techniques.

System trade-off studies also need to be conducted on whether fixed gradient crystals (crystals grown with an inherent gradient) or variable gradient crystals (gradients induced by a temperature difference) should be used. Variable gradient crystals could broaden the science case but could prove difficult to implement.

- **Crystal temperature effects** – The effect on crystals due to temperature will be important from a thermal analysis point of view. How temperature and thermal gradients across the lens affect the PSF, crystal alignment and mosaicity are important factor that requires further investigation.
- **Crystal Misalignment** – The basic concept of how crystal misalignment will affect the PSF is introduced in Appendix C. Further investigation should be carried out on the effect of crystal misalignment on the PSF through monte-carlo simulation.
- **Graded Multilayer Coatings** – The Ariane 5 configurations of the GRL use an additional payload, a silicon micropore optic coated with a graded multilayer, in order to observe energies of 50-200 keV. A graded multilayer capable of meeting the science requirements of this instrument (section 9.2.2.2) needs to be designed and simulated. Choice of material, layer thickness and depth grading profile should be investigated.
- **Silicon Pore Optics** – It is required that the silicon pore optic for the GRL be designed and developed. The effective area, angular resolution and field of view of the optics are to be modelled for various scenarios.

- **Metrology** – Missions such as Darwin, Lisa and XEUS all require very accurate levels of metrology [3]. Systems are currently being investigated and designed for these missions. However, no formation flying mission under development will fly with such a large distance between two spacecraft. It is necessary, therefore, to investigate the transferability of the current metrology systems proposed for missions in development to the Gamma Ray Lens. If it is found that current laser metrology systems are not feasible for such large-scale formation flying, other metrology systems must be developed.
- **Background Rejection Techniques** – Current background rejection techniques are primarily based on anticoincidence vetoing systems and pulse shape discrimination. Sensitivity of the GRL, as with other high-energy astrophysics missions, is greatly reduced with large background readings. The MAX mission proposes the use of a detector capable of using Compton kinematics in background rejection. This technique, and any other potential background rejection techniques, should be investigated for application to the GRL or other background limited missions.

Another key activity for background rejection is the ‘designing out’ of gamma ray lines seen in the intrinsic background as a result of activation within the spacecraft. For example, a great deal of work has been invested in identifying the sources of lines within INTEGRAL’s intrinsic background. The GRL should learn from the findings of this research, and aim to design the spacecraft to minimise the line features contributing to the background in the energy bands of interest.

- **Improved Spacecraft Definition** – Pursuing the GRL study into greater depth will result in the revision and improvement of spacecraft definition. For example, more work is required in order to improve understanding of the deployment mechanism and thermal system on the OSC. A tradeoff study is required for both propulsion system for formation flying requirements, also. There are some concerns that the XEUS metrology system is unsuitable for focal lengths as large as 500m so better definition of the GRL metrology system is also recommended.
- **Polarisation** – As mentioned in section 2, polarisation measurements are frequently mentioned in the science community as desirable in the high-energy regime. A thorough investigation should be made of potential gamma-ray polarisation techniques and, in particular, the possibility of designing a detector capable of conducting polarisation measurements while simultaneously conducting spectroscopy or imaging [4][5][6].
- **Programmatics and costing** – A thorough programmatics and cost analysis of the GRL mission should be conducted in order to truly establish the worth of the mission. Ultimately, as with all science missions, the final mission configuration will depend on the trade-off between cost and science return. It is currently expected that the GRL Ariane 5 configurations represent ESA Cornerstone class missions.

10.2 Technology Development Activities

- **Laue Crystals**
 - **Mass production of crystals** – A technique for growing and mass producing crystals is important due to the very large quantity required to make a lens. A means of mass production will also reduce the cost of producing such crystals.
 - **Crystal quality and mosaicity control** - Repeatedly growing crystals of a certain quality and with a given mosaicity will be an important step in the construction of a large-scale Laue lens. Currently, each individual crystal requires measurement and classification, many crystals from a batch being discarded due to unsuitable mosaicity. Testing each crystal could prove prohibitive if >200,000 crystals require individual classification.
- **Gradient Crystals**
 - **Mass production** - Techniques for the controlled growth and mass production of fixed gradient crystals should be developed.
 - **Temperature gradient crystals** - Techniques for creating and controlling temperature gradient crystals should be developed.
 - **Laue optic systems** - Breadboard models of Laue optic systems should be produced in order to demonstrate the gradient crystals and measure their performance at the energies of interest. Both imaging and non-imaging systems could potentially be of interest. Verification of the technology through a balloon flight would be desirable.
- **Laue Lens Construction**
 - **Close packing** - Techniques should be developed where the packing factor is optimised. A larger packing factor results in an increase of effective area and, therefore, sensitivity without increasing the focal length/background.
 - **Crystal mounting** - The extreme quantity of individual crystals suggests that an automated method of crystal mounting will be required. How the crystals are attached to the lens frame is also important when minimising thermal gradients and mass.
 - **Metrology and control of crystal alignment** – Crystal alignment is of great importance in Laue lens manufacture. A method of measuring and controlling the alignment of each individual Laue crystal is important.

- **Large, deployable mechanisms** – The Laue lens requires a large deployable circular structure. To date, no mechanism this shape and size has been flown on a spacecraft. The alignment requirements of the Laue crystals imply that an extremely position-accurate mechanism is required. Simplicity and reliability are key requirements. The design, development and demonstration of such a large-scale mechanism is necessary. Any processes developed for the GRL will be transferable to other missions requiring such large apparatus.
- **Multilayer Mirrors**
 - **Materials** – Various materials should be investigated and demonstrated for the creation of bilayers efficiently capable of reflecting energies of 50-300 keV.
 - **Multilayer Profiles** – Multilayers of optimum thickness and depth grading profile should be developed and demonstrated for the energies of 50-300 keV.
- **High-energy detectors**
 - **LYSO** - Cerium doped Lutetium Yttrium Orthosilicate (LYSO) should be developed and tested for the application of anti-coincidence shielding.
 - **LuAP** – The development of Lutetium Aluminium Perovskite (LuAP) for anti-coincidence shielding applications would be beneficial. This material's very fast decay period and high density make it a good candidate for a vetoing system, while still improving on the energy resolution of BGO.
 - **LaBr, LaI and LuI** – The Halide scintillators are extremely promising materials for use in gamma-ray detection. In particular, LaI and LuI have the potential for high-energy resolution applications, potentially replacing Ge as a focal plane detector. These materials would require no active cooling and are extremely radiation hard, ideal for astrophysics applications and missions of long duration. These materials are in an extremely early stage of development. Manufacturing processes also need to be established.

Development in the area of high energy detectors can have some serious spin-off benefits, particularly in the area of medicine. Detectors of improved spectral resolution could revolutionise the detection of diseases such as cancer. The commercial availability of such detectors is very important.
- **Polarisation measurement**
 - **Techniques** – Techniques for measuring gamma-ray polarisation should be developed and simulated. Being able to perform polarisation studies while simultaneously imaging or conducting spectroscopy is highly desirable.

- **Laboratory Demonstrations** – Demonstrations of polarisation measurements should be performed in the laboratory
- **Flight Demonstration** – A balloon flight demonstration of gamma-ray polarisation techniques is a necessary pre-cursor to a possible space-flown instrument. Such a demonstration will give a strong indication of the potential of a similar space-based polarisation detector.

10.3 References

- [1] Robert K. Smither, Crystal Diffraction Lenses for Imaging Gamma-Ray Telescope, World Scientific, 1986
- [2] G.K Skinner and P. B Fernandez, Variable-Metric diffraction crystals for X-Ray Optics, Rev. Sci. Instrum. 63 (2), February 1992
- [3] XEUS CDF Study Report, CDF-31(A) October 2004
- [4] Status and prospect for polarimetry in high energy astrophysics, M.L. McConnell, J.M. Ryan, New Astronomy Reviews 48, 215-219, 2004
- [5] A CdTe position sensitive spectrometer for hard X- and soft Gamma-ray polarimetry, E. Caroli et al, Nuclear Instruments and Methods in Physics Research A 477 567-573, 2003
- [6] CACT μ S: A small CdTe array for a prototype balloon experiment, E. Caroli et al. Nuclear Instruments and Methods in Physics Research A 513 357 – 361, 2003

11. Appendices

11.1 Appendix A - Soyuz Launchers; Current Status and Proposed Upgrades for use to L2

The aim of this section is to provide a quick reference for the Soyuz launch vehicle, introducing potential future developments, with special regard to missions involving L2. It is expected that all proposed upgrades would be ready for use by mid 2004, allowing all future Soyuz-Fregat missions to employ this advanced configuration.

11.1.1 Soyuz-Fregat performance (Soyuz user manual)

No current projections of a direct injection into L2 have been undertaken using Soyuz-Fregat parameters as stated in the Soyuz User Manual. This launcher configuration, however, is capable of launching a maximum of 1600 kg into an escape trajectory. It can be assumed that a similar mass could be achieved with the same launcher to L2, at a distance of approx. 1.5 million kilometres outwards from Earth. The launcher is currently available with two types of fairing – the S-type fairing and the ST-type fairing.

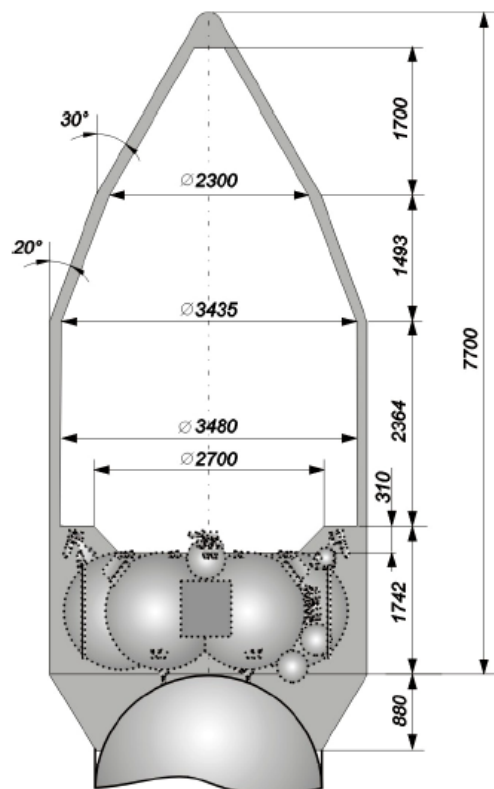


Fig A1.1a –S-Type fairing envelope

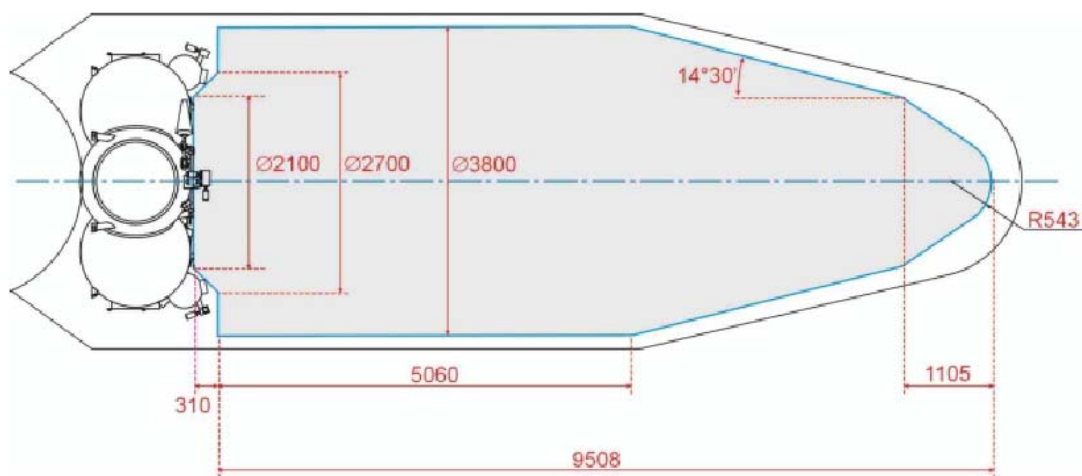


Fig A1.1b –ST-Type fairing envelope

	S-Type Fairing	ST-Type Fairing
Max. External Diameter	3.715 m	4.110 m
Max. Internal Diameter	3.480 m	3.80 m
External Length	7.700 m	11.443 m
Internal Length	5.867 m	9.818 m

Table A1.1 – Comparison between S-Type and ST-Type fairing dimensions

The data used for the current Soyuz status was obtained from the Soyuz User Manual by Starsem and is available on the internal DMS system under General Launchers.

The Soyuz-FG with Fregat upper stage successfully launched Mars Express in 2003. The parameters of this Soyuz launch vehicle are outlined below.

Lift off weight	308 tonnes
Propellant Weight	279.5 tonnes
Height	43.5 m
Thrust in Vacuum:	
First Stage	4964 kN
Second Stage	997 kN
Third Stage	294.2 kN
Fourth (Fregat) Stage	19.62 kN

Table A1.2 – Summary of Soyuz-FG parameters

11.1.2 The upgraded soyuz-st/Fregat 2-1b

STARSEM announced plans to upgrade the Soyuz launcher system in order to improve its capability in high-energy missions. Part of this plan was also to begin launching Soyuz craft from Kourou in collaboration with ESA. The upgraded systems are envisaged to be ready for use by the end of 2004 and launches from Kourou are expected to commence in 2008.

The following figure shows the main proposed upgrades.

Evolution	Main Features	Advantages	Driving Program(s)	Available
FG Engines	Improved 1st and 2nd stage engines $\Delta I_{sp} = 8 \text{ s}$ (1 st stage), 5 s (2 nd stage)	Increased Performance	ISS Mars Express	2001
Fregat Evolution	$\Delta \text{mass}_{\text{inert}} = -150 \text{ kg}$ $\Delta I_{sp} = +3 \text{ s}$	Increased Performance	Mars Express Metop Small GTO	2003-2004
3rd Stage Engine	Staged combustion engine ($\Delta I_{sp} = +32 \text{ s}$)	Increased Performance	Small GTO Galileo	2004
ST Fairing	$\phi_{\text{EXT}} = 4.11 \text{ m}$ ($\phi_{\text{INT}} = 3.80 \text{ m}$) $L = 11.4 \text{ m}$	Increased Payload Volume	Metop	2004
Digital Avionics	On Board Computer Data buses Gimbaled IMU	Mission Flexibility	Metop	2003

Table A1.3- Table showing proposed Soyuz Fregat upgrades, advantages and expected availability

These improvements will allow a significant increase in payload mass and volume. One of the most desirable aspects of the Soyuz launcher is cost. The cost of launching the Soyuz Fregat from Kourou is yet unknown, however it is expected that the use of the Soyuz Fregat from Kourou has the potential to greatly reduce mission costs.

The Soyuz Fregat 2-1b has been considered as the launcher for missions to L2 such as Gaia and XEUS. It is estimated that a Soyuz Fregat is capable of placing ~2050 kg directly into L2. There are other potential scenarios capable of increasing the payload mass such as a lunar gravity assist (LGA), as studied for the GAIA mission, or the HEO transfer orbit studied for XEUS. Initial studies suggest that HEO transfer orbit will allow a ~2300 kg payload launch, while a LGA will increase the payload mass to ~2200 kg.

Orbital analysis for the XEUS project has shown, however, that a rendezvous launch using direct insertion into L2 poses a difficulty with regard to launch window. The launcher must be initiated at an exactly determined time that occurs just twice a year. The launch cannot be delayed for any reason if a direct insertion is to take place and this, unfortunately, cannot be guaranteed. A HEO transfer orbit does not have this limitation as the launch can take place before this critical point in time, the spacecraft awaiting injection into L2 from this intermediate orbit.

Starsem has suggested that the Fregat upper stage could be upgraded further:

- Enlarged propellant tanks to allow better Δv optimisation for high energy missions.
- Detachable tank assembly (3250 kg of propellant) ejected after depletion, allowing better Δv for high energy missions.
- Upgraded control system – a reduction of current mass with upgraded electronics.

These upgrades have not been confirmed by Starsem as currently no commercial justification has been established.

11.1.3 Conclusions

As all Soyuz upgrades are expected to be in place by the end of 2004, it is useful to use the newer launcher parameters for all future missions likely to use this craft. Also, launch from Kourou should be considered for all missions planned beyond 2008. It is expected that a Kourou launch using a Soyuz Fregat will be more expensive than a launch from Baikonour. This cost is yet to be firmly established.

The Soyuz 2-1b launcher has been shown to be viable for payload insertion to L2 using the Fregat upper stage. For a cost of approximately 40 million euros, a payload mass of 2300 kg can be placed at L2 using a HEO transfer orbit. Direct insertion to L2 is a simpler orbital manoeuvre, however the launch window limitation for rendezvous missions is likely to make this scenario (for formation flying missions) an unlikely option. The below table shows the Soyuz Fregat 2-1b parameters complete with all upgrades.

Lift off weight	304 tonnes
Propellant Weight	279.5 tonnes
Height	43.5 m
ST Fairing Maximum Diameter	4.11 m
ST Fairing Length	11.4 m
Thrust in Vacuum:	
First Stage	4964 kN
Second Stage	997 kN
Third Stage	294.2 kN
Fourth (Frigate) Stage	19.62 kN
Payload capabilities to L2 :	
Direct Insertion	2050 kg
Lunar Gravity Assist	2200 kg
HEO Transfer Orbit	2300 kg

Table A14a - Soyuz Fregat 2-1b Launcher Parameters

Diameter	3.35 m
Height	1.5 m
Lift-off Mass	6300 kg
Propellant Mass	5350 kg
Burn out Mass	950 kg
Propellant:	
Fuel	(UDMH)
Oxidiser	Nitrogen Tetroxide
Main Engine Thrust	19850 N
Main Engine Isp	331 seconds
Restarts	20

Table A14b - Table showing the Fregat upper stage parameters of the Soyuz 2-1b

Starsem has also suggested that further Fregat upgrades are possible, although, to date, have not confirmed the undertaking of these developments.

11.1.4 Bibliography

- [1] Soyuz User Manual, STARSEM, April 2001 [on DMS].
- [2] Soyuz Launch for the GAIA Mission, STARSEM/Arianespace, March 2004 [on DMS]
- [3] Soyuz for Exploration Missions, STARSEM, February 2002, [on DMS]
- [4] Soyuz/Fregat 2-1b from Kourou: Estimated performances for HEO and escape missions. A.Yanez and Martin Hechler (ESOC, ESA), March 2004, [on DMS]

11.2 Appendix B - Point Spread Function Size – Derivation

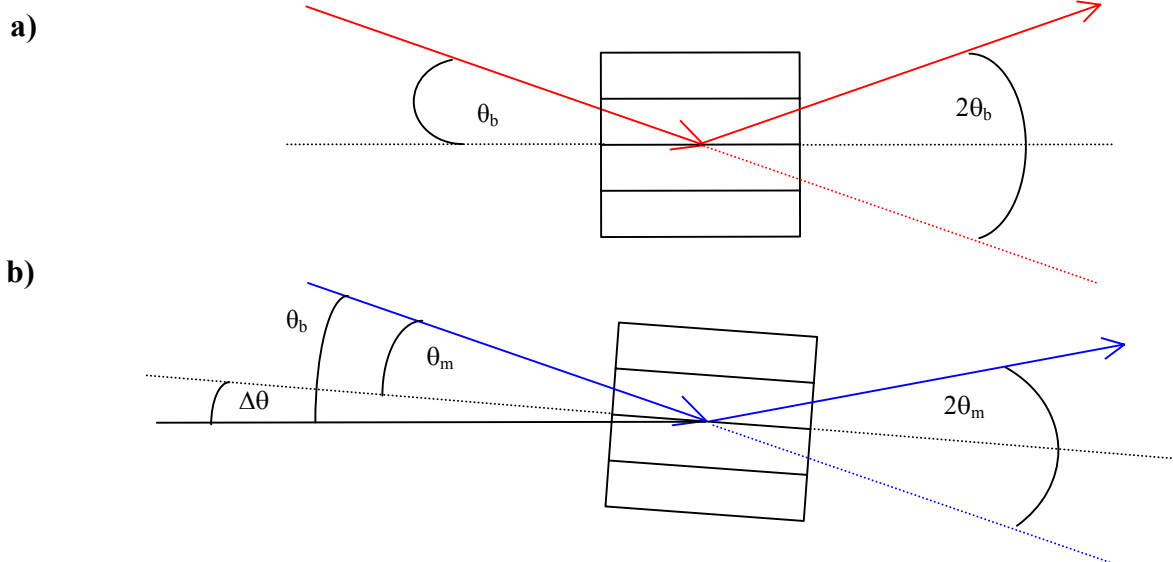


Fig. A21 a) Perfectly aligned crystal, reflection from source reflecting at the expected Bragg angle. b) Misaligned crystal, reflection from source reflecting at an unexpected Bragg angle. N.B the photons reflecting at the different Bragg angle MUST be of a different energy to that expected in order to satisfy the Bragg equation.

$\Delta\theta$ = Misalignment

θ_b = Bragg Angle due to perfectly aligned crystals

θ_m = Misalignment Bragg angle

— Perfect alignment ray path

— Misaligned ray path (higher energy)

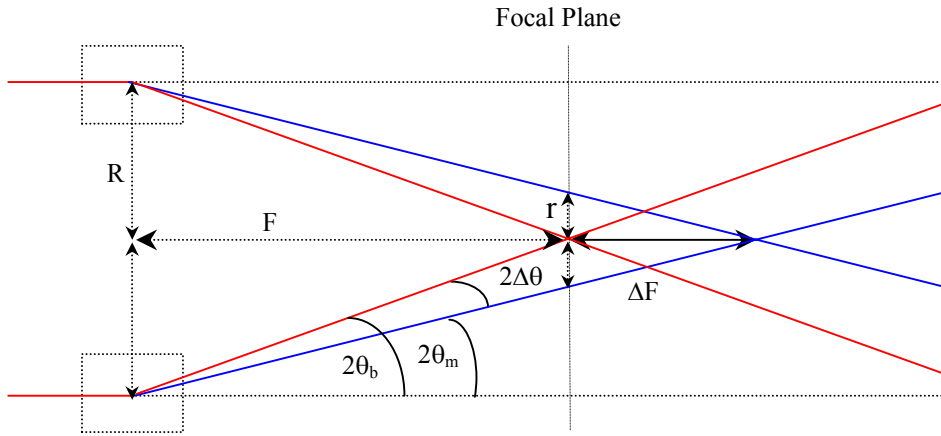


Fig. A22 - Laue Crystal lens schematic showing the ray path of both aligned and misaligned crystals.

F = Focal length due to expected Bragg angle
 ΔF = Difference in focal length due to misalignment
 R = Radius of Laue Lens
 r = Focal spot radius

— Perfect alignment ray path
 — Misaligned ray path (higher energy)

From fig A22;

$$\tan 2\theta_b = \frac{R}{F} \quad \text{For perfectly aligned crystals} \quad (\text{A2.1})$$

$$\tan 2\theta_m = \frac{R}{F + \Delta F} \quad \text{For maximum misaligned crystals} \quad (\text{A2.2})$$

From fig. A21 a) and b);

$$\bullet \quad \theta_b = \theta_m + \Delta\theta$$

$$\therefore 2\theta_m = 2\theta_b - 2\Delta\theta \quad (\text{A2.3})$$

From equations (A2.1), (A2.2) and (A2.3)

$$\therefore (F + \Delta F) \tan(2\theta_b - 2\Delta\theta) = F \tan 2\theta_b = R$$

Rearranging for ΔF ;

$$\frac{F \tan 2\theta_b}{\tan(2\theta_b - 2\Delta\theta)} - F = \Delta F$$

From fig. A22;

- $r = \Delta F \tan 2\theta_m$
 $\therefore r = \Delta F \tan(2\theta_b - 2\Delta\theta)$

Substituting for ΔF ;

$$r = \left[\frac{F \tan 2\theta_b}{\tan(2\theta_b - 2\Delta\theta)} - F \right] \tan(2\theta_b - 2\Delta\theta)$$

For the small angle approximation, $\tan \theta \rightarrow \theta$

$$r = \left[\frac{2F\theta_b}{2\theta_b - 2\Delta\theta} - F \right] [2\theta_b - 2\Delta\theta]$$

$$\Rightarrow r = 2F\Delta\theta$$

Where $\Delta\theta$ is in radians.

N.B The PSF 1σ radius can be estimated by
 $F \times (\Delta\theta/2.35)$
 where F = focal length ($\sim 500\text{m}$)
 $(\Delta\theta)$ = Effective misalignment in radians

11.3 Appendix C - Structural Requirements for the Gamma Ray Lens

The Gamma Ray Lens (GRL) is a formation flying telescope mission with stringent pointing and alignment requirements. In the context of the GRL technology reference study, we are now looking into a realistic lens structure and related deployment scheme. The aim of this note is to provide the alignment and temperature tolerance levels for the GRL in order to establish a baseline structure.

The optic spacecraft will consist of two main parts; a) the gamma ray lens itself, consisting of ~120 concentric Ge and Cu rings and b) the service module. The Gamma Ray Lens optic requires deployment and is the part of the spacecraft that requires strict alignment.

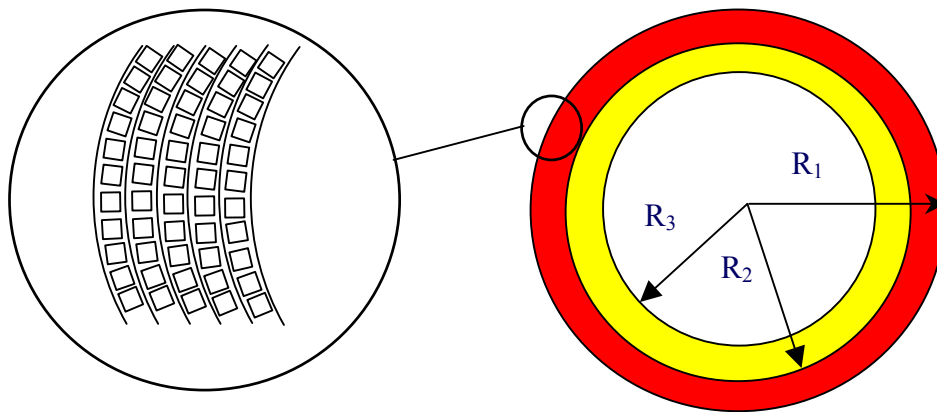


Fig A31 - The Gamma Ray Lens optic, constructed of ~85 Ge rings, ~35 Cu rings. Each crystal is 1cm^3 , packing factor of 85-90%. $R_1 = 4.50\text{m}$, $R_2 = 3.63\text{m}$ and $R_3 = 3.29\text{m}$

There are four types of ‘misalignment’ factors that affect the gamma ray lens. These are;

- a) Mosaicity, $\Delta\theta_B$
- b) Inter-crystal Misalignment, $\Delta\theta_m$
- c) Warping due to temperature effects, $\Delta\theta_w$
- d) Section tilt, θ_T

This note will consider each of these misalignments, highlighting the effects of these errors on the science of the GRL mission.

11.3.1 Mosaicity

Very few crystals display perfect behaviour. This led to the development of a model known as the Ideally Imperfect Crystal by Darwin. Such a crystal is constructed from many tiny crystal fragments arranged in a nearly but not quite parallel configuration. This is known as a mosaic

crystal. The statistical distribution of the angles is considered to be Gaussian, where the mosaicity ($\Delta\theta_B$) is defined as the FWHM of the distribution (Fig A32b). The result of such an arrangement is a broadening of $\Delta\theta$. Mosaicity is, in essence, a measure of imperfection in a crystal.

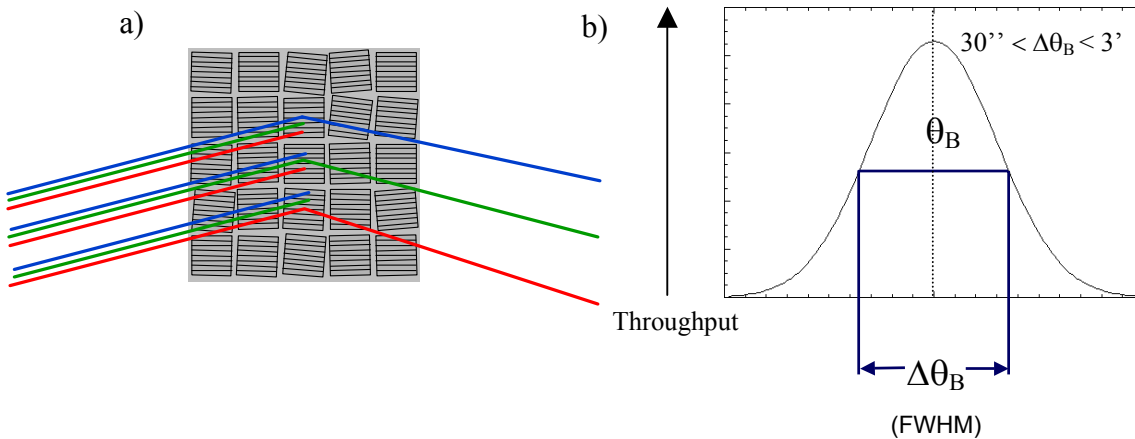


Fig A3.2 a) Schematic of a Mosaic Crystal. The three different coloured rays depict Gamma Rays of differing energy. b) The definition of mosaicity, $\Delta\theta_B$.

One important effect of increasing mosaicity is the reduction of peak efficiency. The integrated efficiency remains roughly constant. Other parameters affected by mosaicity are the size of the point-spread function (PSF), field of view (FOV), energy bandwidth and angular resolution.

It is important for the mission to use crystals with a mosaicity of $\sim 30''$ in order to receive a large, flat effective area response.

11.3.2 Inter-Crystal Misalignment

This effect could, in essence, be considered as mosaicity on a macroscopic level. The additional error in crystal alignment will result in a larger PSF. It is important, therefore, to minimise this misalignment as the PSF size directly affects the sensitivity of the mission.

Table A3.1 shows the total effective misalignment of crystals given a range of values. The values were calculated using

$$\Delta\theta_{Bm} = \sqrt{\Delta\theta_B^2 + \Delta\theta_M^2} \quad [A3.1]$$

Mosaicity ($\Delta\theta_B$)	Inter-Crystal Misalignment ($\Delta\theta_M$)	Effective Misalignment ($\Delta\theta_{BM}$)
30''	30''	42.4''
30''	15''	33.5''
30''	10''	31.6''

Table A3.1) Effective misalignment of crystals within the Gamma Ray Lens

11.3.3 Warping

A temperature gradient across the lens could induce warping. Warping will alter the orientation of the crystals from the desired direction, again resulting in an increased PSF. The warp factor can be combined with the terms in equation [A3.1] in a similar way.

$$\Delta\theta_{BMW} = \sqrt{\Delta\theta_B^2 + \Delta\theta_M^2 + \Delta\theta_W^2} \quad [A3.2]$$

11.3.4 Section Tilt

The size of the Gamma Ray Lens results in the requirement of deployment. The simplest form of deployment would be to fold the optic in two sections, allowing an optic of 9m diameter to fit inside an Ariane 5 fairing.

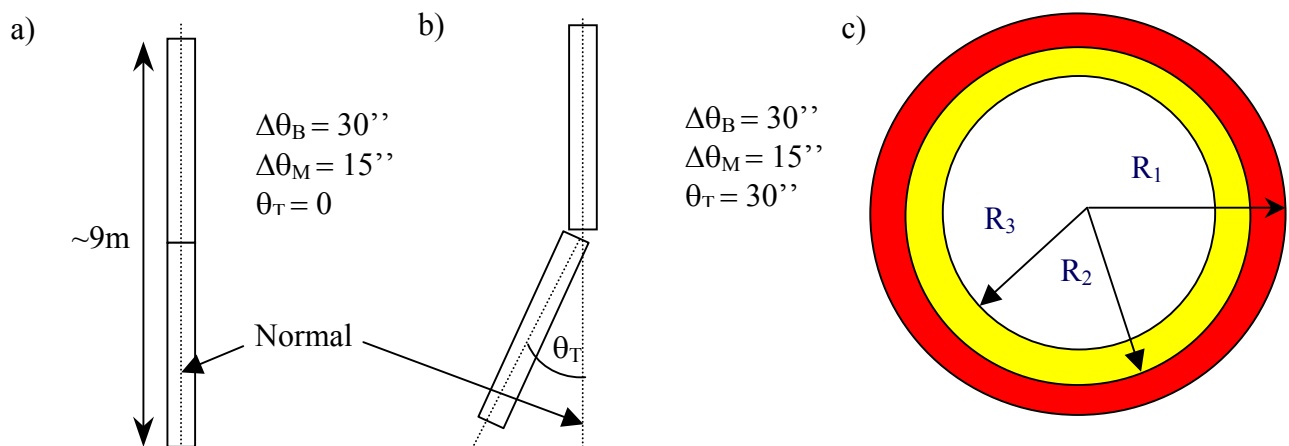


Fig. A3.3 a) A side view of the deployed GRL optic with zero tilt error ($\theta_T = 0$), b) with a tilt error of 30'' ($\theta_T = 30''$), c) front view of the GRL optic. The GRL optic consists of two rings, the outer ring of Ge crystals, and the inner ring Cu crystals

The effect on section tilt is unlike that of mosaicity and inter-crystal misalignment as it is not a random error affecting individual crystals on the lens. The effect is simply and additional angle change applied to every crystal on the portion of the lens deviating from the normal.

Fig A3.3b) shows a schematic of a lens with a tilt error of 30'' on one half of the structure. This offset would also result in an increase of the PSF. This can be quantified as follows;

$$\Delta\theta_{\text{BMWT}} = \sqrt{\Delta\theta_{\text{B}}^2 + \Delta\theta_{\text{M}}^2 + \Delta\theta_{\text{W}}^2} + \theta_{\text{T}} \quad [\text{A3.3}]$$

where θ_{T} is the section tilt angle.

Again, it can be seen that this tilt angle should be minimised and, in fact, contributes greatest to the misalignment error. Table 2 shows the effective misalignment of the lens given the added factor of a section tilt.

$(\Delta\theta_{\text{B}})$	$(\Delta\theta_{\text{M}})$	$(\Delta\theta_{\text{W}})$	(θ_{T})	$(\Delta\theta_{\text{BMWT}})$
30''	15''	30''	30''	75''

Table A3. 2 - Effective misalignment of crystals within the Gamma Ray Lens, including a section tilt factor

11.3.5 Conclusions

It is very important that we minimise the misalignment of crystals in the gamma ray lens, primarily due to the increase in PSF size. Other effects, such as an increase in angular resolution, need greater consideration although, at this time, do not appear to be limiting factors from the science point of view. Some of the effects due to increasing misalignment are outlined in the table 3.

Misalignment Increase	Effects – <i>to be verified</i>
$(\Delta\theta_B)$	Drops peak efficiency and hence effective area, Increases FOV, Decreases angular resolution, Increases PSF and hence decreases sensitivity.
$(\Delta\theta_M)$	Increases FOV, Decreases angular resolution, Increases PSF and hence decreases sensitivity.
$(\Delta\theta_W)$	Increases FOV, Decreases angular resolution, Increases PSF and hence decreases sensitivity.
(θ_T)	Increases FOV, Decreases angular resolution, Increases PSF and hence decreases sensitivity.

Even though the field of view increases due to the misalignments, the gain in FOV, although an advantage, does not compensate for the drop in sensitivity from an increased PSF.

N.B The PSF 1σ radius can be estimated by

$$F \times (\Delta\theta_{\text{BMWT}}/2.35)$$

where F = focal length ($\sim 500\text{m}$)

$(\Delta\theta_{\text{BMWT}})$ = Effective misalignment in radians

11.4 Appendix D - XEUS Mission and MSC Design

Scientific objectives	<ul style="list-style-type: none"> • Detection of massive black holes in earliest active galaxy nuclei • Study of the formation of first gravitationally bound • Study of evolution of metal synthesis • Characterisation of intergalactic medium
Payload	<ul style="list-style-type: none"> • MSC: <ul style="list-style-type: none"> ◦ Two deployable mirror leaves with in total 8 x 8 segments of which 48 are populated with mirror petals. The 16 centre segments are equipped with light tight covers due to mass constraints ◦ Petal dimension: length 70 cm, width 70 cm, height 80 cm ◦ Average petal mass: 61 kg/m²
	<ul style="list-style-type: none"> • DSC: <ul style="list-style-type: none"> ◦ WFI (Wide Field Imager) ◦ NFI2 (Narrow Field Imager 2) ◦ NFI1 (Narrow Field Imager 1) for low energy range (0.1 – 2 keV) with an energy resolution of E/dE of ~ 500 ◦ Payload options are a dispersive spectrometer (grating) allowing for higher resolutions E/dE of 1000 - 5000 range with two configurations identified
Launcher	Ariane-5 launch from Kourou carrying both MSC and DSC (launcher performance for direct injection into L2 is 6800 kg).
Spacecraft	<ul style="list-style-type: none"> • MSC nominal mission = 15 yrs, extended mission up to 20 yrs (Note: DSC is expected to be designed for 5 years and planned to be replaced when required) • Dry mass = 4586 kg. Propellant mass 294 kg. • Main S/C bus: octagonal cylinder 4100 mm x 6910 mm (stowed configuration). • Three-axis stabilised (cold gas system to prevent mirror contamination) • Reaction wheels for re-pointing to acquire new target • No formation keeping (only orbit correction & maintenance) • Payload: matrix of petals that constitute the mirror (» 1434 kg for Ariane-5, » 2610 kg for Delta IV) • Absolute point error 60 arcsec (X & Y-axes), 3600 arcsec on Z-axis • Absolute measurement error 1 arcsec (X & Y-axes), 300 arcsec on Z-axis • Two body-mounted solar arrays of 9.5 m² using triple junction cells with 28% BOL efficiency • Two switchable X-band LGAs, omni coverage • S-band inter S/C RF link • 17 different types of mechanism • Greater than 72 hrs full autonomy

Cruise Phase and XEUS deployment	<ul style="list-style-type: none"> Duration: 90 to 160 days Direct injection: <ul style="list-style-type: none"> Launcher's dispersion correction required, $\Delta V < 25$ m/s, to be performed with AOCS not later than 2 days after injection Trimming manoeuvre: < 2 m/s at day 10 Mid-course manoeuvre: < 1 m/s at day 50 MSC - DSC separation after day 50 No ΔV required for L2 halo orbit insertion The proposed XEUS deployment scenario is as follows: <ul style="list-style-type: none"> During the initial part of the cruise phase MSC and DSC remain in launch configuration and are spin stabilised (hydrazine thrusters) During the attached mode the stack is controlled by the MSC (i.e trajectory corrections and AOCS) and DSC is passenger MSC and DSC commissioning commences after stack separation and could be completed prior to target orbit (L2) being reached
Nominal	<ul style="list-style-type: none"> Duration: 15 + 5 years
Mission Phase	<ul style="list-style-type: none"> Final orbit: L2 halo orbit: <ul style="list-style-type: none"> Quasi-periodic: Every 20 days, small orbit maintenance manoeuvres needed (~ 5 cm/s) Orbit maintenance budget: 1-2 m/s per year No eclipses Amplitude: $> 670\,000$ km Orbit period: 6 months No insertion ΔV when using optimal transfer trajectory Typical observation time: 3×10^5 s (about 3.5 days)
Formation Flying Package	<ul style="list-style-type: none"> Formation set-up and precision formation flying control performed by the DSC (MSC is free-flyer, DSC is follower). The same applies when slewing to a new target: <ul style="list-style-type: none"> Both S/C move in purely inertial space Both S/C perform absolute pointing control Only the DSC performs relative distance control DSC - MSC distance during science operations shall be 50 m: <ul style="list-style-type: none"> Allowed formation flying error along optical axis: ± 5 mm Allowed formation flying error sideways to optical axis: ± 1 mm Metrology approach: <ul style="list-style-type: none"> Inter S/C distance $< 30\,000$ km: RF metrology (S-band) <ul style="list-style-type: none"> Precision at 120 m: elevation: ± 12 cm, azimuth: ± 6 cm, Range: ± 0.52 cm Six LGA antennas on MSC, six on DSC Inter S/C distance < 120 m: Optical metrology: <ul style="list-style-type: none"> Four corner cube reflectors on MSC mirror Laser rangefinder with absolute distance meter (submillimetric accuracy) on DSC Dual λ interferometer (± 3.5 μm range resolution) 12 optical heads, max. ~ 2.5 m baseline: <ul style="list-style-type: none"> Pulses sequenced to each head Multilateration During cruise after S/C separation loose formation (RF metrology) Inter S/C link (S-band) allows data transfer (housekeeping) in case one of the two spacecraft has lost communication with ground segment

Operations	<ul style="list-style-type: none"> • Only MSC housekeeping (per day: 0.3 hrs at 95 kbps) • LEOP performed by ESA LEOP network stations Kourou, Vilspa & Perth/New Norcia • Routine operations using the Perth 35-m ground station linked to XEUS mission control centre
Program-matics	<ul style="list-style-type: none"> • Model philosophy: STM, ATB & PFM • System Simulation Facility • Formation flying test bed

Appendix D Table showing a summary of the XEUS mission and MSC design

11.5 Appendix E – Ariane 5 GRL System Mass Budgets

	#	mass	nom mass	margin	mass
OSC					
Communciation			19	12.14	21
LGA (low gain antenna)	9	0.10	0.90	5	0.95
X-band transponder	2	3.45	6.90	10	7.59
X-band SSPA (Solid state power amplifier)	2	1.30	2.60	5	2.73
X-band RFDU (Radio-Frequency Distribution unit)	1	1.20	1.20	10	1.32
S-band transponder-metrology	2	3.00	6.00	20	7.20
S-band omni antenna	6	0.10	0.60	5	0.63
S-band RFDU	1	0.30	0.30	10	0.33
Data Handling			9	20	11
CDMU/MM (Central Data Management Unit/ Mass memory)	1	6	5.50	20	6.60
bus i/f	1	2	1.80	20	2.16
command matrix box	1	2	2.00	20	2.40
AOCS			31	5.00	32
CSS (Coarse Sun sensor)	4	0.10	0.40	5	0.42
FSS (Fine Sun Sensor)	2	0.62	1.24	5	1.30
Gyro	1	7.50	7.50	5	7.88
STR (star tracker)	2	1.10	2.20	5	2.31
RW (Reaction wheel)	4	4.90	19.60	5	20.58
Propulsion			17	5.00	18
THR (thruster)	8	0.30	2.40	5	2.52
Tank + valves and filters	1	15.00	15.00	5	15.75
Power			66	10.00	73
Si Solar Arrays	1	35.43	35.43	10	38.97
GaAs Solar Arrays	2	3.00	6.00	10	6.60
Battery	1	10.81	10.81	10	11.89
PCDU (Power conditioning and distribton unit)	1	13.95	13.95	10	15.35
Metrology			1	10.00	2
corner cubes	4	0.35	1.40	10	1.54
Harness			36	20	44
Instruments			1684	5	1774
Laue Lens - Ge	1	985	985	5	1034
Laue Lens - Cu	1	576	576	5	605
Silicon pore optic	1	122.5	123	10	135
Structure			485	20.00	582
Lens Petal Support	1	60.00	60.00	20	72.00
Lens Arms	1	60.00	60.00	20	72.00
Lens Suppor Ring	1	31.44	31.44	20	37.73
Main Bus	1	269.80	269.80	20	323.76

	Multilayer Support Pyramid	1	16.00	16.00	20	19.20
	Multilayer Frame	1	33.80	33.80	20	40.56
	Multilayer Case	1	14.25	14.25	20	17.10
Thermal				83	20	99
	MLI	146.3	1	73	20	88
	Radiators	1	1	1	20	1
	Paint	42.3	0	8	20	10
Mechanisms				25	20	30
Adapter (Inter S/C)		1	98	98	0	98
Pyrotechnics				5	20	6
Dry Mass						2790
System margin					20	558
Total Dry mass with margin						3348
Propellant						180
Total OSC mass						3528



DSC

Communciation				19	12.02	21
	MGA Medium gain antenna)	3	0.40	1.20	5	1.26
	X-band transponder	2	3.45	6.90	10	7.59
	X-band SSPA	2	1.30	2.60	5	2.73
	X-band RFDU	1	1.20	1.20	10	1.32
	S-band transponder-metrology	2	3.00	6.00	20	7.20
	S-band omni antenna	6	0.10	0.60	5	0.63
	S-band RFDU	1	0.30	0.30	10	0.33
Data Handling				14	20	17
	CDMU/MM (HICDS)	1	14	14.40	20	17.28
AOCS				24	5.00	25
	CSS	4	0.10	0.40	5	0.42
	FSS	2	0.62	1.24	5	1.30
	Gyro	1	7.50	7.50	5	7.88
	STR	2	1.10	2.20	5	2.31
	RW	4	3.20	12.80	5	13.44
Propulsion				47	5.00	50
	THR	8	0.30	2.40	5	2.52
	Tank + valves and filters	3	15.00	45.00	5	47.25
Power				32	10.00	36
	Solar Arrays	1	7.60	7.60	10	8.36
	Battery	1	10.81	10.81	10	11.89
	PCDU	1	13.95	13.95	10	15.35
Metrology				39	9.23	42
	laser TOF (time-of-flight)	2	3.00	6.00	10	6.60

	optical heads	12	0.50	6.00	5	6.30
	dual interferometer	1	26.90	26.90	10	29.59
Harness				20	20	23
Instruments				169	10.66	187
	Detector (Ge)	1	8.62	8.62	5	9
	ACS Side Panel (LaBr3)	6	19.05	114.30	10	126
	ACS Base Plate (LaBr3)	1	14.28	14.28	10	16
	ACS Base-Side Panle (LaBr3)	6	2.67	16.02	10	18
	Cryo-Cooler	2	3.50	7.00	20	8
	Si PM Tubes	1366	0.001	1.37	20	1.64
	Front End Electronics	1	1.00	1.00	20	1.20
	Back end Electronics	1	2.00	2.00	20	2.40
	Main Tube Case	1	2.35	2.35	20	2.82
	Detector Skirt	1	1.69	1.69	20	2.03
	Internal Structure	1				
Structure				195	20	234
	Cuboid Outer Structure	1	150	150	20	180
	Inner Cylinder	1	41	41	20	49
	Inner Walls	4	1	4	20	5
Thermal				27	20	32
		30.10				
	MLI	445	1	15	20	18
	Radiators	1	1	1	20	2
	Paint	31.54	0	6	20	8
	Heat Pipes	10	0	4	20	5
Mechanisms				5	20	6
Pyrotechnics				5	20	6
Dry Mass						680
<i>System margin</i>					20	136
Total Dry mass with margin						815
Propellant						365
Total DSC mass						1118

MSC mass						3528
DSC mass						1118
adapter mass						98
Total launch mass						4741

11.6 Appendix F – Margin Philosophy for Assessment Studies

  DOCUMENT	
document title/ titre du document	
MARGIN PHILOSOPHY FOR ASSESSMENT STUDIES	
<hr/>	
prepared by/préparé par	AA
reference/référence	SCI-A/2003.302/AA
issue/édition	1
revision/révision	4
date of issue/date d'édition	16/2/05
status/état	Draft
Document type/type de document	Technical Note
Distribution/distribution	SCI-A
<p>European Space Agency Agence spatiale européenne</p> <p>ESTEC Keplerlaan 1 - 2201 AZ Noordwijk - The Netherlands Tel. (31) 71 5656565 - Fax (31) 71 5656040</p> <p style="text-align: right;">Margin Philosophy 1_4.doc</p>	

APPROVAL

Title titre	Margin Philosophy	issue issue	1 1	revision revision	1 1
----------------	-------------------	----------------	--------	----------------------	--------

author auteur	Alessandro Atzei	date date	16/2/05
------------------	------------------	--------------	---------

approved by approuvé by		date date	
----------------------------	--	--------------	--

CHANGE LOG

reason for change /raison du changement	issue/issue	revision/revision	date/date
Update of section 2.2	1	1	23/10/03
Review by NR	1	2	26/11/03
Correction	1	3	11/2/03
Update of Delta V, communications and Temperature margin sections	1	4	16/2/05

CHANGE RECORD

Issue: 1 Revision: 3

reason for change/raison du changement	page(s)/page(s)	paragraph(s)/paragraph(s)
Reference number for comms margin corrected	7	2.5
General updates of DV section (updated as well as new margins). NB: numbering has changed!	5	2.2
New ECSS references for 2.5 and 2.6	7	2.5, 2.6

TABLE OF CONTENTS

1	INTRODUCTION	4
2	MARGINS REQUIREMENTS AND MANAGEMENT	4
2.1	Mass margins	4
2.2	Delta-V margins	5
2.3	Power margins	6
2.4	Data processing margins	7
2.5	Communications margins	7
2.6	Temperatures margins	7

1 INTRODUCTION

This document is intended to establish a common margin philosophy for SCI-A studies. The following margin philosophy is based on the Margin Requirements TN prepared for other science missions, such as Bepi Colombo and Solar Orbiter.

2 MARGINS REQUIREMENTS AND MANAGEMENT

2.1 Mass margins

- | | |
|--------|---|
| R-M-1 | At the end of the Assessment Study phase, the total mass at launch of the spacecraft shall include an ESA system level mass margin of at least 20 % of the nominal mass at launch. |
| R-M-2 | The nominal mass at launch does not include the ESA system level mass margin, but shall include the design maturity mass margins to be applied at equipment level. |
| R-M-3 | <p>This ESA system level mass margin shall:</p> <ul style="list-style-type: none"> ■ Be visible and traceable in the overall mass budget of the spacecraft composite, ■ Be uniformly distributed to the wet mass (Dry and Propellant) of all modules or elements of the spacecraft composite, ■ Not include any propellant residuals or unused propellant. |
| R-M-4 | At equipment level, the following design maturity mass margins shall be applied: |
| R-M-41 | ■ > 5 % for “Off-The-Shelf” items (ECSS Category: A / B) |
| R-M-42 | ■ > 10 % for “Off-The-Shelf” items requiring minor modifications (ECSS Category: C) |
| R-M-43 | ■ > 20 % for new designed / developed items, or items requiring major modifications or re-design (ECSS Category: D). |

2.2 *Delta-V margins*

- R-DV-1 The following Delta-V margins (covering uncertainties in mission design and system performance) shall be applied to the Effective Delta-V manoeuvres:
- R-DV-11 ■ 5 % for trajectory manoeuvres
 - R-DV-12 ■ 100 % for the orbits maintenance manoeuvres, over the specified lifetime
 - R-DV-13 ■ 100 % for the attitude control and angular momentum management manoeuvres
- R-DV-2 When manoeuvres budgets concern theoretical values, and do not take into account gravity losses (for instance: impulsive manoeuvres performed by chemical propulsion engines), such gravity losses shall be quantified and added to the specified Effective Delta-V.
- R-DV-3 Launcher dispersion for each launch vehicle shall be assessed and included (e.g. 30 m/s for the Soyuz-Fregat).
- R-DV-4 The Launcher performance penalty shall be assessed over the entire launch window, to avoid using ideal performance only.
- R-DV-5 In case of Gravity Assist Manoeuvres (GAM), an allocation of 15 m/s (TBC) shall be added to the Delta V budget for each GAM, to account for preparation and correction of these manoeuvres.
- R-DV-6 In case of electric propulsion, a 4% increase of the Delta V budget shall be foreseen for navigation during the cruise phase, to compensate for trajectory inaccuracies.
- R-DV-7 At destination, the spacecraft shall be able to perform orbit and attitude control manoeuvres, necessary for orbit maintenance during the specified lifetime.
- R-DV-8 The propulsion modules of the spacecraft shall be designed and sized for the Maximum Separated Mass.
- R-DV-9 In case of staging (multi-stages spacecraft composite), requirement R-DV-4 applies to all propulsion modules according to the Delta-V partitioning among stages.
- R-DV-10 The volume of the tanks of the propulsion modules shall be sized for the Maximum Separated Mass plus at least 10 %.

2.3 Power margins

- R-P-1 At equipment level and for conventional electronic units, the following design maturity power margins shall be applied:
- R-P-11 ■ > 5 % for “Off-The-Shelf” items (ECSS Category: A / B)
- R-P-12 ■ > 10 % for “Off-The-Shelf” items requiring minor modifications (ECSS Category: C)
- R-P-13 ■ > 20 % for new designed / developed items, or items requiring major modifications or re-design (ECSS Category: D).
- R-P-2 The following shall apply, should electric propulsion be considered: For the electronic equipment of the electric propulsion system (e.g. power conditioners; ion thruster drivers; ...) the design maturity power margins specified in R-P-1 shall only be applied to the dissipated power.
- R-P-3 At the end of the Assessment Study phase, the total power budget of the spacecraft shall include an ESA system level power margin of at least 20 % of the nominal power requirements of the spacecraft.
- R-P-4 The ESA system level power margin shall be visible and traceable in the overall power budget of the spacecraft composite.
- R-P-5 The nominal power requirements include the power requirements of all spacecraft elements (payload and platform, including their respective design maturity power margins to be applied at equipment level), and does not include the ESA system level power margin.
- R-P-6 Solar arrays and batteries shall be sized to provide the spacecraft required power, including all specified margins, at end of life.

2.4 Data processing margins

- R-SW-1 At the end of the Assessment Study phase, any on-board memory (RAM used for code and / or data) shall include a memory margin of at least 50 %.
- R-SW-2 At the end of the Assessment Study phase, any on-board processor peak usage shall not exceed 50 % of its maximum processing capability.

2.5 Communications margins

- R-C-1 Links (up-and down-link) budgets and associated margins, for all phases of the mission, shall be computed as defined in ECSS 50-05-1A including: nominal, adverse, favourable, mean – 3 sigma and worst RSS (Root Sum Square) cases.
- R-C-2 Telecommand and telemetry data rates shall be satisfied with minimum margins as defined in ECSS 50-05-1A, for all mission phases, under all cases specified in R-C-1.

2.6 Temperatures margins

- R-T-1 The different temperature ranges (calculated, predicted, design, acceptance, qualification) shall be in accordance to ECSS-E-30-1A.